CELL-MATRIX TENSIONAL FORCES WITHIN CELL-DENSE, TYPE I COLLAGEN OLIGOMER TISSUE CONSTRUCTS FACILITATE RAPID *IN VITRO* VASCULARIZATION OF DENSE TISSUE CONSTRUCTS FOR SKIN ENGINEERING

by

Kevin Buno

A Dissertation

Submitted to the Faculty of Purdue University

In Partial Fulfillment of the Requirements for the degree of

Doctor of Philosophy

Weldon School of Biomedical Engineering

West Lafayette, Indiana

December 2018

THE PURDUE UNIVERSITY GRADUATE SCHOOL
STATEMENT OF COMMITTEE APPROVAL

Dr. Sherry Voytik-Harbin, Chair

Weldon School of Biomedical Engineering

School of Basic Medical Sciences

Dr. Jenna Rickus

Associate Vice Provost for Teaching and Learning

School of Agricultural and Biological Engineering

Weldon School of Biomedical Engineering

Dr. Pavlos Vlachos

School of Mechanical Engineering

Weldon School of Biomedical Engineering

Dr. Mervin Yoder

Distinguished Professor Emeritus, Indiana University School of Medicine

Associate Dean for Entrepreneurial Research, Indiana University School of Medicine

Approved by:

Dr. George R. Wodicka

Head of the Graduate Program

To my loving parents, Peter and Lottie, for their unconditional support throughout my life.

To my grandma, Adoracion T. Mendoza, for the countless math flashcards we did in elementary school.

ACKNOWLEDGMENTS

First and foremost, I would like to express my utmost gratitude to my advisor, Dr. Sherry Voytik-Harbin, for giving me the opportunity to study under her throughout my time here at Purdue. Thank you for believing in me and for being the coolest advisor, ever. I could tell from the day I met you that we both shared a mutual excitement for collagen and tissue engineering; I knew I had to work in her lab. Her enthusiasm with everything she does provides excitement and passion that is contagious. Here is a little side story showing how awesome Sherry is. One day, our whole lab went to a presentation over at the Loeb Playhouse. On the way back, I dared her to run through the fountain. Without hesitation, she put down her phone and walked straight into the fountain. The whole lab followed suit and it was amazing. In addition to her fun-loving nature, she has provided me with unending support in terms of my professional and personal development. To satiate my desire to teach, she allowed me to mentor multiple undergraduate students. Furthermore, she offered me the unique experience of helping develop a course. This opened my eyes to the world of teaching. As for my development as a scientist, Sherry has been phenomenal. She gave me space to allow for creative freedom in research, but knew when to tighten things up if I was moving astray. Her approach to science helped me accomplish my research goals: she does not care if you break anything or spend money, as long as you are in the lab trying to make something work. She has also been there during hard times, and I valued her advice and support during those times. Overall, I am forever grateful for your mentorship, Sherry.

I would like to thank the rest of my committee, Dr. Jenna Rickus, Dr. Pavlos Vlachos, and Dr. Mervin Yoder. Dr. Rickus, I appreciate your feedback not only on the content of my research, but also on how I should effectively communicate my research. Dr. Vlachos, thank you for your valuable insight on flow-related works as well as your feedback on my research. Dr. Yoder, thank you for providing us with the endothelial colony forming cells as well as providing your clinical perspective when examining my research.

Teamwork makes the dream work! I would like to thank members of the Harbin laboratory, for their support and guidance from the beginning: Dr. Catherine Whittington, Dr. Rucha Joshi, Dr. Nimisha Bajaj, Dr. TJ Puls, Dr. Sarah Brookes, Kevin Blum, Will

Hoggatt, Lauren Watkins, Clarissa Stephens, David Sohutskay, Rachel Morrison, Stephanie Thiede, Xiaohong Tan, Daniel Romary, Madeline McLaughlin, Mahera Husain, Evan Surma, John Nicholas, and Ajay Nachiappan. Thank you all for providing me with feedback on my research approaches and presentations. Additionally, all of you made going to lab that much easier with the goofy antics and lighthearted jokes. Catherine, thank you for showing me the ropes in the lab. Whether it was cell/tissue culture or collagen prep, you provided me with very patient instruction despite my inability to stay within my own personal bubble. Furthermore, your research laid the foundation for my research, and I am grateful for that. I also appreciate all of the feedback you have given me with writing and presenting. Rucha, thank you for your friendship and mentorship over the years. I will never forget when you bought me a badminton racket just so you could destroy me on the courts. I also appreciate your guidance in the lab whether it was collagen prep or teaching me how to order things. You took the most detailed notes! Thank you for being the happiest person and having such an uplifting spirit. Together, Catherine and Rucha have been like my older sisters here at Purdue and I am very grateful for their guidance. Nimisha, AKA (lab) wifey, I am thankful for your comradery at Purdue. I will never forget the countless all-nighters writing at MJIS or troubleshooting cell-cultures. Also, thank you for making desserts for everyone on their birthday – they were always delicious. Mentoring Stephanie with you was a fun and productive experience. I want to thank Will for being an awesome lab mate and an even better roommate. Lauren, thank you for the bike trips, it was a good breath of fresh air. TJ, the ice to my fire, I appreciate you being there from the start; we went through a lot together during our first years. Clarissa, thank you for being the cleaning machine that you are. Sarah, I appreciate all of the insight you have given me regarding animal studies. You are the first person I go to when I need information on animal-related information. Rachel, you are always in the way (inside joke). All jokes aside, I appreciated our conversations and related banter. David, my fellow Buckeye, I am glad we were able to work together on developing the animal model. I appreciate all of the fun facts you share on such a wide variety of topics. Thank you for playing Smash with me and being a worthy adversary in that regard. While the graduate students are there most of the time, I cannot forget the undergraduates.

I want to give a special thanks to the undergraduates of our lab; you have all contributed towards my ability to teach. Stephanie, you are the only reason why I root for Michigan. I appreciate your friendship and advice whenever I have come to you as well as our runs to Happy China whenever we had long days at MJIS. Ana Villanueva, thank you for being patient with me since I mentored you early on in my PhD. Daniel, thank you for being such a stellar mentee and for pushing translational research. Future work in my research area will surely rely on your contributions. Xiao, I appreciate the bubble tea during the final weeks leading up to my defense as well as the occasional ginormous snack from Costco. I also appreciate your banter and your shared passion for shoes. Thank you, John Nicholas, for teaching me how to use the ember 3D printing system. Overall, learning from other lab members has been an important aspect of my professional development, but branching out and learning from other research groups can be just as significant.

The advancement of science relies on collaborative efforts aimed to tackle the world's problems. I am very thankful for all of the opportunities I have had collaborating with other labs. I would like to thank Dr. Xuemei Chen, Dr. Justin Weibel, Mercy Dicuango, and Dr. Suresh Garimella for our collaboration to make collagen spheres using superhydrophobic surfaces. Mercy, thank you for being a great friend. I would not have had the idea of contacting your group had we not known each other. Xuemei and Justin, I enjoyed our weekly meetings to discuss research progress. Xuemei, thank you for taking time out of your day to teach me how to re-create the superhydrophobic surfaces. Dr. Garimella, thank you for giving me the opportunity to present our collaborative work to your entire group. Here, I could hone my communication skills, since I had to convey our biologically-related scientific findings to mechanical engineers. Overall, the experience with your group demonstrated the beauty of interdisciplinary collaboration. Dr. Nuri Damayanti is another collaborator I would like to thank. Nuri, thank you for being such an enthusiastic scientist and for taking the time to teach me about FLIM microscopy. I really enjoyed working with you as well as the conversations we shared. I would also like to thank Dr. Marisol Herrerra for her collaboration. We spent many hours on the confocal and I enjoyed all of the conversations we had during those times. I also want to thank Chris Shelley for not only sending us ECFCs when needed, but also for showing Nimisha and

me the ECFC extraction process. Overall, I am thankful for the opportunities to learn from other research groups.

In addition to collaborators, there are individuals that I would like to thank for teaching me new techniques. Thank you, Dr. Aaron Taylor, for helping me adjust to the Nikon confocal microscope over at Hansen when the confocal in MJIS went down. I appreciate all of your help with trying to push the boundaries of microscopy technology. I would also like to thank Bob Seiler for his help in cryogenic scanning electron microscopy as well as the many life conversations he shared during these imaging sessions. Thank you, Dr. Yuezhong Feng and Yinglong Chen for teaching me how to use the 3D printer over at the Mechanical Engineering school.

I want to thank all of the individuals who helped me develop my skills related to animal research. Carol Dowell, thank you for your instruction on all rodent-related methods. Additionally, thank you for taking time to provide me with one-on-one instruction on animal surgery. I want to thank the BME Veterinary Technician team. Specifically, I would like to thank Samantha Nier, Melissa Bible, Tina Cleary, and Bill Schoenlein for their guidance on the animal studies. You all provided helpful feedback on the animal protocol. Thank you Samantha for being in the trenches with us for our animal studies. You set a great example on how to respectfully conduct animal research. I am thankful that I could do this animal work with David. Your clinical knowledge has been invaluable. Also, I enjoyed all the time spent together – whether it was surgery, clean-up, bandaging, or analysis, we made a great team. I want to thank Dr. Scot Harbin for providing information on animal bandaging material. Additionally, I would like to thank Dr. Sunil Tholpady for his insight on rat bandaging techniques. Thank you, Gabriel Albors, Kelsey Bayer, and Kelsey Wasilczuk for providing us with many rat cadavers to practice our animal protocol. I also wanted to thank Sarah and Rachel, who took time out of their day to help when we needed extra hands.

Since beginning graduate school, my ability to communicate science through presentations and writing has improved dramatically thanks to many individuals. Sherry, thank you for taking the time to develop my communication skills. Whether it was writing or presenting, you have taught me how to adjust my communication styles to fit my audience. Thank you for giving me the opportunity to develop a course and to lecture in

front of students. I appreciated all of your advice related to teaching (i.e., delivery of lecture material, handling student concerns, or creating creative assignments). As a fellow TA, I want to thank Dr. Evan Phillips for his feedback on lectures. I also want to thank Dr. Luis Solorio for allowing me to teach lectures in BME 201. Dr. Corey Neu, Dr. Andrew Brightman, and Dr. Laurie Pinkert, thank you for the NSF writing class. Your dissection of my NSF proposal helped further develop my ability to write. Thank you, Catherine for your dedication to helping me write that NSF proposal along with many other documents. I want to thank Hetal Patel and Kristofer Buno for taking time out of their day to read through my documents and providing feedback. Thank you to the BME Graduate Student Association for all of the outreach opportunities. Communicating science effectively to middle schoolers has helped me to exercise my ability to simplify science so that it could be easily understood.

I could have never gotten to where I am without the wonderful faculty and staff within the Weldon School of Biomedical Engineering. I would like to thank Asem Aboelzahab, Dr. Rucha Joshi, and Dr. Lester Smith for their assistance with 3D printing and poster printing. Asem, you handled the majority of my requests and were able to turn them around rapidly, helping me meet research deadlines. You and Rucha gave me access to the undergraduate labs and tools, giving me freedom to achieve my research goals. I want to thank Norvin Bruns, Kirk Foster, and David McMillan for their rapid fabrication skills as well as guidance when working in the machine shop. I must thank Susan and Bill for the annual training they provide, as well as the instruction they provide for maintaining building safety. Additionally, I want to thank you both for giving me temporary IDs whenever I had lost/forgotten mine. Susan, Bill, and Kirk have done an overall tremendous job of making sure research/lab needs are met. I would like to thank the lovely ladies within the Business office. Carla Brady and Pamela Lamb, you have been tremendously helpful when I needed to order supplies last-minute. Thank you Linda Clark for helping me figure out travel-related costs as well as payroll information. Thank you to the custodial staff of the Weldon school. Specifically, thank you, Amanda Dalton, for your service and for all of our random discussions. I want to thank Jo Gelfand for not only helping me reserve rooms in MJIS, but also for her goofy demeanor that brightens up the building. Thank you, Kathryn Cooper for helping me set up conference calls and for your conversations. Dr.

David Umulis, I appreciated our friendly rivalry between the Ohio State University and University of Michigan. I do apologize that Michigan has not won a game against Ohio State during our shared time at Purdue. I also thank you for introducing me to Cornish pasties. My taste buds will never be the same. I want to thank all the individuals who handle shipments to MJIS, which includes Dan Wasmuth, Susan, and Charlotte Bell. I want to thank Tammy Siemers for setting up the annual industry tours. The tour opened my eyes to the variety of opportunities available to BME students. Last, but not least, I would like to thank Sandy May for her guidance in navigating graduate school. You have done an exceptional job keeping me on task for graduation. Overall, the community surrounding the Weldon School is not only extremely helpful for accomplishing research, but also provides a friendly, fun-loving environment that enhances the graduate student experience at MJIS.

I must also thank my funding sources as well as travel grants: National Science Foundation Graduate Research Fellowship (NSFGRFP; DGE-1333468), National Heart, Lung, and Blood Institute (NHLBI), the Purdue Doctoral fellowship, Purdue Graduate Student Association Travel Grant.

Lastly, I must thank my family and friends for their support. They have been there through thick and thin: boosting me up when my morale was low, but also celebrating with me upon reaching major milestones. I want to especially thank my parents for their love and support throughout my whole life. They have put my brothers and me before themselves and I could not be more grateful. I also want to thank my older brother, Karl, for setting a great example through his success. I appreciate your advice on meditation and being present, which have both helped me cope with hardships through graduate school. I also thank my younger brother, Kris, for inspiring me through his academic achievements and desire to learn. Overall, I am very lucky for all of the people in my life. I would not be who I am or where I am without all of them.

TABLE OF CONTENTS

LIST OF TABLES

LIST OF FIGURES

ABSTRACT

Author: Buno, Kevin, P. PhD
Institution: Purdue University
Degree Received: December 2018
Title: Cell-matrix Tensional Forces within Cell-Dense, Type I Collagen Oligomer Tissue Constructs Facilitate Rapid *In Vitro* Vascularization of Dense Tissue Constructs for Skin Engineering
Committee Chair: Sherry Voytik-Harbin

The skin provides protection and maintains homeostasis, making it essential for survival. Additionally, skin has the impressive ability to grow, as observed in children as they grow into adults. However, skin functions are compromised in large skin defects, a serious problem that can be fatal. The gold standard treatment is to use an autologous skin graft; however, due to donor site morbidity and limited availability, when full-thickness defects surpass 2% total body surface area (TBSA), skin substitutes are preferred. Unfortunately, current skin substitutes on the market: are slow to revascularize (2+ weeks), have low graft survival rates (<50% take), and lead to significant scarring and contracture. Fortunately, a promising solution is to prevascularize engineered skin substitutes *in vitro*, which has been shown to facilitate rapid tissue integration upon grafting by providing an intact vascular network that readily connects to the host's circulation. However, current approaches for prevascularizing tissue constructs require long *in vitro* culture times or implement low extracellular matrix (ECM) density tissue constructs – both which are problematic in a clinical setting. To address this, we implemented a novel multitissue interface culture model to define the design parameters that were essential for rapid vascularization of soft tissue constructs *in vitro*. Here, we identified endothelial colony forming cell (ECFC) density and maintenance of cell-matrix tensional forces as important factors for rapid *in vitro* tissue vascularization (18% vessel volume percentage after 3 days of culture). We then applied these parameters to achieve rapid *in vitro* vascularization of dense, oligomer tissue constructs (12, 20, and 40 mg/mL). We demonstrated, for the first time, rapid *in vitro* vascularization at 3 days within dense matrices (ECM concentration > 10 mg/mL). Lastly, a rat full-thickness excisional wound model was developed to determine the acellular densified oligomer's (20 and 40 mg/mL) ability to resist wound

contraction and facilitate a wound healing response (recellularization and vascularization) when grafted into wounds. Future work will implement the vascularized, dense tissue constructs into the developed animal model to assess the vascularized graft's efficacy on treating wounds to reduce scarring and contracture outcomes.

CHAPTER 1. INTRODUCTION

1.1 Introduction

Skin serves as the organismal interface with the environment, offering protection from infection and maintaining homeostasis (i.e., temperature and fluids). Furthermore, skin demonstrates its remarkable ability to grow while maintaining its function, as shown when children grow into adults[1], [2]. While full-thickness skin defects present known challenges in adults, it is skin loss within children, which occurs for a number of reasons, including trauma, burns, oncologic resection, and congenital anomalies, that brings forth additional complications as the child grows. The current gold standard of care for patients suffering from full-thickness defects is to implement autografts. However, if the autografted dermis does not contain enough blood vessels, these grafts are not able to grow with the patient. Additionally, when patients experience wounds that are too large (>20% total body surface area), there is limited availability and donor site morbidity[3] – therefore, skin substitutes are needed. The current procedure for skin substitutes starts with suturing the skin substitute into the wound. Since skin substitutes on the market are not vascularized, they must be thoroughly vascularized by the host's body, after which an epidermal layer can be added[4]. Unfortunately, current skin substitutes on the market are slow to revascularize (2+ weeks), since angiogenesis-related in-growth of vessels moves at a rate of roughly 5μm/hr[5]. Additionally, the time required for revascularization is prolonged when thicker dermal substitutes are used. Overall, the current procedure for applying skin substitutes is lengthy, requiring multiple steps and results in poor take rates (<50%), scarring and contracture, and growth limitations[6]–[9]. Clinical observations have demonstrated that a vascularized tissue grows with a child[10], [11]; therefore an engineered skin replacement that is rapidly vascularized would adapt with a growing child.

Skin is the largest organ of the body and relies on its vasculature to supply nutrients to support its many functions. The skin i.) protects internal organs from the outside world (i.e., chemicals, bacteria, physical), ii.) regulates homeostatic processes (i.e., thermoregulation, fluid balance), and iii.) facilitates the sensation of our surroundings. Additionally, skin demonstrates its remarkable ability to grow with patients as observed in

growing children. The **epidermis** (0.07 mm to 0.6 mm thick) is the outermost layer of the skin and is responsible for barrier function. This layer is comprised mostly of keratinocytes and is characterized by layers of keratin supported by an underlying basement membrane. The epidermis does not contain any blood vessels; therefore, the keratinocytes must receive nourishment from blood vessels of the underlying dermal layer. The **dermis** (0.6mm to 3mm) is responsible for the skin's mechanical properties and contains many of the functional structures of the skin (i.e., glands, follicles, vasculature). These structures receive their nourishment from the microvasculature (capillaries). As one moves deeper into the skin, the dermis transitions into the **hypodermis** (AKA fat or subcutis), which contains adipocytes (fat cells), fat, and is well vascularized. The vasculature in the hypodermis are made up of arteries and veins and provide the bulk supply of blood to the rest of the dermal vasculature. Overall, analyzing the hierarchical assembly of skin in terms of structure and function highlights the importance of the vasculature when engineering next-generation full-thickness skin substitutes. The ideal engineered skin substitute should contain ECM and cellular components associated with rapid vascularization to facilitate rapid restoration of normal skin functions (i.e., barrier function, thermoregulation, ability to grow).

At present, pediatric patients are treated the same as adults, which is problematic when evaluating post-operative patient quality of life. The gold standard for skin defects is to treat the patient with an autologous split thickness skin graft (STSG) that is taken from another location on their body. STSGs contain the entire epidermis and only part of the dermis, while a full thickness skin graft contains both the entire epidermis and dermis. Once the skin graft is applied, successful take relies on the graft's access to nutrients via a step-wise occurrence of: i.) plasmatic imbibition, ii.) vascular anastomosis, and iii.) revascularization[12]. When a skin graft is placed onto the wound, it initially receives nourishment from the wound plasma in a process known as plasmatic imbibition ("drinking plasma"). Over the next 24 to 72 hours, vascular anastomosis is observed, where the host's blood vessels grow into the graft and connect with the graft's vessels. Once the vessel networks are connected, the mode of graft cell nourishment transitions from plasmatic imbibition to normal (and more effective) capillary blood vessel diffusion. Around 4-6 days after grafting, the whole tissue is revascularized. This three-step process determines

graft take success and precedes key regenerative processes such as re-epithelialization and re-innervation.

Graft characteristics are an important determinant of successful outcomes in terms of reducing scarring and contraction. STSGs may be used to cover large wounds, but they are not ideal since they lack most of the mechanically stable dermal layer. As such, successful graft take still results in scarring/contracture outcomes[13]–[15]. As mentioned earlier, this is especially bad for children because scar tissue is dense and inelastic, which hinders movement and does not grow[14], [15]. As such, the aesthetically unappealing scars result in continual suffering by growing pediatric patients who experience a painful recurrence of wound openings. Alternately, an ideal approach would be to apply a full thickness skin graft (FTSG) to the patient's wound, which includes the entire epidermal and dermal layers. Since it contains more of the mechanically stable dermal layer, successful FTSG take results in reduced scarring/contracture outcomes. Conversely, since FTSGs represent a more-complete graft (than STSGs), their usage is limited to wounds that encompass less than 2% of total body surface area. Therefore, autologous grafts are not sufficient due to limited availability and donor site morbidity[3]. These patients, especially children, need a skin substitute that reduces the occurrence of scarring/contracture events.

While many skin substitutes are commercially available (Table 1.1), there is still no permanent skin substitute for children suffering from large skin defects. While current skin substitutes on the market succeed in having i.) ideal handling characteristics, ii.) support for barrier function, and iii.) inductions/conduction of neodermal regeneration, no substitute on the market can grow with the patient[5], [16]. Tissue engineered skin substitutes replace the need for autologous grafts, and different types exist to address various wound types/locations: epidermal, dermal, and dermo-epidermal substitutes. **Epidermal substitutes** (AKA cultured epithelial autografts; Epicell, ReCell) consist of autologous keratinocytes (the predominant cell in the epidermis) that are harvested from the patient, grown *in vitro* for three weeks, and subsequently applied onto the wound site[17]. While the use of an autologous cell source reduces immunogenicity, this approach is hindered by long prep times (3 weeks), low success rates (<50% take), tissue fragility, and scarring/contracture outcomes[8], [9]. In contrast, **dermal substitutes** (Integra®, AlloDerm®, Matriderm®) provide more mechanical integrity, which reduces the amount

of scarring/contraction when compared to epidermal grafts[18]. These thick scaffolds are comprised of type I collagen, the predominant ECM protein in the skin, and are either acellular or cellular (allogenic fibroblasts). Dermal substitutes must be paired with a STSG to complete the graft and provide barrier function. However, unlike native dermis, the dermal substitutes are not vascularized. Therefore, after grafting thick dermal substitutes (>1mm), clinicians must wait 2-3 weeks for the dermal substitute to be sufficiently vascularized before adding an STSG or an epidermal substitute on top[19], [20]. Prematurely adding the epidermal component results in graft failure via tissue necrosis due to insufficient access to nutrients[4]. As vessels grow into the dermal substitute, so do other cell types, including fibroblasts, fibrocytes, and inflammatory cells. The recellularization process contributes to wound contraction[21]. Despite the care and consideration taken for this two-step approach, these transplants still suffer from low success rates and scarring/contraction[8], [9]. Lastly, **dermo-epidermal** substitutes (Apligraf, Orcel), contain an allogenically cellularized epidermis (keratinocytes) and a mechanically fragile dermis (fibroblasts). Similar to the aforementioned skin substitutes, these still require remodeling, recellularization, and vascularization by the host, which contributes to wound contraction[22]. Furthermore, this approach is expensive and timely[23]. In conclusion, the overarching problem of commercially available skin substitutes are that they are **timely** (requiring multiple steps), **ineffective** (<50% graft take), and **do not grow with the patient** (due to scar tissue formation)[8], [9]. We believe these problems can be overcome by creating skin grafts that i.) are sufficiently vascularized and consist of an ECM that is ii.) biocompatible and iii.) mechanically stable.

Table 1.1 Summary of commercially available treatments for large skin defects

Products	ECM material	Cellular component	Indication	Disadvantages
Dermal Substitutes				
Alloderm	Decellularized human dermis	-	Burns and full-thickness wounds	-May contain immunogenic residual allogeneic cell remnants
Matriderm	Decellularized bovine dermis	-	Full-thickness burns	-May transmit diseases
Integra	Collagen-GAG sponge	-	Deep partial thickness and full thickness burns	-Infection -Hematomas -Seromas
Epidermal substitutes				
Epicell	-	Cultured autologous keratinocytes	Deep partial- and full-thickness burns	-Fragile, requires dermal support -Variable take rates -Poor long term results
ReCell	-	Autologous, highly-proliferative keratinocytes	Reduce need for donor site in deep dermal defects	
Dermo-epidermal substitutes				
Apligraf	Acid-extracted, Bovine Type I Collagen	Allogenic keratinocytes and fibroblasts	Ulcers (venous leg and diabetic foot)	-Allogenic cell sources are eventually lost 1-2 months after grafting -Cannot treat full thickness burns due to lack of mechanical integrity

Our long-term goal is to employ advanced tissue fabrication techniques for creating regenerative skin replacements that rapidly integrate and generate fully functional skin that adapts with the growing patient. This thesis focused on the design of the dermal component with an emphasis on deciphering mechanobiology mechanisms for promoting vessel formation *in vitro* and *in vivo*. Important design requirements for this dermal component of the regenerative skin replacement include: biocompatibility, mechanical stability, and rapid vascularization. The regenerative dermal replacement will utilize type I collagen, which is advantageous since, in its fibrillar form, collagen determines the structural and mechanical properties of skin[24]. Specifically, type I collagen oligomeric collagen, will be used. Unlike other self-assembling collagens, such as monomeric telo- and atelocollagens, oligomeric collagen contains intermolecular crosslinks that result in tissue constructs with improved mechanical integrity, polymerization times and reproducibility[25], [26]. Furthermore, unlike decellularized tissues or collagen sponges, oligomeric collagen retains cell signaling properties through its inherent cell and molecular binding domains without the concern for immune rejection. As such, the oligomer collagen matrix offers a promising solution by providing a microenvironment where cells have remained viable and have responded to local matrix mechanophysical cues by displaying altered morphology, cytomechanics, phenotype, and tissue morphogenesis[27]–[29]. To further enhance the mechanical integrity of the biomaterial, a densification process will be

employed[28], [29]. When oligomer collagen self-assembles into a matrix, it consists of interconnected collagen fibrils with interstitial fluid in between. During densification, a confined compression is used to control fluid removal from the tissue construct, resulting in tissue constructs resembling soft connective tissues in terms of collagen density, higher-order interfibril associations, and mechanical properties. The densification process facilitates the creation of physiologically dense tissue constructs (40 mg/mL collagen concentration) while maintaining the ability to readily encapsulate cells throughout the ECM, a feat that is unachievable within top-down tissue engineering approaches. The use of confined compression to modulate fibril architecture and mechanical properties of the engineered tissue without compromising collagen's biological signaling properties provides significant advantages over conventional collagen processing techniques. Specifically, promiscuous exogenous crosslinking agents (i.e., glutaraldehyde, dehydrothermal treatment, ultraviolet radiation, enzymatic crosslinking) have been used to strengthen collagen tissue constructs, which have been shown to induce cytotoxicity, protein denaturation, inflammation, and can mask cell binding sites[30]–[33]. In addition to the matrix component, endothelial cells (EC) will be added for rapid vessel formation to facilitate successful graft take and growth with the patient. Specifically, the ECs will form vessels via vasculogenesis, or the de novo formation of blood vessels. Here, ECs are encapsulated within an extracellular matrix (ECM), and these individual ECs migrate, form vacuoles, coalescence into vessels, and eventually mature/stabilize. Early *in vitro* vasculogenesis models primarily employed human umbilical vein endothelial cells (HUVEC) due to their accessibility and ease of expansion[34]. However, their mature phenotype results in limited proliferative and vessel-forming capacity and tends to regress shortly (~48 hrs) after suspension within a 3D ECM[35]. Alternately, endothelial colony forming cells (ECFCs) display high clonogenic and proliferative potential as well as robust vessel forming capacity[36]. When compared to HUVECs, ECFCs form a higher density of vessel networks *in vitro*[37]. As such, to achieve rapid vascularization of the oligomer tissue constructs, we will encapsulate endothelial colony forming cells (ECFCs). This pairing has been shown to form vessels that continue to persist after 2 weeks of culture *in vitro*[38]. Furthermore, previous work in our lab has shown that matrix mechanophysical features, like collagen-fibril microstructure and stiffness, guides human vessel

morphogenesis by ECFCs both *in vitro* and *in vivo*[38]–[40]. It has also been shown that prevascularization of a tissue construct results in rapid anastomosis when grafted onto animals[41]. While vascularization of these tissue constructs has been achieved, the employed ECMs are relatively less-dense than physiologic skin (1.0-3.0 mg/mL vs. 40 mg/mL)[42], [43]. As mentioned earlier, graft characteristics, such as mechanical stability, are important for reducing scarring and contracture outcomes. Therefore, what is needed is a method to vascularize physiologically dense tissue constructs.

Current research approaches aimed at prevascularizing skin substitutes *in vitro* are slow (2-4 weeks) and do not employ mechanically stable ECMs. The majority of approaches are either top-down or bottom-up. Top-down approaches implement prefabricated scaffolds, such as collagen sponges and decellularized tissues, that are seeded with ECs[44]–[48]. Due to the dense nature of these prefabricated scaffolds, ECs aggregate at the periphery of the scaffold and employ simulated angiogenesis to slowly vascularize the scaffold. Unlike vasculogenesis, angiogenesis is the formation of blood vessels from a pre-existing vessel network. The dense aggregation of ECs mimics a blood vessel wall that invaginates, which initiates blood vessel sprouting into the tissue construct. However, ECs are typically seeded on one side of the tissue construct, so vessels must grow through the entire thickness of the scaffold to fully vascularize it. On the other hand, bottom-up approaches employ vasculogenesis. Here, ECs are encapsulated within a soluble ECM that is subsequently polymerized, holding ECs in their 3D conformation[42], [43], [49]–[51]. ECs are dispersed throughout the ECM and begin to individually form vessels via vasculogenesis. As vessel networks form throughout the tissue construct, they eventually anastomose with one another, forming an interconnected vascular network throughout the tissue construct. As such, employing vasculogenesis is favorable over angiogenesis since vascularization concurrently occurs throughout the entirety of the tissue construct. Although the vasculogenesis approach seems ideal, these approaches still implement low-density ECMs (3-6 mg/mL collagen) that are more prone to tissue contraction. As such, current tissue culture methods are cell density-limited: increased cell densities result in tissue contraction. When tissues contract, cell-matrix tensional forces are lost, resulting in EC vessel regression[52]. We believe that increasing the EC density while maintaining

cell-matrix tensional forces will enhance vessel formation by bringing cells closer together and providing mechanotransductive signaling cues for survival.

1.2 Organization of thesis

This dissertation aims to show the process by which the critical design parameters, specifically cell-matrix tensional forces and ECFC density, can be applied to modulate *in vitro* ECFC vessel formation within tissue constructs at a variety of ECM densities. Cell-matrix interactions have been identified as a critical design parameter for tissue vascularization[39], [52], [53]. Specifically, not only can ECs sense the type of ECM, but they also sense the mechanical stiffness through their integrins using mechanotransduction signaling pathways[54]. Furthermore, when the cell-matrix interactions are unbalanced, vessel formation is compromised. In the case for imbalance towards matrix interactions, it has been previously shown that increasing the ECM density inhibits vessel formation[52], [55]–[58]. During vessel formation, ECs must degrade their surrounding ECM to clear a path for nascent vessel sprouting and branching. Therefore, when the ECM density is too high, the ECM poses a physical barrier to neovascularization. On the other end of the spectrum, when cells dominate the cell-matrix tensional force balance, cell-mediated tissue contraction is observed[52]. As the cell density of a tissue culture is increased, so is the collective traction forces within the tissue construct. When the collective traction force within the tissue construct exceeds its adhesion force to the well plate, the tissue construct separates from the wall. Here, cell-mediated tissue construct contraction is initiated, cell-matrix tensional forces are lost, and the encapsulated ECs regress. We hypothesized that maintaining these cell-matrix tensional forces under high cell density conditions would provide ECFC with signaling cues for rapid and extensive vessel network formation. Furthermore, we hypothesized that implementing these design criteria within denser ECMs (>10 mg/mL collagen concentration) will enable the rapid vascularization of dense tissue constructs *in vitro*, a feat that remains unachieved. By increasing the ECFC density within dense ECMs, the cell-matrix tensional forces are more balanced, favoring vessel formation. In **Specific Aim 1**, we defined the critical design parameters for rapidly vascularizing low-density tissue constructs (<10 mg/mL collagen concentration) *in vitro*. Here, the multitissue interface model was proposed, and is the method used to maintain cell-matrix

tensional forces. In **Specific Aim 2**, we defined cell signaling within the rapidly formed vessels created in Aim 1. **Specific Aim 3** employed knowledge gained from Aims 1 and 2 to rapidly vascularize densified oligomer tissues (>10 mg/mL collagen concentration). Lastly, **Specific Aim 4** details the development of a rat wound model that was used to define wound healing response to densified oligomer tissue constructs.

CHAPTER 2. IN-VITRO MULTI-TISSUE INTERFACE MODEL SUPPORTS RAPID VASCULOGENESIS AND MECHANISTIC STUDY OF VASCULARIZATION ACROSS TISSUE COMPARTMENTS

2.1 Overview

Here, we detailed the development of a novel culture model that overcomes limitations of current tissue culture models and allowed us to achieve Specific Aim 1: To define the critical design parameters for rapidly vascularizing low-density tissue constructs (< 10 mg/mL collagen concentration) *in vitro*. The story begins with the goal of rapidly vascularizing less dense tissue constructs, because this range has been shown to facilitate vessels formation. The novel tissue culture system we developed is the multitissue interface model. Unlike conventional tissue cultures, the multitissue interface culture system allowed the encapsulation of a high density of endothelial colony forming cells (ECFC) ($\geq 2\times10^6$ cell/mL) within a tissue construct in absence of cell-mediated tissue contraction. As such, cell-matrix tensional forces were maintained and extensive vessel formation was observed in 3 days. This model enabled us to study ECFCs in a context that was not previously possible. In this work, we determined that the critical design parameters for vascularizing less-dense tissue constructs was: i.) maintaining cell-matrix tensional forces, ii.) increasing ECFC density, and iii.) addition of adipose stromal cells (ASC) to the culture. Defining the critical parameters for rapidly vascularizing these less-dense tissue constructs set the foundation for rapid vascularization of a denser tissue construct that may serve as a dermal substitute. As mentioned previously, vascularization is a key determinant of skin graft success. The sooner that the tissue constructs can be vascularized, the better the patient outcome will be. This work was published and featured as a spotlight application in in the *American Chemical Society: Applied Materials and Interfaces*.

2.2 Introduction

A significant challenge facing tissue engineers is the design and functional assembly of complex multitissue systems, including vascularized tissue−tissue interfaces[59], [60]. Such systems are typically composed of multiple cell types arranged

and organized with boundaries or within gradients of extracellular matrix (ECM) components to perform specific functional roles[61]. Moreover, incorporating functional vasculature within such multitissue systems is essential to their scalability, long-term tissue survivability, and effective integration with host tissues upon implantation[62]. It is now recognized that a complex interplay of biochemical and biophysical cues is involved in tissue morphogenesis[63], and new design approaches to support the construction and optimization of vascularized tissue–tissue interfaces are needed.

To create complex, vascularized tissue-engineered constructs, the guiding mechanisms of blood vessel formation, maturation, and stabilization must first be understood. Neovascularization, as occurs *in vivo* during embryonic development and throughout adult life, involves two primary processes, namely, vasculogenesis and angiogenesis[63], [64]. Vasculogenesis represents the *de novo* self-assembly of vessel networks by endothelial cell precursors, making it ideally suited for tissue engineering strategies. Angiogenesis involves the sprouting and elongation of new vessels from pre-existing vasculature, a process necessary for facilitating functional anastomosis, or hook-up, between the vascularized tissue construct and the host vasculature.

A number of critical steps and mechanisms underlying vasculogenesis and angiogenesis have been defined using various three-dimensional (3D) *in vitro* vascularization models. For example, angiogenic capillary sprouting is observed when endothelial cells (ECs) are cultured as a monolayer atop the surface of a 3D ECM substrate[65] or sandwiched between substrate layers[66], [67]. Capillary sprouting also occurs from aortic rings[68], microvessels[69], EC-coated microbeads[70], or EC aggregates/spheroids[71], [72] embedded within substrates. Collectively, angiogenesis involves invasion of physiologically relevant substrates, such as interstitial fibrillar type I collagen or fibrin, by activated ECs of existing vessels or monolayers; this requires limited matrix proteolysis, proliferation, migration, and lumen formation and stabilization[73]. In contrast, *in vitro* models of vasculogenesis involve monodispersion of ECs or their progenitors, where individual cells are homogeneously distributed within a 3D substrate (Figure 2.1A,B)[74]–[76]. Here, programmed events associated with vasculogenesis include vacuole formation, vacuole coalescence to form multicellular lumens, and vessel maturation and stabilization[77]. These 3D *in vitro* models, together with corroborating *in*

vivo evidence, show that vessel morphogenesis is modulated by a complex series of events involving cell–cell, cell–ECM, growth factor, and morphogen signaling[78].

While these 3D *in vitro* models have provided mechanistic insight into vascularization processes, they are limited in their ability to define critical design parameters necessary for vascularization of tissue-engineered constructs and, more importantly, vascularization across tissue–tissue interfaces. For example, tissue construct contraction, which results from cell–matrix traction forces, is often associated with high cell densities and/or low-mechanical-integrity substrates[52], [79]. Such contraction events affect vessel morphogenesis outcomes by altering the mechanical boundary conditions of the tissue construct[52], [80], compromising the overall vessel network morphology, tissue histology, and scalability. Improved definition and standardization of critical design parameters, including cell type, cell seeding density, medium composition, substrate composition, substrate physical properties, and mechanical boundary conditions, are needed to ensure robust and reproducible functional performance of vascularized tissue engineered constructs for both research and clinical applications[75], [81].

The present study features a design approach that utilizes, for the first time, biphilic wettability surfaces having hydrophilic regions patterned onto a superhydrophobic background to direct the formation of spherical cell–collagen tissues. Such spherical cell–collagen tissues can be readily integrated into a second tissue for creation of a multitissue interface *in vitro* (Figure 2.1C,D). This approach enables independent specification of each tissue's interstitial collagen-fibril ECM and resident cell populations, including type and density. This new culture model was applied to test a hypothesis that independent control of cell–ECM and cell–cell interactions would affect vessel morphogenesis within a component tissue as well as across the tissue–tissue interface. An essential element of the design approach is the application of type I collagen oligomers, which represent a soluble collagen formulation that self-assembles to form collagen-fibril matrices with higher-order interfibril associations. As such, the supramolecular assembly of oligomers supports the creation of collagen–fibril matrices with a broad range of structural and mechanical properties (specified by fibril density and matrix stiffness) beyond those that can be achieved with conventional collagen monomers, atelocollagen, and telocollagen[25], [39], [82], [83]. Furthermore, embedding oligomer-based tissue

spheres within an oligomer-based surrounding tissue facilitates the creation of a tissue–tissue interface that maintains stability even in the presence of high cell densities, which may be necessary to replicate certain physiological conditions.

Previously, oligomer collagen-fibril matrices have been shown to provide the necessary mechanobiological cues to induce and guide monodispersions of endothelial colony forming cells (ECFCs) to form lumenized vessel networks stabilized by a basement membrane both *in vitro* and *in vivo*[39], [40]. In the present work, the multitissue interface method is applied to culture ECFCs at unprecedented densities, thereby accelerating vessel morphogenesis to within 3 days. This culture model also demonstrates that the ECFC density and crosstalk between ECFCs and adipose-derived stromal cells (ASCs) across a tissue–tissue interface play critical roles in not only determination of the vessel network morphology but also stabilization of vessels formed within and across tissue compartments. Controlling and optimizing relevant design features associated with multitissue interfaces, specifically the structural and mechanical features of the collagen-fibril matrix as well as the cell composition and density, may assist the development of vascularized tissue interfaces for a diverse range of tissue engineering applications.

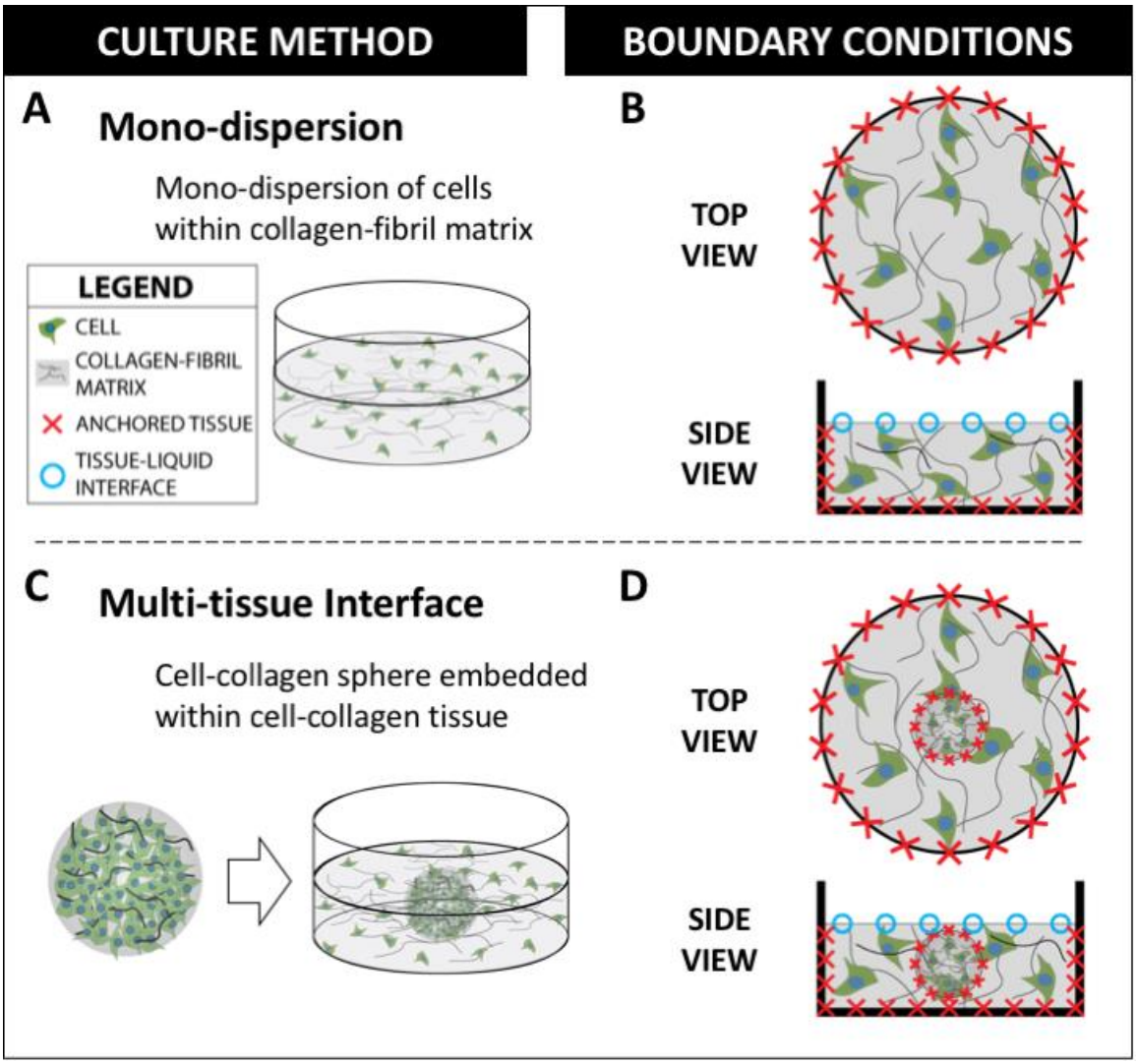

Figure 2.1 The multitissue interface model contained a collagen sphere tissue that was fully anchored (100% surface area) to the surrounding collagen, which enhanced its ability to resist contraction and maintain cell-matrix tensional forces. (A, C) Schematic diagrams and (B, D) boundary conditions for (A, B) homogeneous monodispersion and (C, D) multitissue interface culture formats. Monodispersion cultures involve homogeneous distribution of cells within a surrounding collagen-fibril matrix. Multitissue interface cultures are created by embedding a cell–collagen tissue sphere within a surrounding cell–collagen tissue construct.

2.3 Materials and Methods

2.3.1 Fabrication of Biphilic Surfaces with Spatially Nonuniform Wettability

Wettability. Superhydrophobic surfaces were fabricated on Si substrates using a metal-assisted chemical etching method[84]. The surface was first etched with 5% HF

aqueous solution for 3 min to produce a hydrogen-terminated substrate and then immersed into an aqueous solution containing 4.8 M HF and 5 mM $AgNO_3$ for 1 min to create a uniform layer of Ag nanoparticles. The surface was rinsed with water to remove surplus Ag^+ and then immersed in an etchant composed of 4.8 M HF and 0.4 M H_2O_2 for 30 min. After etching, the Si substrate was washed repeatedly with water and immersed in dilute HNO_3 (1:2 HNO_3/deionized water) for 30 min to dissolve the Ag catalyst. As a result of this process, Si nanowires were grown uniformly across the substrate. To render the surface superhydrophobic, the sample was silanized through immersion in a 1 mM n-hexane solution of 1H,1H,2H,2H-perfluorooctyltrichlorosilane for 1 h followed by heat treatment at ~150 °C on a hot plate for 1 h. The static apparent contact angle and roll-off angle of the as-fabricated surface were measured to be ~165° and <1°, respectively, using a rame-hart (Succasunna, NJ) model 590 goniometer; while a spherical droplet was formed upon deposition on the surface, these highly nonwetting characteristics prevented reproducible attachment and positioning of droplets on the surface.

In order to facilitate the formation and adhesion of spherical collagen and cell–collagen droplets on the surface, laser-assisted surface treatment was used to selectively create hydrophilic regions on the superhydrophobic background. An array of dots (0.9 mm diameter dots with a center-to-center spacing of 4.5 mm) was generated on the surface using a commercial CO_2 laser-engraving system (PLS6MW, Universal Laser Systems, Inc., Scottsdale, AZ; 75 W, laser wavelength = 10.6 μm). The system was used to inscribe the desired pattern on the substrate by raster-scanning the laser beam across the surface at a speed of 0.2 m/s with 400 pulses per inch. The laser irradiation rapidly increases the local temperature and removes the superhydrophobic surface-coating material, generating hydrophilic dots to which droplets can attach.

The biphilic surfaces were exposed to two different sterilization techniques, including an autoclave (121 °C, 15 atm, 15 min) and 80% ethanol diluted in Milli-Q water (15 min). Surfaces that received the 80% ethanol treatment were rinsed thrice in sterile phosphate-buffered saline (PBS) and then air-dried. Contact angle measurements of water droplets (5 μL) were taken before and after the sterilization treatments. Surfaces were tested in triplicate (n = 3), and the results were compared using a paired t test.

2.3.2 Preparation of Type I Collagen Oligomers

Type I collagen oligomers were acid-solubilized from the dermis of market-weight pigs and lyophilized for storage as described previously[39]. The oligomer formulation was standardized on the basis of molecular composition as well as polymerization capacity according to ASTM International standard F3089-14[85]. Here the polymerization capacity is defined by the matrix shear storage modulus, G′ (in Pa), as a function of oligomer concentration in the polymerization reaction. Each collagen solution was diluted with 0.01 N HCl to achieve the desired concentration and neutralized with 10× PBS and 0.1 N NaOH to achieve pH 7.4[86]. Neutralized solutions were kept on ice prior to induction of polymerization by warming to 37 °C.

2.3.3 Validation of Collagen Sphere Geometry and Reproducibility

Type I collagen oligomers were diluted in 0.01 N HCl and neutralized to stiffness values of 0, 200, and 1000 Pa, which correspond to final oligomer concentrations of 0.0, 1.4, and 2.9 mg/ mL, respectively. Air-displacement (Pipetman, Gilson Inc., Middleton, WI) and positive-displacement (Microman, Gilson Inc.) pipettes were used to dispense oligomer at specified volumes of 5, 10, and 15 μL onto the hydrophilic spots of the biphilic surface, resulting in sphere formation (Figure 2.2). For each experimental group, triplicate spheres were formed (n = 3). Sphere volumes were measured from goniometer images, and the sphere geometry was characterized by the droplet height-to-width aspect ratio (ImageJ, NIH, Bethesda, MD):

$$Aspect\ Ratio = \frac{H_{sphere}}{W_{sphere}} \qquad (1)$$

where H_{sphere} and W_{sphere} represent the height and width of the oligomer sphere, respectively. An ideal sphere would have an aspect ratio of 1; the amount of reduction below 1 indicates the degree of sphere distortion.

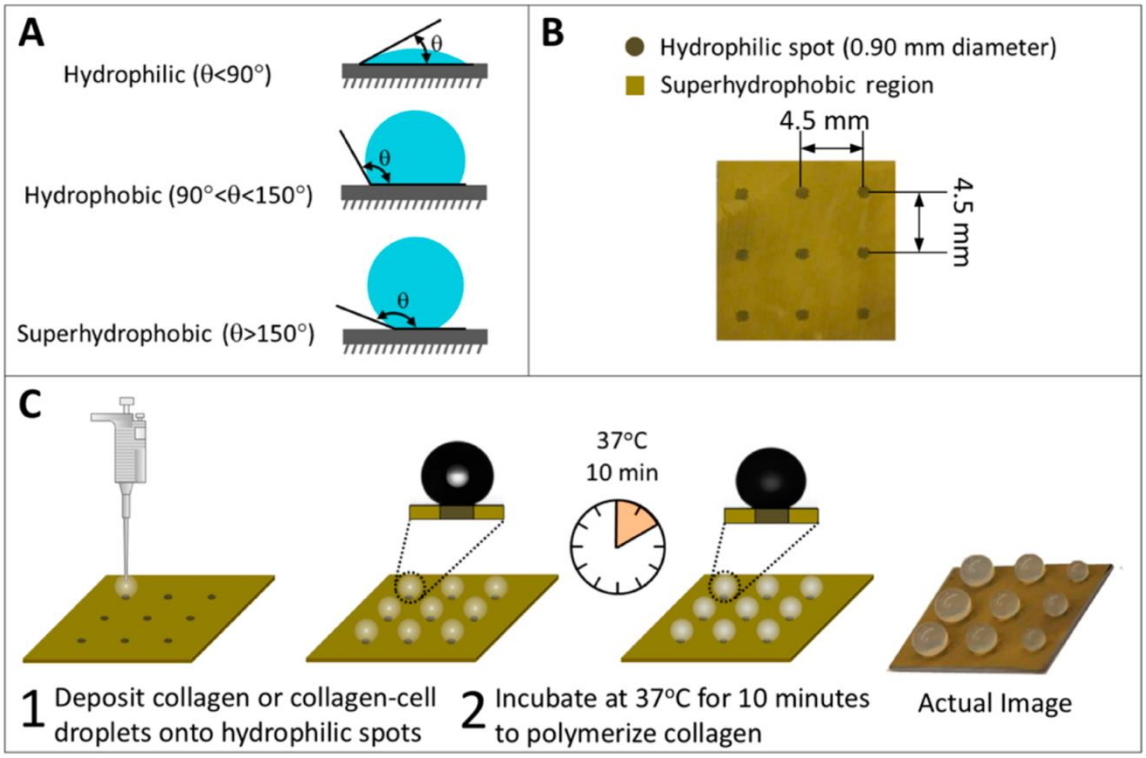

Figure 2.2 (A) Schematic diagram demonstrating interactions of a droplet with surfaces having uniform wetting properties. (B) Biphilic surfaces with hydrophilic spots surrounded by superhydrophobic regions used to form collagen or tissue spheres. The superhydrophobic areas facilitate sphere formation, while the hydrophilic spots assist in deposition and adhesion of spheres to the substrate. (C) Overview of the tissue sphere formation process. Aliquots of neutralized oligomer solution in the presence or absence of cells are deposited onto the hydrophilic spots of the biphilic surface. The surface is subsequently placed into a humidified 37 °C incubator to induce self-assembly of collagen fibrils (polymerization). The rightmost photograph shows oligomer collagen spheres with volumes of 15, 10, and 5 μL formed on the biphilic surface

2.3.4 Cell Culture

Human ECFCs were isolated from umbilical cord blood and cultured as described previously[87]. Low-passage human ASCs were grown according to the manufacturer's instructions (Zen-Bio, Research Triangle Park, NC). Both ECFCs and ASCs were propagated in complete endothelial cell growth medium (EGM-2, Lonza, Walkersville, MD) supplemented with 10% fetal bovine serum (HyClone, ThermoFisher Scientific, Waltham, MA). Cells were grown and maintained in a humidified environment of 5% CO_2 in air at 37 °C. ECFCs and ASCs were used in experiments at passages between 8 and 13.

2.3.5 Preparation of 3D Monodispersion and Multitissue Interface Tissue Constructs

For the monodispersion format (Figure 2.1A,B), ECFCs were suspended in neutralized oligomer at a density of 0.5×10^6, 2×10^6, or 5×10^6 cells/mL. The oligomer−cell suspension was aliquoted into a 48-well plate (250 μL/well) and subsequently polymerized at 37 °C for 15 min.

For the multitissue interface format (Figure 2.1C,D), 5 μL aliquots of oligomer−cell suspension were pipetted onto the biphilic surfaces to create spheres, which were polymerized for 10 min at 37 °C. Next, the oligomer−cell suspension for the surrounding tissue was pipetted into 48-well tissue culture plates at 250 μL/well. A single polymerized oligomer−cell sphere was immediately placed in the center of each well, and the surrounding tissue was polymerized for 15 min at 37 °C. The volumes of the sphere and surrounding tissue microenvironment were selected such that the sphere was not in contact with the upper (liquid−air interface) and lower (cultureware) surfaces, ensuring uniform and highly reproducible tissue−tissue interactions and mechanophysical properties across the sphere surface area. All of the tissue constructs were cultured in complete EGM-2 medium in an incubator (5% CO_2, 37 °C) with daily medium replacements. All of the experimental groups were tested in triplicate (n = 3).

2.3.6 Assessment of Sphere and Overall Tissue Contraction

To monitor qualitative changes in the embedded sphere and tissue construct volume as a function of cell seeding density and time, macroscopic top-view images of the 48-well plate were taken at 0, 24, 48, and 72 h. The sphere boundary was identified in each image, and the sphere cross-sectional area was calculated using ImageJ. After 3 days of culture, tissues were rinsed thrice in PBS, fixed in 3% paraformaldehyde, and rinsed thrice again in 1× PBS. A volume displacement method was used to quantitatively measure the final tissue volume. Triplicate wells containing tissue constructs, along with three empty wells, were carefully filled with PBS. Next, the supernatant (PBS) from each sample was weighed using an analytical balance (BP 210 D, Sartorius, Elk Grove, IL). The known mass of the supernatant and the density of water at 21.5 °C (0.9979 g/mL) were used to calculate the supernatant volume, $V_{supernatant}$, which represents the volume in the well not occupied

by tissue. The volume calculated for the empty wells represents the total volume of each well, V_{well}. Subtracting $V_{supernatant}$ from V_{well} gives a measure of tissue volume:

$$V_{tissue} = V_{well} - V_{supernatant} \quad (2)$$

From initial tissue volumes, V_i, of 250 and 255 μL for the matrix-only and multitissue interface methods, respectively, the final tissue volume percentages were calculated:

$$\frac{V_{tissue}}{V_i} * 100\% = Final\ Tissue\ Volume\ \% \quad (3)$$

2.3.7 Immunostaining of 3D Tissue Constructs

Tissue constructs were fixed in 3% paraformaldehyde after 3 days of culture, permeabilized with 1% Triton X-100, blocked with 1% bovine serum albumin, and stained with rabbit anti-human collagen type IV (ab6581, Abcam, Cambridge, MA) overnight at 4 °C. The constructs then were rinsed with PBS and incubated with goat anti-rabbit−Alexa Fluor 633 conjugate (A-21070, Life Technologies, Carlsbad, CA) overnight at 4 °C. After rinsing, constructs were counterstained with fluorescein isothiocyanate (FITC)-conjugated Ulex europaeus agglutinin 1 (UEA-1) lectin (L9006, Sigma-Aldrich, St. Louis, MO) and phalloidin (A22283, Molecular Probes, Eugene, OR) to stain the endothelial cell membrane and actin cytoskeleton, respectively.

2.3.8 3D Vessel Morphology Analysis

For 3D qualitative analysis, tissue constructs were imaged using an Olympus FluoView FV-1000 confocal system adapted to an inverted microscope (IX81, Olympus Corporation, Tokyo, Japan). Image stacks were collected from one to three locations within each of the three independent tissue constructs per experimental group. All of the image files were imported into MATLAB (The MathWorks, Natick, MA) to create projections of each stack. Confocal reflection microscopy was used to visualize the collagen-fibril microstructure[88].

For quantitative vessel morphometric analysis, a confocal image stack (635.9×635.9×100 μm^3) was collected from the tissue sphere within each of the three independent tissue constructs per experimental group (n = 3). Image files were imported into Imaris (Bitplane, Concord, MA) for 3D reconstruction and analysis. Briefly, an

isosurface was created and split into individual surface objects that were characterized by a set of geometric parameters including sphericity, ellipticity (prolate or oblate), ellipsoid axis length, and volume. Objects were then classified as a quiescent cell, short vessel, small vessel network (SVN), extensive vessel network (EVN), or other using the decision tree Supplemental Figure 1. Objects with volumes less than 2000 μm^3 were regarded as debris and not considered in the morphological profile analysis. The volumes of objects classified as a short vessel, SVN, and EVN were summed to calculate the total vessel volume, which was used to calculate the vessel volume percentage of the entire imaged volume.

2.3.9 Quantification of Alignment of Collagen Fibrils and Cells.

Confocal reflection and fluorescence image volumes were used to determine the collagen fibril and cell orientations, respectively. Image volumes (1309 μm × 436 μm × 30 μm) were captured in such a way that their length was oriented parallel to the normal line of the sphere. Each image volume was then segmented into thirds lengthwise to determine the orientation as a function of distance from the tissue− tissue interface. The angular direction was calculated using an ImageJ fast Fourier transform algorithm. The absolute values of all orientation angles were then divided by 90 to create a normalized alignment parameter with values of 0 and 1 representing orientations tangent (parallel) and normal (perpendicular) to the sphere surface. Two image volumes within each of three replicate constructs were analyzed

2.3.10 Statistical Analysis

Statistical analyses were performed using statistical analysis software (SAS, Cary, NC). Unless otherwise stated, comparisons were made using one-way analysis of variance (ANOVA) with a Tukey posthoc test. A critical global p value of 0.05 was used.

2.4 Results and Discussion

2.4.1 Biphilic Surfaces Reproducibly Form Collagen and Tissue Spheres

Superhydrophobic surfaces are characterized by a large water droplet contact angle (>150°; see Figure 2.2A) and low contact angle hysteresis (<10°), resulting in spherical droplets that roll off the surface even when it is tilted at a very slight angle. In the present

work, biphilic surfaces consisting of hydrophilic regions patterned onto a superhydrophobic surface supported the highly reproducible formation of variously sized tissue spheres composed of polymerized collagen-fibril matrices in the presence and absence of cells (Figure 2.2B,C). Patterning the superhydrophobic surface with small hydrophilic spots was necessary to facilitate solution deposition and prevent free rolling of spheres. Spots with a diameter of 0.9 mm preserved a high contact angle of greater than 150°, creating highly spherical tissue construct geometries.

A full factorial experimental design was performed to quantify the effects of oligomer matrix stiffness (as specified by the oligomer concentration) and volume (5, 10, or 15 μL) on the tissue sphere geometry and reproducibility. For a given target tissue sphere volume, the measured sphere volume delivered by an air-displacement pipet was inversely related to the collagen-fibril matrix stiffness (oligomer concentration) (Figure 2.3A). The measured tissue sphere volumes for 1000 Pa oligomer, representing the highest-viscosity solution, were roughly 73%, 78%, and 84% of the specific target volumes of 5, 10, and 15 μL, respectively. The use of a positive-displacement pipet dramatically improved the volume delivery accuracy and precision. In fact, when a positive-displacement pipet was used to create 1000 Pa spheres, the accuracy was at least 87% and the precision was 1.9% or better for all volumes tested. Unlike air-displacement pipettes, which use a compressible dead-air volume to move the fluid, positive-displacement pipettes use an incompressible piston to move the fluid. This direct contact enhances the accuracy and precision, especially for viscous liquids. Finally, although gravity effects caused an inverse relationship between the sphere aspect ratio and the measured volume, the sphere aspect ratios were greater than 0.8 for all volumes and matrix stiffness values tested (Figure 2.3B). Taken together, the results demonstrate that the oligomer tissue sphere volume and geometry can be reproduced with high precision and accuracy

A

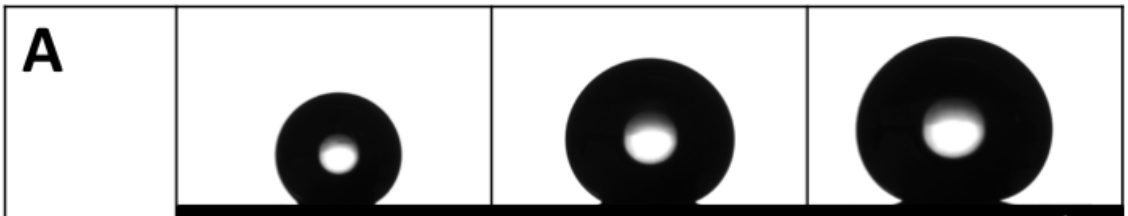

Target Volume		5µL				10µL				15µL			
Collagen Matrix Stiffness (Pa)		0	200	1000	1000	0	200	1000	1000	0	200	1000	1000
Pipet type		Air	Air	Air	Pos	Air	Air	Air	Pos	Air	Air	Air	Pos
Measured Volume (µL)	Mean	4.26	3.84	3.66	4.33	9.40	8.74	7.77	9.14	14.20	12.98	12.59	13.26
	Standard Deviation	0.10	0.14	0.14	0.05	0.04	0.04	0.13	0.07	0.12	0.25	0.04	0.26
Coefficient of Variation		2.4%	3.6%	3.8%	1.1%	0.4%	0.4%	1.7%	0.8%	0.8%	1.9%	0.3%	1.9%

B

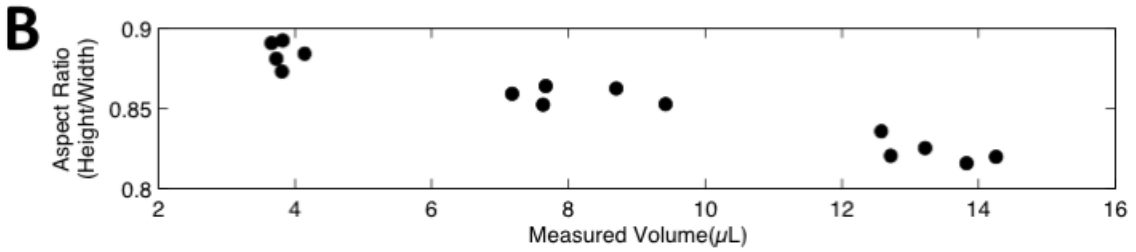

Figure 2.3 The method for producing collagen spheres was reproducible when using the positive displacement pipet. Due to gravity, the collagen spheres became flatter as the volume of the droplet was increased. (A) Representative goniometer images and volumetric measurements for oligomer spheres prepared at target volumes of 5, 10, and 15 µL with matrix stiffnesses of 0 (water), 200, and 1000 Pa (specified by the oligomer concentration). The goniometer images represent oligomer spheres (200 Pa) prepared at designated volumes (scale bar = 1 mm). Target volume indicates the volume specified on the air-displacement (Air) or positive-displacement (Pos) micropipette. (B) Scatter plot of measured oligomer sphere volumes and aspect ratios for all of the matrix stiffness values. Data points represent a combination of 0, 200, and 1000 Pa oligomer spheres.

2.4.2 Multi-tissue Interface Format Prevents Cell-Mediated Tissue Contraction of High-Cell-Density Tissues

A number of researchers, including our group, have shown that conventional monodispersion cultures of ECs or their progenitors within type I collagen or fibrin matrices undergo vasculogenesis[38], [40], [52], [53], [89]. The extent of vessel network formation, as well as their maturation and stability, depends on specific microenvironment conditions, including matrix composition and physical properties[25], [40], [52], [90], [91], medium composition[92], type of EC[52], and addition of accessory cells[77], [91]. The

extent of vessel formation was also shown to be positively correlated with the EC seeding density[93]; however, seeding densities of 1×10^6 cells/mL or lower are routinely used to avoid tissue construct contraction. Tissue contraction depends on the combination of cell density and type[52], matrix type and associated physical properties[94]–[96], and physical boundary conditions[79], [95]. Culture surface coating with glutaraldehyde, polyethylenimine, or poly-L-lysine may be applied to improve construct adherence and minimize contraction[55], [97].

Here we evaluated both the conventional monodispersion format and the proposed multitissue interface culture format on their ability to maintain mechanical boundary conditions and avoid tissue construct contraction (Figure 2.4). In all of the experiments, the oligomer concentration was kept constant at 1.4 mg/mL ($G' = 200$ Pa) since conventional monodispersion culture of ECFCs within this matrix formulation has been shown to induce robust vessel formation[38]. The volumes of the sphere (5 μL; ∼2 mm in height) and surrounding tissue microenvironment (250 μL; ∼2.6 mm in height) were selected such that the tissue sphere was completely embedded within the surrounding tissue microenvironment, ensuring uniform and highly reproducible tissue−tissue interactions and mechanophysical properties across the sphere surface area. As expected, for monodispersion cultures (Figure 2.4, top), the tissue construct contraction increased significantly ($p < 0.05$) with increasing cell density, except for constructs prepared at the lowest ECFC density (0.5×10^6 cells/mL), where contraction was not detected. Tissue constructs prepared with 2×10^6 and 5×10^6 cells/mL displayed density-dependent contraction as early as 24 h, with final tissue volume percentages of 38.5 ± 12.6% and 10.3 ± 12.1%, respectively, after 3 days of culture. In contrast, all of the constructs prepared using the multitissue interface method maintained their starting tissue volumes regardless of ECFC seeding density (Figure 2.4, bottom). Additionally, there was no statistically significant change in the cross-sectional area of the embedded sphere for any of the experimental groups over the 3 day time period (Figure 2.4). Notably, tissue sphere embedment within a surrounding tissue matrix represents a variation of bilayered collagen substrates in which two collagen matrices are polymerized consecutively, one on top of the other[98]. Both approaches result in fusion of two different tissue microenvironments to create a tissue interface. Unlike the conventional monodispersion format, the multitissue

interface approach incorporates a tissue−tissue interface that prevents cell-mediated tissue contraction, representing a more controlled and physiologically relevant microenvironment.

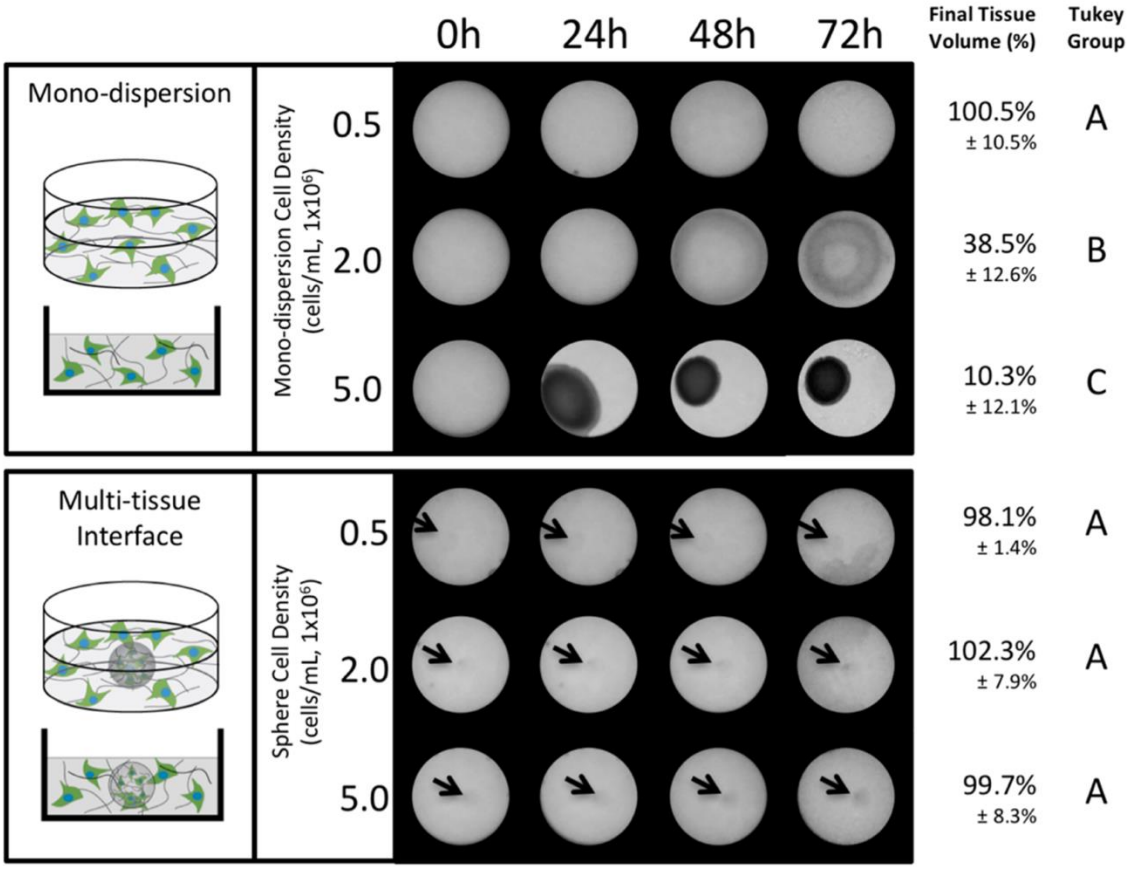

Figure 2.4 Sphere tissues within the multitissue interface model prevented cell-mediated contraction at all time points and densities, while the monodispersion tissue constructs experienced an increase in rate and extent of contraction as cell density was increased. Time-dependent contraction of tissue constructs prepared using (top) the monodispersion format and (bottom) the multitissue interface method. Monodispersion constructs were prepared by seeding 0.5×10^6, 2.0×10^6, or 5.0×10^6 ECFCs/mL within an oligomer matrix (200 Pa). Multitissue interface constructs involved embedding an oligomer sphere (200 Pa, 5 μL; arrows) prepared with 0.5×10^6, 2.0×10^6, or 5.0×10^6 ECFCs/mL within a surrounding tissue consisting of 0.5×10^6 ECFCs/mL within an oligomer matrix (200 Pa). Final tissue volumes were measured after 72 h of culture and compared statistically using Tukey's test. Letters indicate statistically different groups ($p < 0.05$).

As presented here, our *in vitro* multitissue interface model involves a "tissue spheroid" formed with a specified cell population as well as a specified ECM component. Such an approach should be distinguished from the more well established "cell spheroids", which are formed exclusively from cells. Specifically, endothelial cell spheroids, formed

in the absence of any specified matrix component, are routinely embedded within a surrounding collagen matrix, creating an *in vitro* model of angiogenesis[99]. Spheroid formation is induced by culturing endothelial cells overnight within nonadherent cultureware[72], [100]. Compared with the multitissue interface model, cell–cell interactions dominate within endothelial cell spheroids, and vasculogenesis is not observed. Instead, vessels sprout and extend from the spheroid into the surrounding matrix, mimicking angiogenesis[99]

2.4.3 Multi-tissue Interface Cultures Enhance the Rate and Extent of Vessel Morphogenesis and Stabilization

In the present study, we compared the two culture formats and observed differences at the tissue and cellular levels in terms of vessel morphogenesis. Although both formats showed that the extent of vessel formation was positively correlated with ECFC density, dramatic differences in vessel network induction, morphology, and stabilization were observed; this is largely attributed to differences in the mechanical boundary conditions (Figure 2.5). Consistent with our previous reports[38], ECFCs cultured for 3 days at low density (0.5×10^6 cells/mL) in a monodispersion format were round or vacuolated with regional collagen type IV deposition associated with ECFC membranes (Figure 2.5A). As the ECFC density increased, vacuolated cells fused, forming increased numbers of small vessel networks with type IV collagen deposition apparent along the length of the vessel. Constructs containing 5×10^6 ECFCs/mL appeared to have the highest vessel density because of contraction of the tissue volume; however, the ECFCs remained round or formed only short vessels with limited network interconnections (Figure 2.5A). For monodispersion cultures, the cell–matrix tension balance is quickly lost upon tissue contraction, which occurs when collective cell traction forces overcome tissue–plastic adhesive forces. As such, the matrix–integrin–cytoskeleton signaling experienced by the vessel-forming endothelial cells is altered, compromising vessel elongation and anastomosis. Clearly, these results confirm that sufficient cell–matrix traction forces are necessary for induction of vasculogenesis as well as vessel morphogenesis[101]. In addition, the number of vessel-forming networks, which depends on the ECFC density, is an important driver for network connection or anastomosis.

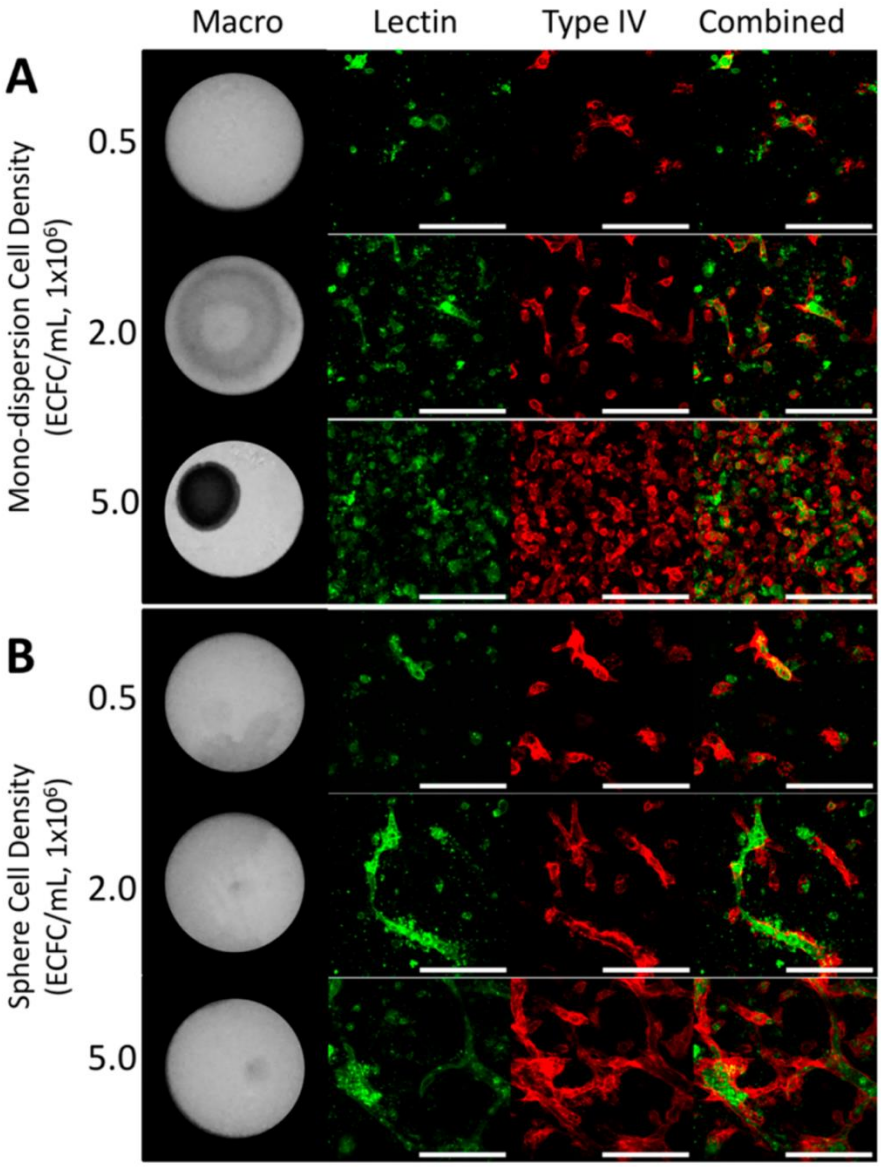

Figure 2.5 Within the uncontracted tissue constructs (multitissue interface model, BOTTOM), ECFC vessel formation increased with increasing ECFC density. On the other hand, the contracted monodispersion tissue constructs contained smaller, compromised vessel formation. Projections of confocal image stacks (50 μm thick) illustrating vessel network formation (green fluorescence, lectin) and type IV collagen deposition (red fluorescence) following 3 days of culture in either (A) the monodispersion format or (B) the multitissue interface format. Confocal images were taken within the tissue sphere of the multitissue interface format. Monodispersion constructs were prepared by seeding ECFCs at specified densities within an oligomer matrix (200 Pa, 250 μL). Multitissue interface constructs were prepared by embedding an oligomer sphere (200 Pa, 5 μL) prepared with ECFCs at a specified density within a surrounding tissue consisting of 0.5×10^6 ECFCs/mL within an oligomer matrix (200 Pa, 250 μL). After 3 days of culture, the 5×10^6 ECFCs/mL sphere demonstrated superior vessel network formation relative to the other groups. Scale bars = 150 μm .

Results observed with the multitissue interface model further support the concept that both the number of vessel-forming networks and cell–matrix traction forces are critical to the overall vessel morphogenesis process. In this format, tissue sphere ECFCs showed rapid, extensive vessel network formation (Figure 2.5B) that increased with ECFC seeding density. In fact, extensive multicellular vessel networks stabilized by type IV collagen were apparent within only 3 days. This accelerated rate of vessel formation is at least 2 times as fast as those in previous reports by our group[38] as well as other culture models involving EC–pericyte cocultures[77]. Thus, our model likely better recapitulates *in vivo* developmental vasculogenesis, which is said to occur in the span of between several hours to a few days[102].

Upon comparison of the monodispersion and multitissue interface formats at the lowest ECFC density (0.5×10^6 ECFCs/mL), the observed vessel numbers and morphologies were similar, largely since ECs in the two formats experience similar cell–matrix tension balance. In contrast, high-density multitissue interface cultures prepared with 2×10^6 or 5×10^6 ECFCs/mL formed vessel networks that were longer and more interconnected than those in the corresponding monodispersion cultures. We postulate that this improved outcome may be attributed to the fact that the multitissue interface model supports maintenance of the tissue geometry and the associated cell–matrix tensional forces. As shown in Figure 2.5B, multitissue interface cultures prepared with 5×10^6 ECFCs/mL formed extensive, highly interconnected, and lumenized vessel networks stabilized by a basement membrane, resembling capillary networks (Supplemental Figure 2) formed *in vivo*. It has been postulated that pericytes or accessory cells are required for stabilization of formed vessels by basement membrane deposition[77]. However, the results obtained in the present study confirm our previous findings that oligomer collagen matrices are sufficient to induce type IV collagen deposition by ECFCs in the absence of accessory cells[38], again emulating steps of vasculogenesis reported in the quail[103].

2.4.4 Customizable Tissue-Tissue Interface: ASC Addition to Surrounding Tissue Dramatically Improves ECFC Vessel Formation and Stabilization within Tissue Sphere

Recently, much attention has been focused on determining how accessory cells, such as pericytes, affect vessel morphogenesis and stabilization for both *in vitro* and *in vivo* tissue engineering strategies[90], [104]–[107].› It is generally accepted that accessory cells enhance vessel morphogenesis through not only paracrine signaling but also direct cell−cell contact[108], [109]. Accessory cells also remodel and reorganize the substrate, which in turn modulates mechanophysical EC−matrix interactions[110]. To study EC−accessory cell interactions, researchers routinely employ cocultures in which ECs and accessory cells (i.e., pericytes, fibroblasts, ASCs, and bone-marrow-derived mesenchymal stromal cells) are concurrently and homogeneously monodispersed in a substrate[77], [91], [110]. In the present study, we employed the multitissue interface model to determine the extent of crosstalk between the two distinct tissue compartments. Specifically, we defined how ECFCs and ASCs, alone or in combination with the surrounding tissue microenvironment, affect ECFC vessel formation within the embedded tissue sphere. For these experiments, all of the tissue constructs were prepared with embedded tissue spheres containing 5×10^6 ECFCs/mL. ASCs were chosen as the accessory cells because of their suitability for autologous cell therapies.

Qualitative evaluation of constructs cultured for 3 days indicated that ASCs, ECFCs, and ASCs + ECFCs in the surrounding tissue enhanced ECFC vessel formation within the tissue sphere relative to the control containing no accessory cells (Figure 2.6A−D). Although the quantified vessel volume percentages for the control (6.4 ± 2.1%) and ECFC-only (6.8 ± 3.5%) groups were statistically similar ($p > 0.05$), the ECFC-only group contained fewer quiescent cells and vessels that appeared slightly more elongated. This increase in the percentages of short vessels and small vessel networks and decrease in the percentage of quiescent cells were captured by the new algorithm designed to quantify identified categories of vessel morphology (Figure 2.6A, B). This quantification strategy provided a vessel morphogenesis “fingerprint” for each experimental group studied.

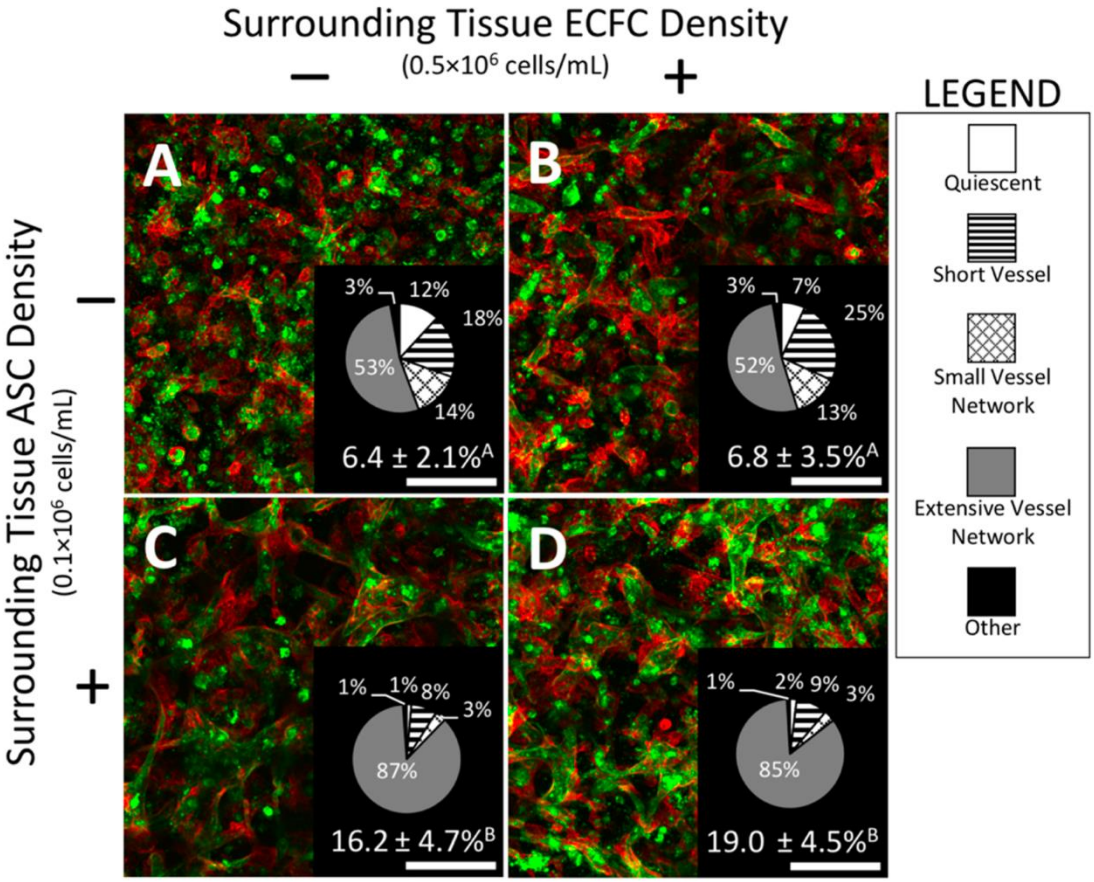

Figure 2.6 The presence of ASC in the surrounding tissue provided a significant boost to ECFC vessel volume percentage within the sphere tissue compartment. Projections of confocal image stacks (200 μm thick) taken within the tissue sphere, illustrating vessel network formation and basement membrane deposition for various multitissue interface constructs after 3 days of culture. ECFC-encapsulated oligomer spheres (200 Pa, 5×10^6 ECFCs/mL, 5 μL) were embedded in oligomer matrices (200 Pa, 250 μL) seeded with either (A) no accessory cells, (B) ECFCs only, (C) ASCs only, or (D) a combination of ECFCs and ASCs. Tissue constructs were stained with UEA1 lectin (green fluorescence) and type IV collagen (red fluorescence) for visualization of ECFC vessel networks and deposited basement membrane, respectively. The inset at the bottom right in each panel contains quantified vessel morphology parameters and vessel volume percentages. The vessel volume percentage increased significantly with the presence of ASCs in the surrounding tissue, as determined using Tukey's test. Superscript letters indicate statistically different groups ($p < 0.05$). Scale bars = 150 μm.

A dramatic difference was observed in both the volume percentage and morphology of vessels formed when ASCs were added to the surrounding tissue. Both the ASC and ASC + ECFC groups induced the formation of highly interconnected and persistent vessel networks (Figure 2.6C, D). The vessel volume percentages for the ASC and ASC + ECFC

groups were 16.2 ± 4.7% and 19.0 ± 4.5%, respectively, which were more than 2-fold greater than those without ASCs. In terms of vessel morphology, the ASC and ASC + ECFC groups were composed of 87% and 85% extensive vessel networks (EVN), respectively, compared with roughly 50% EVN for groups without ASCs. Unlike conventional monodispersion cultures, where ECs and accessory cells are cocultured together within a substrate, the multitissue interface model allows ECs and accessory cells to be cocultured in separate but interfacing tissue environments. This approach effectively minimizes the influence of initial direct cell–cell contact but allows diffusion of paracrine signals. While an ASC-conditioned medium has been shown in past studies to positively affect EC outgrowth and vessel formation, it did not induce angiogenic vessel sprouting[106], [111]. Similar observations were made in our multitissue interface model, where vascularization was confined within the tissue sphere. Collectively, such findings further suggest that ASC–ECFC crosstalk positively influences vasculogenesis through ASC-mediated paracrine signaling as well as transmission of matrix mechanophysical signals.

2.4.5 Increasing the ASC Density Within the Surrounding Tissue of the Multitissue Interface Construct Further Enhances Vascularization within the Tissue Sphere and Across the Tissue–Tissue Boundary

Because enhanced vasculogenesis was observed at a low density of ASCs (0.1×10^6 cells/mL) in the surrounding tissue, we hypothesized that increased ASC density would lead to increased vessel volume percentage within the tissue sphere and also facilitate vessel elongation (angiogenesis) across the tissue interface. Once again, all of the tissue spheres were prepared with 5×10^6 ECFCs/mL at a volume of 5 μL within 200 Pa oligomer collagen. After 3 days of culture, enhanced vasculogenesis within the tissue sphere was evident both qualitatively and quantitatively, with an increase in the vessel volume percentage with increasing ASC density (Figure 2.7A, B). The increase in vessel volume percentage was further correlated to the EVN percentage, with EVN percentages of 80%, 90%, and 94% for groups containing 0.1×10^6, 0.2×10^6, and 0.5×10^6 ASCs/ mL, respectively. Therefore, the extent of vascularization within the tissue sphere was positively correlated with the ASC density in the surrounding tissue. Furthermore, ASCs assumed a pericyte-like role, migrating toward the abluminal wall of the vessels

(Supplemental Figure 3) which is consistent with previous findings in 3D models using fibrin[109].

Another interesting finding was the modulation of vascularization events at the tissue−tissue boundary as a function of ASC density. As shown in Figure 2.7C, when the surrounding tissues were seeded with lower ASC densities (0.1×10^6 and 0.2×10^6 ASCs/mL), vascularization events were confined primarily to the tissue spheres. However, constructs containing 0.5×10^6 ASCs/mL showed enhanced vasculogenesis within the sphere as well as vessel elongation or angiogenesis across the tissue interface (Figure 2.7C). Furthermore, the amount and extent of ASC orientation toward the sphere increased with ASC seeding density (Figure 2.8). It is well-established that ECFC-secreted platelet-derived growth factor BB (PDGF-BB) is a potent chemoattractant for not only pericytes but also ASCs[112]–[114], making paracrine signaling likely to have contributed to ASC alignment. Another possible contributing factor is mechanotransductive cues. Previous research involving the *in vitro* EC spheroid model showed that cell traction forces of the EC spheroid radially align collagen fibrils, creating collagen "paths" extending outward from the EC spheroid[100]. Additionally, EC spheroids showed preferential angiogenic sprouting toward one another even when located 600−800 μm apart. Interestingly their observed long-distance angiogenic sprouting was preceded by matrix reorganization. In our model, we observed increased collagen-fibril alignment or "paths" with increasing ASC density in the surrounding tissue for distances exceeding 1000 μm (Figure 2.8). The distance of ECM alignment was positively correlated with the ASC density in the surrounding tissue. Our current observations combined with those reported in the literature provide evidence that ECFC−ASC crosstalk across tissue boundaries, including cell−matrix mechanophysical forces as well as paracrine signaling, are important vascularization determinants, contributing to both early-stage vasculogenesis and later-stage angiogenesis and vessel elongation.

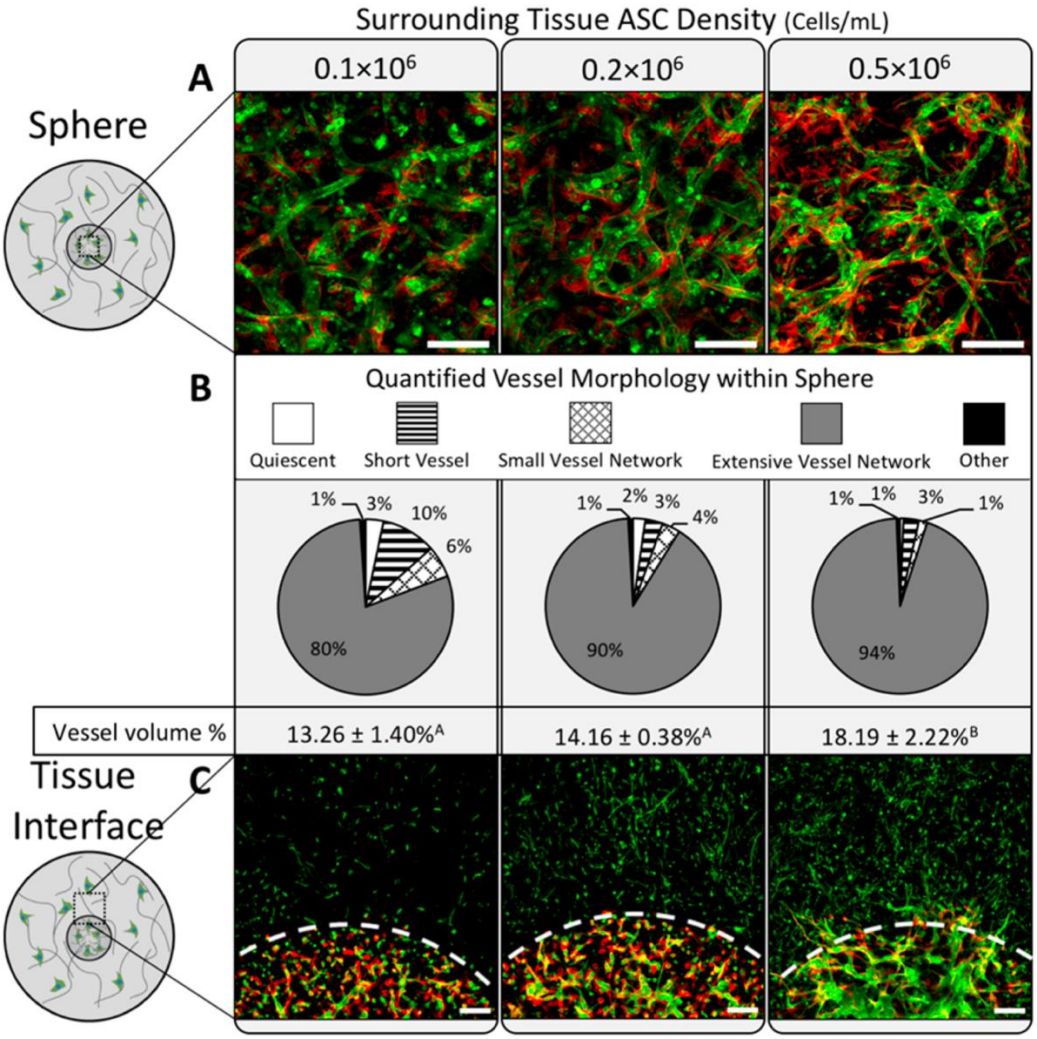

Figure 2.7 Increasing ASC density in the surrounding tissue compartment resulted in (TOP) an increase in ECFC vessel volume percentage within the sphere tissue compartment and (BOTTOM) ECFC angiogenic sprouting across tissue compartments. (A) Projections of confocal image stacks (200 μm thick) illustrating vessel network formation and basement membrane deposition within the tissue sphere for various multitissue interface constructs after 3 days of culture. ECFC-encapsulated oligomer spheres (200 Pa, 5×10^6 ECFCs/ mL, 5 μL) were embedded in oligomer matrices (200 Pa, 250 μL) seeded with ASCs at either 0.1×10^6, 0.2×10^6, or 0.5×10^6 cells/mL. Tissue constructs were stained with UEA1 lectin (green fluorescence) and anti-type IV collagen (red fluorescence) for visualization of ECFC vessel networks and deposited basement membrane, respectively. Scale bars = 150 μm. (B) Quantified vessel morphology parameters show that the vessel volume percentage as well as the percentage of extensive vessel networks were positively correlated with the ASC density. Tukey's test was used to compare groups. Superscript letters indicate statistically different groups ($p < 0.05$). (C) Projection of confocal image stacks (50 μm thick) illustrating vessel network formation at and across the tissue−tissue interface (dotted line). Tissue constructs were stained with phalloidin (green fluorescence) and anti-type IV collagen (red fluorescence) for visualization of cells and deposited basement membrane, respectively. Scale bars = 150 μm.

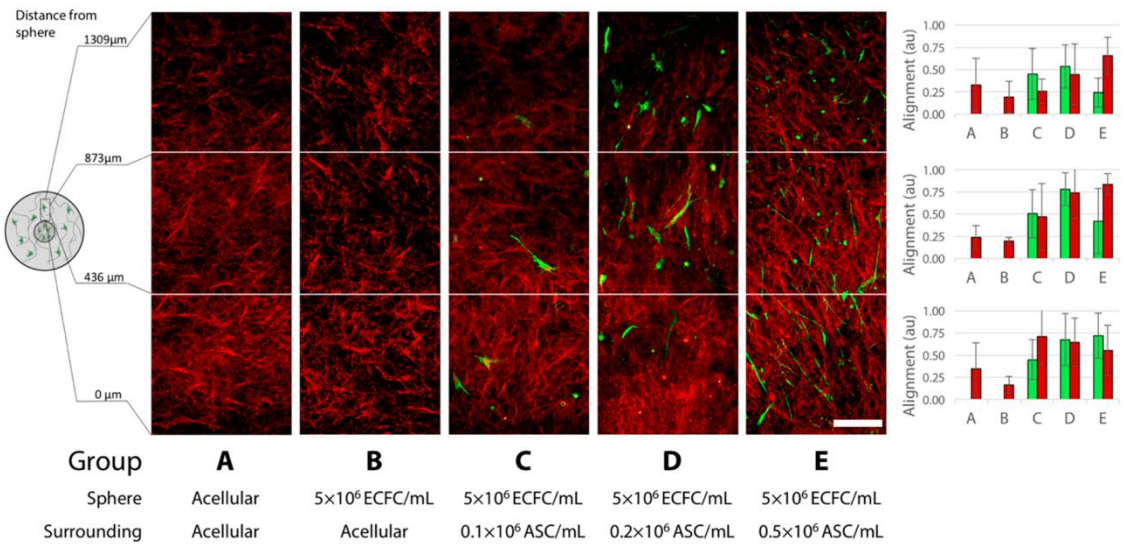

Figure 2.8 Increasing the ASC density in the surrounding tissue compartment increased the cell-matrix tensional forces, resulting in matrix and cellular alignment towards the sphere tissue compartment. (LEFT) Schematic showing imaging areas with specified distances from the sphere. (CENTER) Projections of confocal image stacks (30 µm thick) outside the tissue sphere for various multitissue interface constructs after 3 days of culture. ECFC-encapsulated oligomer spheres (200 Pa, acellular or 5 ×10^6 ECFCs/mL, 5 µL) were embedded in oligomer matrices (200 Pa, 250 µL) seeded with ASCs at either 0.0×10^6, 0.1×10^6, 0.2×10^6, or 0.5×10^6 cells/mL. Tissue constructs were stained with phalloidin (green fluorescence) for visualization of ASC orientation, and confocal reflectance was used to visualize the collagen-fibril microstructure (red fluorescence). Increasing the ASC density in the surrounding tissue increases the collective cell-mediated traction force, leading to tension-induced alignment of collagen fibrils. Parallel alignment of collagen fibrils appears to be positively correlated with the ASC seeding density. Constructs with 0.5×10^6 ASCs/mL yielded higher alignment at distances farther away from the sphere compared with the other groups. Scale bar = 150 µm. (right) Bar graphs displaying the alignment of the collagen fibrils (red) and ASCs (green) for each respective group.

2.5 Conclusion

Vasculogenesis and angiogenesis are dynamic and integrated neovascularization processes that require complex spatiotemporal cell–cell, cell–matrix, and soluble factor signaling. Herein we have described a novel *in vitro* multitissue interface model that is ideally suited for diverse vascularization studies, including vascularization across tissue–tissue interfaces, because it recapitulates a number of elements associated with *in vivo* developmental vasculogenesis. Conventional *in vitro* models focus on vasculogenesis (*de novo* formation of blood vessels) or angiogenesis (sprouting of vessels from existing

vessels or EC monolayers). However, the multitissue interface model captures both initial *de novo* vasculogenesis within the tissue sphere and later-stage angiogenesis marked by vessel sprouting and elongation into the surrounding tissue compartment. Creating a model with defined and highly reproducible tissue−tissue interfaces involved the application of surfaces with uniquely engineered surface wettability patterns that could capture and support various-sized tissue spheres. Reproducible model development was further facilitated by the use of collagen oligomers, which polymerize rapidly (roughly 10 min) and can be formulated to create a broad range of interstitial type I collagen fibril microenvironments (beyond 2000 Pa)[39]. Conventional collagen monomer matrices, even when used at high concentrations, yield compliant matrices with stiffness values of roughly 200 Pa or less[39]. However, the model shown herein allows control over each tissue microenvironment in terms of matrix composition and physical properties, cell type, and cell density. Importantly, the boundary conditions for the multitissue construct allowed the generation of a component tissue compartment with unprecedented cell densities while avoiding the cell-mediated tissue contraction routinely observed in high-cell-density tissues formed via conventional monodispersion methods. The rapid vasculogenesis observed in the tissue sphere was supported by a combination of high cell density and sufficient ECFC−matrix mechanophysical interactions. The stable boundary conditions and microstructure mechanical properties of the collagen-fibril matrix enabled ECFCs to quickly generate the necessary matrix traction force to guide the formation, maturation, and stabilization of vessel networks. Furthermore, the well-documented benefits provided by ASC paracrine signaling were undeniably present in our system; however, it was evident that cell−matrix tensional forces transmitted between tissue compartments also played a role in later-stage angiogenic vessel elongation. While the present work demonstrates the utility of this model for mechanistic studies of tissue and tissue−interface vascularization, the model has broader applications, including bone−soft tissue interactions, tumor−stroma interactions, blood−brain barrier, hematopoietic stem cell niche, and islet−vascular interactions. This novel *in vitro* model is expected to provide guiding principles for the design of complex multitissue systems, including vascularized tissue-engineered constructs for tissue engineering and regenerative medicine applications.

CHAPTER 3. APPLYING A MULTIPLEX PEPTIDE BIOSENSOR TO LIVE-TRACK KINASE PHOSPHORYLATION WITHIN ENDOTHELIAL CELLS CULTURED IN THREE-DIMENSIONS

3.1 Overview

Chapter 3 details an interlaboratory collaboration between the Harbin and the Iyudayaraj lab. In chapter 2, we used the multitissue interface model to determine the critical design parameters for rapid vascularization in less-dense tissue constructs. Here, we found that ECFC density, cell-matrix tensional forces, and the presence of ASC was important for rapid vascularization. However, the cellular mechanism underlying the rapid vessel formation was not investigated. To understand this "black box," we employed peptide biosensors developed by Dr. Nuri Damayanti to track the signaling within live ECFCs cultured in the multitissue model I developed. Live imaging of cell signaling is advantageous over terminal end-point data collection (i.e., western blot, mass spectrometry), because it allows the study of transient cells signaling dynamics in response to a stimulus. When developing a biosensor, it is essential that the testing platform is robust. Since vessel formation is difficult to achieve and maintain *in vitro*, it was important to use the multitissue model to achieve rapid, robust vessel formation. Using the peptide biosensors, we further defined the critical design parameters determined in Chapter 2. Specifically, we probed the Vascular Endothelial Growth Factor Recepter-2 (VEGFR-2) and AKT signaling pathways, both of which are essential for neovascularization. We demonstrated that the two sensors could be taken up by a variety of cell types. Furthermore, we employed the sensors within various endothelial cell models: i.) 2D-cultured ECFCs, ii.) 3D-cultured ECFCs (multitissue model), and iii.) vascularization within zebrafish. All three models demonstrated transient sensitivity to the presented stimuli. Overall, the significant finding of this work was that we could live-track ECFC signaling within the rapidly formed vessels, which allowed us to further define the critical design parameters of the multitissue model. Future work employing these two technologies may provide insight on optimizing the timing for grafting based on EC signaling dynamics. This work resulted in a published manuscript in the *American Chemical Society: Sensors*.

3.2 Introduction

While achieving vascularization in a robust and rapid manner is important, it is useful to define the underlying cellular signaling pathways. Within the multitissue interface, we include two tissue groups: a small tissue sphere containing a high cell density of ECFCs, and a surrounding tissue to anchor that tissue in place. It is clear that this multitissue model involves increased cell-cell interactions from previously reported models. Additionally, since the tissue sphere is anchored in place, the matrix is kept intact, and thus cell-matrix interactions remain a prominent signaling modality in this system. While conjectures can be made on the contributions of each signaling modality towards vessel formation, specific cellular mechanisms underlying the vessel formation in this model are not yet fully understood.

The dynamic process of vessel formation involves cell proliferation, migration, differentiation, and apoptosis, which are all in response to the complex cellular signaling response. Generally, a cell's response involves movement of the signal from a receptor down a signaling cascade. One aspect of cell signaling, specifically kinase phosphorylation, plays a key role in intracellular signaling. When phosphorylated, the substrate undergoes conformational changes, altered localization, or interacts with an adaptor protein to bring about changes in its activity[115], [116]. Overall, this phosphorylation event triggers a downstream phosphorylation cascade that controls the cellular response[117]. In fact, multiple kinases take part in regulating downstream signaling, which results in complex regulation at the post-translational level. Furthermore, the spatial localization of the kinases, along with its activity, further exemplifies the complexities of kinase signaling.

Regarding endothelial cell signaling, vascular endothelial growth factor receptor-2 (VEGFR-2) is a major receptor responsible for cell growth, survival, and vessel formation. Moreover, the VEGF-A/VEGFR-2 is known as the most prominent ligand-receptor complex within the VEGF system[118]. When VEGF binds to VEGFR2, this results in autophosphorylation of a tyrosine residue in the intracellular domain of VEGFR2, specifically Tyr801. Once this domain is phosphorylated, it upregulates the phosphorylation of Tyr1054 and Tyr1059, further increasing its own activity[119]. Downstream from VEGFR2 are a myriad of signaling proteins: protein kinase c, AKT, p38MAPK, RAC, RHO GTPases, ERK, and MTOR to name a few. VEGFR2 has been

found to be most extensively expressed on endothelial cells, with the highest expressions happening during embryonic vasculogenesis and angiogenesis[120]–[122]. To further highlight its importance in the developing embryo, the knockout of VEGFR2 in mice has demonstrated embryonic lethality[123]. While there are many different downstream signaling molecules to VEGFR2, one of particular importance is AKT.

AKT has been identified as the downstream signaling molecule responsible for endothelial cell survival[124]. As mentioned earlier, when VEGFR-2 is activated, it begins a phosphorylation cascade that activates other signaling molecules. One of these molecules is the phosphatidylinositol 3-kinase (PI3-K), which then phosphorylates lipids on the plasma membrane, which activates a secondary messenger (PIP3). PIP3 recruits AKT to the cell membrane, where AKT is activated. It is clear that these signaling cascades are dynamic, involving the movement of proteins to different parts of the cell in order for activation to occur.

The ability to monitor kinase activity and location would provide tremendous insight on how a specific stimulus affects the complex, intracellular signaling cascade. However, this ability remains difficult to achieve. Current approaches for measuring protein phosphorylation involve western blot[125], mass spectrometry[126], and radioactive labeling[127]. While these methods have proved useful over the years, these approaches require a large number of cells and are only able to capture the average response of a cell population. What is needed is the ability to monitor these phosphorylation events in living cells on a single-cell level, as it could provide useful information on cell response to a specific stimulus.

Other groups have implemented peptide biosensors or genetically engineered probes and have been able to measure protein kinase activity on a single-cell level[128]–[131]. However, these methods employ cell lysates and use either fluorescence intensity-based measurements or Förster resonance energy transfer (FRET), both of which provide challenges for multiplex evaluation. In contrast to these methods, fluorescence lifetime imaging (FLIM) is advantageous, because FLIM is less dependent on excitation power. Another added benefit is that FLIM analysis is not dependent on probe concentration allowing more flexibility in terms of experimental setup and analysis.

In this work, we implemented multiple peptide biosensors within living cells to track kinase phosphorylation using time-correlated single photon counting FLIM (TCSPC-FLIM)[132]–[134]. The peptide biosensors were developed by the Iyudayaraj lab, while the robust vessel formation platform was developed by the Harbin lab. TCSPC-FLIM enables detection of a specific fluorescent species based on its fluorescence lifetime. This capability makes TCSPC-FLIM an ideal choice for monitoring multiple kinases simultaneously. In the present work, we targeted signaling molecules that play a significant role in blood vessel formation, specifically vascular endothelial growth factor receptor-2 (VEGFR-2) and a downstream signaling molecule, AKT[135], [136]. Previous works employed pharmacological inhibition[137], RNA interference[138], [139], and immunoblotting[140], and have shown that differential signaling between VEGFR-2 and AKT result in different cell responses. As such, developing an approach to monitor kinase signaling between these two targets would be useful for researchers in areas of drug development, oncology, synthetic biology, biomaterials, and toxicology.

While the molecule probe used for data acquisition is important, we must also consider an ideal model to use for vessel formation. To vascularize tissue constructs, endothelial cells (EC) are combined with an extracellular matrix (ECM) and growth factors. In these models, the ECs attach to the extracellular matrix (ECM) and begin to sense and respond to a range of stimuli: the ECM, other ECs, and growth factors. While there exists a large number of approaches that have enabled robust vessel formation and have allowed thorough study of vasculogenic vessel formation events, these approaches oftentimes apply excessive growth factors or apoptotic agents and are therefore not physiologically relevant. What is needed is a robust method for *in vitro* tissue vascularization that maintains physiological relevance. As such, we have decided to implement a novel multitissue interface culture model[141]. This model incorporates an EC dense collagen sphere tissue into a surrounding oligomer collagen tissue construct. The format of this tissue culture model allows the culture of a high density of ECs in an uncompromised format. Using this model, extensive tissue vascularization (>15 vessel volume percentage) has been achieved in just 3 days, in lieu of excessive growth factors or anti-apoptotic agents. The model achieves extensive vascularization whilst employing minimal additives, making it an ideal candidate model for drug or biosensor testing. By merging these two platforms, we

developed a method to study multiple signaling pathways simultaneously, capturing both spatial and temporal information, within a physiologically relevant system.

3.3 Materials and Methods

3.3.1 Peptide Biosensor

The design of peptide sensors was based on a well-defined preferential substrate motif for each kinase. A delivery sequence is included in the main kinase-recognition sequence of each sensor. VEGFR-2 sensor, VSOR, contains a VEGFR-2 kinase domain with phosphorylatable tyrosine site. The complete sequence for VSOR is GRRRAAPEDLYK(5-FAM)DFLTGRKKRRQRRRQ). The AKT sensor, ASOR, contains the phosphorylatable serine site. The amino acids sequence for ASOR is ARKRERAYSFK(5-FAM)HHARKKRRQRRRPQ. The excitation/emission for 5-FAM is 492/518 nm. To facilitate multiplex detection, Cy5 fluorophore with excitation/emission at 649/670 nm was used in ASOR. The sequence for nonphosphorylatable ASOR is ARKRERAYCFK(5-FAM)HHARKKRRQRRRPQ, and phosphorylated ASOR is ARKRERAY(Serine-phospho)FK(5-FAM)HHARKKRRQRRRPQ. All peptides were prepared by Alpha Diagnostic at 90% purity.

3.3.2 *In vitro* 2D Cell Culture and *In Vitro* 3D Vasculogenesis Model

Human endothelial colony forming cells (ECFC) were obtained as a kind gift from Dr. Mervin Yoder (Indiana University School of Medicine, Indianapolis, IN) and cultured as previously described[142]. The 3D vasculogenesis model was built in a multitissue interface format as previously described with slight modifications[141]. Specifically, the models were created within glass-bottom petri dishes rather than 48 well plates.

3.3.3 Sensor Delivery and Imaging in 2D and 3D Cultures

Live cells in 2D and 3D cultures were incubated with the respective biosensors in serum free medium for 20 min prior to FLIM imaging experiments. Cells were washed and maintained in the culture medium and live cell imaging chamber with controlled temperature at 37 °C.

3.3.4 TCSPC-FLIM

FLIM experiments utilized a scanning confocal time-resolved microscope system (MicroTime 200, PicoQuant, Germany)[132], [133], [143]–[146] that allows for precise recording of the arrival time at the detector. The instrument response function (IRF)[143] was taken into consideration during measurement and data analysis.

3.4 Results and Discussion

3.4.1 ASOR and VSOR Could be Internalized by Various Cell Types

Both ASOR and VSOR demonstrated the ability to work in a variety of different cell lines (Figure 3.1). Both biosensors were applied to ECFC, MCF12A, RCC 786-R, and HEK-293. In the ECFC, ASOR was found to be localized primarily in the nucleus and appeared to diffuse outwards into the cytoplasm. The VSOR, on the other hand appeared to be explicitly found at the nucleus as well as very lightly at the periphery of the cell. It is important to consider that these ECFC were cultured on a glass coverslip, a 2D condition where ECFC are unable to form vessels. Furthermore, the ability for the sensor to be internalized by a myriad of cells highlights the wide-range applicability of the biosensor.

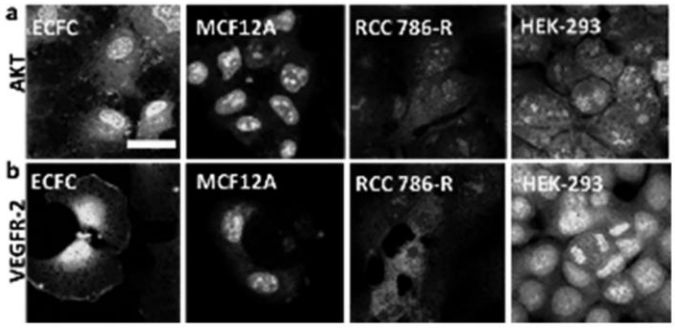

Figure 3.1 (A) ASOR and (B) VSOR were internalized by different cell lines, demonstrating the versatility of the biosensor across cell types. Fluorescence images after 20 min of incubation with ASOR-Cy5 (A) and VSOR-5-FAM (B) (20 μM each) in different cell types cultured on 2D glass coverslips at 37°C. Scale bar = 20 μm.

3.4.2 2D ECFC Signaling Dynamics of VEGFR2 and AKT can be Tracked Using VSOR and ASOR, Respectively

ECFC cultured on glass coverslips were treated with VEGF, an agonist for the VEGFR-2, and the subsequent kinase activity was tracked using the peptide biosensors (Figure 3.2). VEGFR-2−AKT signaling cascade was observed during real-time multiplex monitoring of VSOR and ASOR (Figure 3.2A−D). Within 20 min of VEGF stimulation, VSOR exhibited an increase in fluorescence lifetime in all three major cellular compartments; cell receptor (membrane area) (25% increase compared to t = 0), cytoplasm (30% increase from t = 0), and nucleus (35% increase compared to t = 0) (Figure 3A, B). Subsequently, ASOR also exhibited an increase in fluorescence lifetime indicating an increase in AKT activity at the receptor, cytoplasm, and nucleus (Figure 3.2A, C). Increase in the lifetime signal of both VSOR and ASOR following VEGF stimulation (Figure 3.2 A, C) demonstrates the signaling cascade between VEGFR-2 and its downstream AKT. We also show that the stimulated signals can be inhibited, and the rate of inhibition can be observed (Figure 3.2B, D). After 60 min of VEGF stimulation, Axitinib, a potent VEGFR-2 small molecule inhibitor, was introduced and the signals from both sensors were continuously monitored for another 60 min (Figure 3.2C, D). Both VSOR and ASOR signals initially demonstrated a 10% decrease during the first 10 min following Axitinib administration. However, ASOR signal increased after 20 min while VSOR signal was 45% lower than the initial state (t = 0, Figure 3.2C, D). This result is expected, given the fact that AKT is a common signaling protein shared by distinct signaling pathways[147], [148] and can be activated by many extracellular signals[149], [150]. Therefore, inhibition of VEGFR-2 alone is not sufficient to inhibit AKT activation.

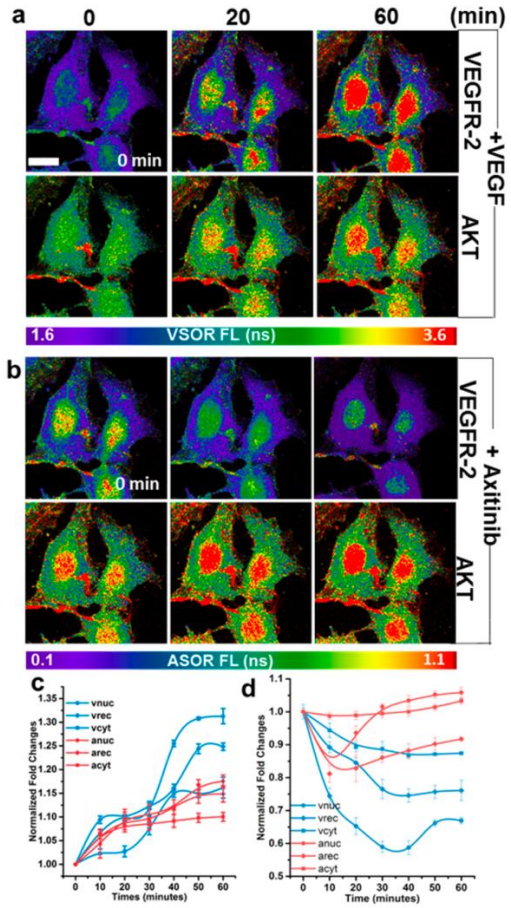

Figure 3.2 ECFC cultured in 2D demonstrated an appropriate response to VEGFR-2 (A) stimulation and (B) inhibition. (C) VEGFR-2 signaling increased with downstream activation of AKT. Similarly, (D) VEGFR-2 signaling decreased in response to an inhibitor with additional downstream effects on the AKT pathway. Real-time multiplex monitoring of VEGFR-2 and AKT phosphorylation in 2D culture. (A) FLIM images and (C) quantitative analysis of VSOR and ASOR upon 20 ng/mL of VEGF stimulation. (B) FLIM images and quantitative analysis (D) of VSOR and ASOR treated for 60 min with 10 nM of the inhibitor, Axitinib in ECFC. Quantitative analysis was conducted on three cellular compartments: cell nucleus (nuc), receptor (rec), and cytoplasm (cyt) compared to control (TOP). Scale bar = 20 μm. n=3 biological replicates.

To further test our multiplex sensors, we stimulated ECFC with insulin, an agonist for insulin receptor signaling pathway, in a VEGF-free medium and monitored the ASOR and VSOR signal for 60 min (Figure 3.3A, B). As expected, ASOR signal increased by 35% within 20 min of insulin stimulation (Figure 3.3A, B). On the other hand, VSOR signal also showed a 10% increase from the initial state, as expected from AKT feedback[151]. we inhibited AKT alone with a potent AKT small molecule inhibitor, Honokiol. We

monitored both VSOR and ASOR signals for 60 min (Figure 3.4A, B). ASOR signal continuously decreased up to 10% during 60 min while VSOR signal remained relatively constant ($P > 0.05$). Further testing of the sensors was demonstrated using insulin stimulation since insulin and VEGFR-2 signaling pathways share AKT as a common downstream kinase in their otherwise distinct signaling cascades[151], [152]. These results demonstrate the ability of our multiplex sensing methodology to monitor the direct activity of multiple kinases in real time.

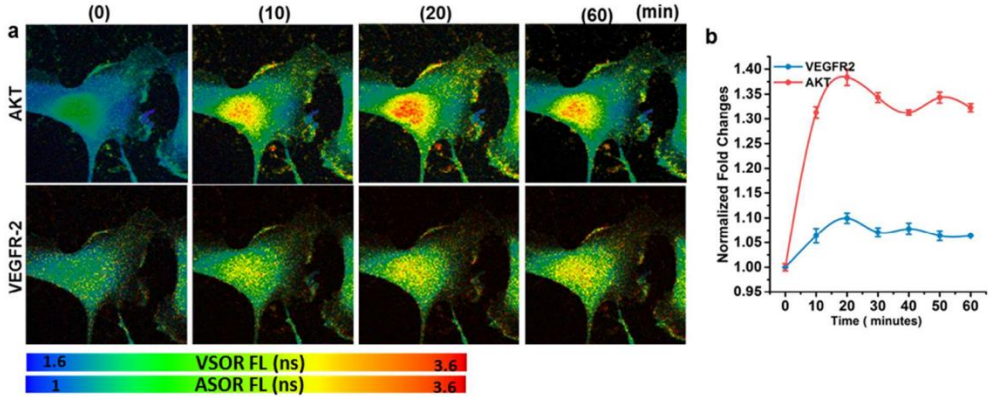

Figure 3.3 ECFC cultured in 2D demonstrated appropriate cell signaling response to insulin, an AKT promotor. AKT signaling increased, which resulted in an increase in VEGFR-2 signaling. Real-time monitoring of ASOR and VSOR after 1-hour of AKT stimulation with 100 ng/mL insulin. (A) Fluorescence lifetime of VSOR (TOP) and ASOR (BOTTOM) shows an initial increase during the first 20 minutes, followed by an oscillatory behavior for the remaining time period. (B) Results drawn from the qualitative images were validated by quantifying the relative change in fluorescence lifetime in both the sensors. In the first 20 minutes, fluorescence lifetime of both sensors increased, however the increase in ASOR (red line) was greater than VSOR (blue line). After 20 minutes, both sensors exhibited a decreasing oscillatory response. Data is representative of three independent biological and three technical replicates. Scale bar = 50 µm.

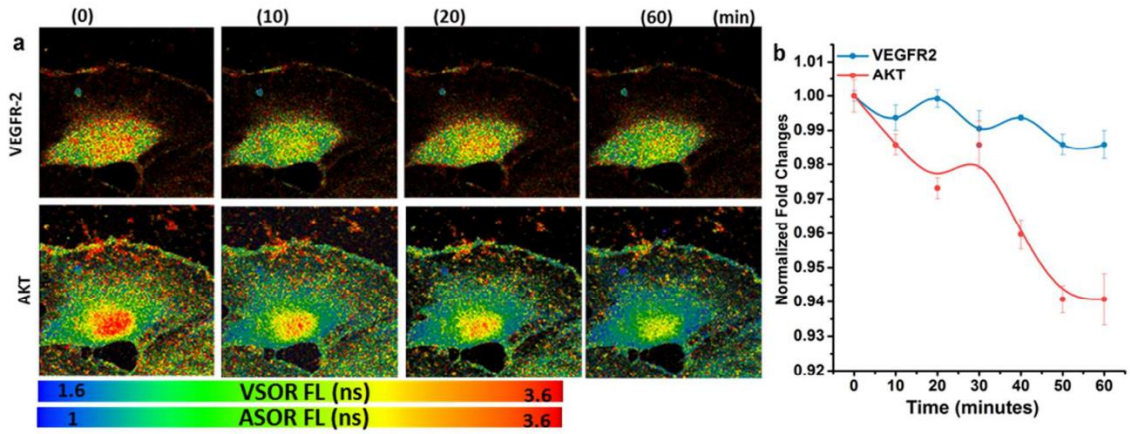

Figure 3.4 ECFC cultured in 2D demonstrated appropriate cell signaling response to honokiol, an AKT inhibitor. AKT signaling decreased, which decreased upstream VEGFR-2 signaling. Real-time monitoring of ASOR and VSOR after 1-hour of AKT inhibition (treatment with 100 μm Honokiol). (A) Time-course FLIM images of VSOR (top) and ASOR (bottom) showed an overall trend of decreasing fluorescence lifetime for both sensors, although a noticeable increase in VSOR fluorescence lifetime was noted after 20 minutes. (B) Quantitative analysis showed a larger decrease in the fluorescence lifetime of ASOR after Honokiol treatment, which was followed by a relatively smaller decrease in the fluorescence lifetime of VSOR. VSOR showed oscillating response starting from 20 minutes with a general decreasing trend. Data was representative of three independent biological and three technical replicates. Scale bar = 50 μm.

3.4.3 3D ECFC Signaling Dynamics of VEGFR2 and AKT can be Tracked Using VSOR and ASOR, Respectively

After validating the VSOR and ASOR sensors to monitor the VEGFR-2−AKT signaling cascade in 2D cultures of ECFC, we extended our study to 3D cultures of ECFC. In our tissue-like 3D vasculogenesis model, ECFCs form a vascular 3D network structure after 72h (Figure 3.5) of culturing[141]. We validated that both of the sensors could be internalized in these 3D-cultured ECFCs (Figure 3.6). After 30 min of incubation, both sensors were internalized inside the 3D vasculature structure. The strategy used in 2D cultures to monitor VEGFR-2 and AKT signaling cascade by VEGF stimulation was utilized in 3D culture.

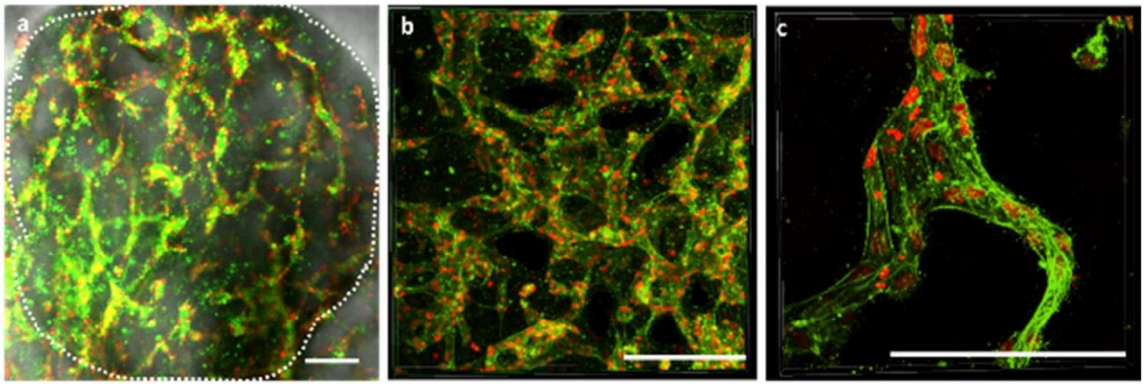

Figure 3.5 Confocal images validated the presence of an intact, interconnected ECFC vessel network. (a) Micro vessel network formed in 3D vasculogenesis model after 3 days of culture. Phalloidin (green) and Hoechst (red) stained for visualization of F-actin and nucleus, respectively with (A) 10x objective, (B) 20x and (C) 60x objective. Scale bar = 100 μm

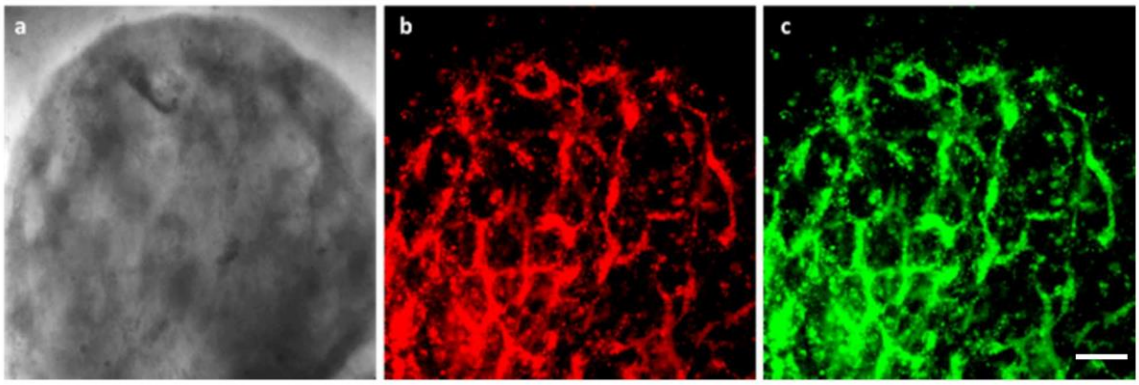

Figure 3.6 ECFC-formed vessels successfully internalized ASOR and VSOR after 30 minutes of incubation with 15 μM of each sensor. 10× magnification images of 3D vasculogenesis model from (A) the bright field mode, (B) the ASOR fluorescence channel and (C) the VSOR fluorescence channel. Scale bar = 100 μm.

Consistent with our results from 2D cultures, upon VEGF stimulation, the fluorescence lifetime of both VSOR and ASOR signals increased (Figure 3.7A, B). Different regions of the vasculature structure exhibited distinct amplitude of signal response upon VEGF stimulation (Figure 3.7A). As in our 2D culture, we also observed a decrease in the fluorescence lifetime of VSOR and ASOR upon treatment with VEGFR-2 inhibitor Axitinib (Figure 3.7C, D), as expected.

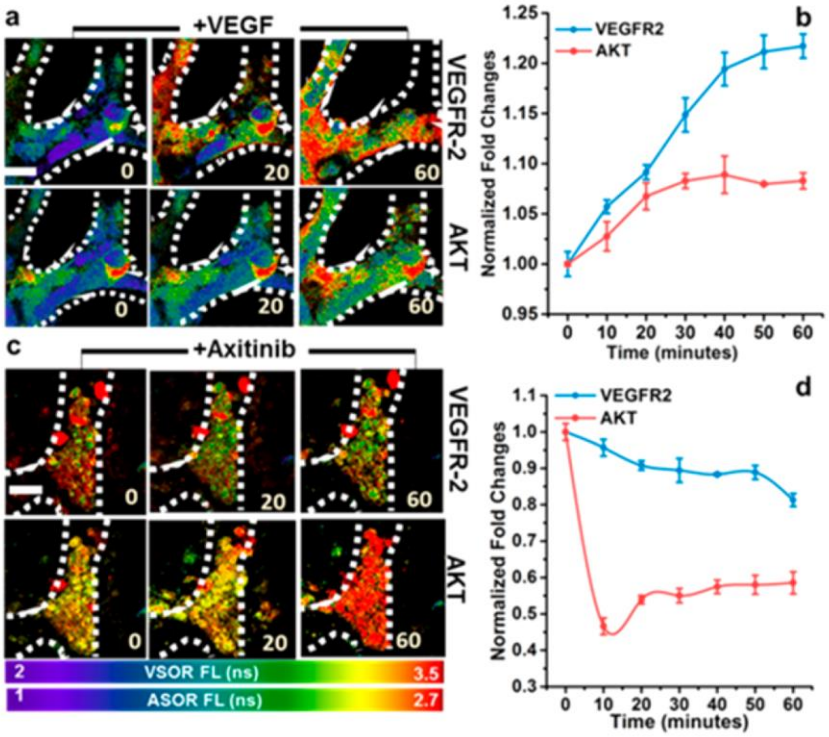

Figure 3.7 ECFC cultured in 3D demonstrated an appropriate response to VEGFR-2 (A) stimulation and (C) inhibition. (B) VEGFR-2 signaling increased, with downstream activation of AKT. Similarly, (D) VEGFR-2 signaling decreased in response to an inhibitor, with additional downstream effects on the AKT pathway. Real-time monitoring of VEGFR-2 and AKT phosphorylation in 3D culture. FLIM images (A, C) and quantitative analysis (B, D) for VSOR and ASOR in 3D vasculature during 60 min of observation: (A, B) Fluorescence lifetime of VSOR and ASOR increases upon 10 ng/mL VEGF stimulation. (C, D) Fluorescence lifetime of VSOR and ASOR decreases within 10 min upon treatment with the inhibitor, Axitinib at 20 nM. Scale bar = 20 μm. n=3 biological replicates.

3.4.4 Multiplex Kinase Phosphorylation Monitoring in Zebrafish *In Vivo* Model.

After testing the ASOR and VSOR in 2D and 3D culture systems, we then evaluated the performance of both sensors for monitoring VEGFR-2−AKT signaling *in vivo*. Zebrafish was used as an *in vivo* model to further demonstrate our sensors and the imaging strategy. The uptake of sensors was highly efficient in the vascular system of anesthetized zebrafish (Figure 3.8a, Supplemental Figure 4) via intravenous microinjection through the caudal vein[151]. Biodistribution assay was also carried out in older 7 days' post-fertilization (dpf) larvae (Supplemental Figure 4) and younger embryo as early as 3 hpf (Supplemental Figure 4Supplemental Figure 4 Distribution of ASOR (bottom, red) and VSOR (top, green) 10 minutes after the sensor was microinjected into zebrafish at different

stages of development. (A, D) 3-hour post fertilization (3hpf) embryo; (B, E) five days post fertilization (5dpf); and (C, F) seven days post fertilization (7dpf).). Notably, rapid sensor uptake was observed within 5 min after injection in both ages of the fish and the sensors did not disrupt development of embryo into larvae (Supplemental Figure 5). The choice of 5 dpf larvae was based on our observation that larvae have a more developed organ than embryo and is more durable when transferring it from the microinjection platform to the FLIM system. Consistent with *in vitro* 2D and 3D results, VSOR signal within the vasculature area of live zebrafish increased within 20 min of VEGF stimulation (Figure 3.8A (white box), B (top), C). Subsequent increase in the signal of VSOR followed by ASOR upon stimulation with 100 ng/mL VEGF (Figure 3.8B (bottom), C) was observed. As observed in 2D and 3D cultures, the signal of VSOR decreased upon treatment with 200 nM of Axitinib within 60 min of observation (Figure 3.8E, white and blue arrow, D), indicating inhibited activity of VEGFR-2. Within 10 min of Axitinib treatment, lower signal of ASOR activity was observed, indicating a signaling cascade between VEGFR-2−AKT noting a decrease in VEGFR-2 activity to lower AKT activity. Interestingly, ASOR exhibited increased activity after 10 min of inhibition, indicating an elevation in AKT activity, which was also observed in 2D and 3D cultures. Our results in live zebrafish are consistent with our observations in 2D and 3D cultures, demonstrating the broad applicability and translation potential of our methodology from single cells to more complex systems, such as 3D cultures and live zebrafish.

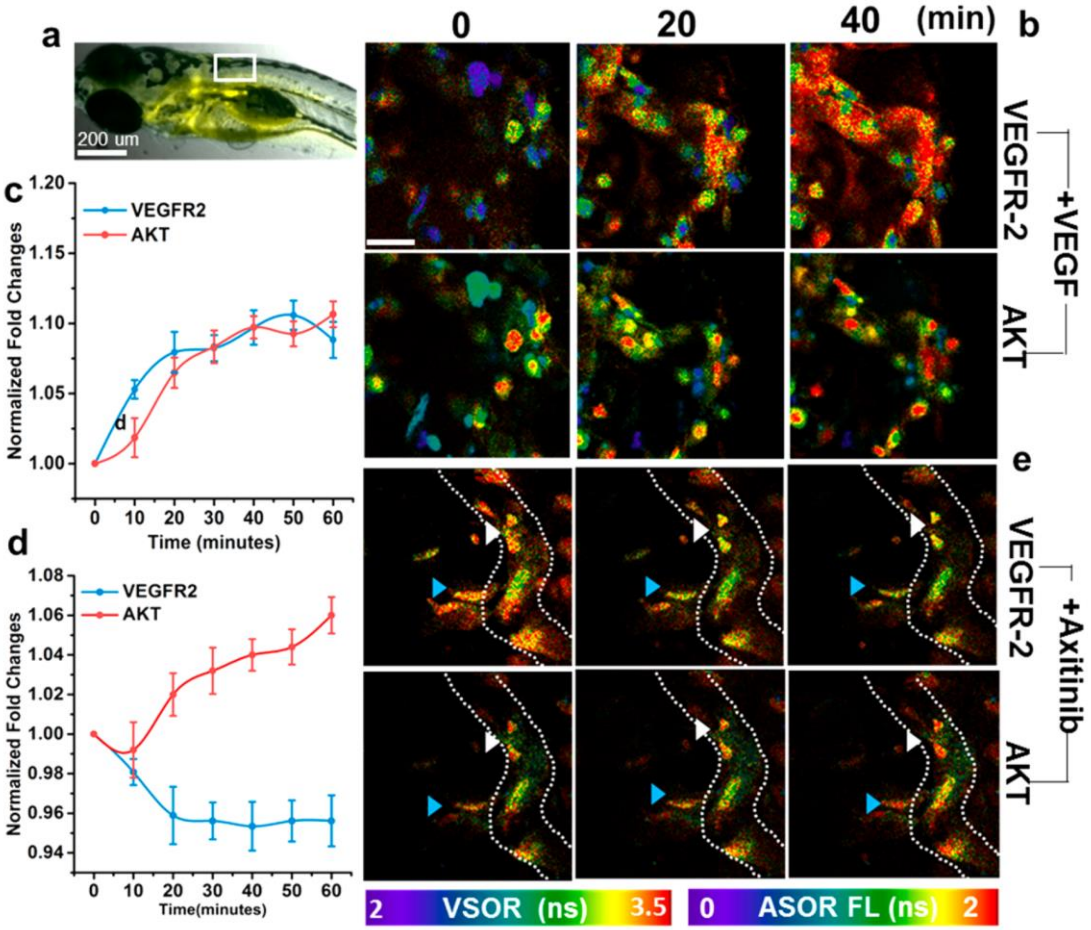

Figure 3.8 Endothelial cells within a zebrafish model demonstrated an appropriate response to VEGFR-2 (B) stimulation and (E) inhibition. (C) VEGFR-2 signaling increased, with downstream activation of AKT. Similarly, (D) VEGFR-2 signaling decreased in response to an inhibitor, with additional downstream effects on the AKT pathway. Real-time monitoring of VEGFR-2 and AKT phosphorylation in live zebrafish: (A) Sensor distribution in live 5 dpf zebrafish larvae. FLIM images (B, E) and quantitative analysis (C, D) of VSOR and ASOR in the vasculature (white box) of zebrafish depicted in (A) during 60 min of observation. (B, C) Fluorescence lifetime of VSOR and ASOR increases upon treatment with 100 ng/mL of the VEGF stimulant. (D, E) Fluorescence lifetime of VSOR and ASOR decreases within 10 min upon treatment with 100 nM of Axitinib. Scale bar = 20 µm. n=3 biological replicates.

3.4.5 Differences Observed Across 2D, 3D, and *In Vivo* Vascularization Models

While the general response remains mostly consistent between the three models—the promoter increases VEGFR2 and AKT activity, while the inhibitor decreases the activity—it is important to highlight subtleties within the data. Specifically, when looking closely at the inhibitor data for each model, an initial drop in AKT activity is observed

across all models. However, when looking at VEGFR2 in the 3D culture model, VEGFR2 barely dropped relative to AKT. On the other hand, within the 2D and *in vivo* models, VEGFR2 signaling was relatively much lower than that of AKT signaling. A possible explanation for this signaling discrepancy between models may be found in the FLIM images when comparing the 3D model with the likes of the 2D and *in vivo* models. The 3D model appears to be much more cell-dense than the other two models. It has been previously demonstrated that increased cell-cell contacts upregulates VEGFR2 signaling due to association via vascular endothelial-cadherin (VE-cadherin), a cell-cell adhesion molecule[153]. As such, this would explain why the increased cellular density of the 3D model would result in increased signaling of VEGFR2. This mechanistic claim could be probed in multiple ways. One way would be to apply the multiplex biosensors into an older zebrafish containing a more-developed vascular system. That way, the increased cell density of the developed vessel network would likely provide signaling closer to the 3D model. Another way would be to decrease the endothelial cell density of the 3D model. By decreasing the endothelial cell density within the 3D model, this would reduce the amount of cell-cell contacts and slow down the rate of vessel formation.

While we mentioned that AKT decreases in all groups, close observation of the AKT dynamics may reveal compensatory signaling mechanisms at play. When looking at the 2D and *in vivo* models when the inhibitor is introduced, relative recovery in AKT activity is observed by 30 minutes in 2D (82% to 94%) and 20 minutes *in vivo* (99% to 102%). For the 3D model, AKT demonstrated a steep drop however, the relative recovery was great (47% to 55%). Taken together, it appears that all models implemented VEGFR-2-independent compensatory mechanisms that upregulate AKT activity. For example, it has been demonstrated that activation of integrin-linked kinases (ILK) via phosphorylation will proceed to directly phosphorylate AKT[154]. AKT is downstream from many different signaling modalities, so survival can be maintained even if VEGFR-2 is not activated. For example, Ang1 has been shown to promote AKT activity, resulting in increased expression of survivin, an anti-apoptotic gene[155]. AKT activation in this manner is especially upregulated in cancers, specifically tumor vessel growth[156]–[158]. It is unsurprising that cancerous phenotypes have been associated with upregulated AKT signaling. There are even drugs on the market that aim to specifically inhibit AKT activity. Therefore,

elucidating mechanisms surrounding AKT would benefit researchers in drug discovery and oncology.

3.5 Conclusion

The work presented in this chapter highlighted the benefit of interlaboratory collaborative work by focusing on the integration of innovative tools, namely in-vitro 3D physiologic model of vasculogenesis (vessel formation) and a novel multiplex peptide biosensor. The oligomer-collagen-based multitissue model provided robust vessels that could be studied using the peptide biosensor multiplex. This work demonstrated great potential with the ability to live-track ECFC signaling in response to activators and inhibitors. The biosensor could be used to improve our understanding of ECFC mechanobiology as it relates to ECM stiffness. While VEGFR-2 is primarily known to respond to VEGF molecules, studies have shown that ECs cultured on moderately stiff polyacrylamide gels demonstrate an increase in VEGFR-2 expression[159]. It would be of great value to characterize the ECFC signaling when cultured in matrices of varying stiffnesses and relate it to the resulting vessel network that is formed. An additional application for these technologies would for optimizing the timing for grafting a vascularized tissue construct into a patient. It has been shown that when implanting a tissue construct, the vascular maturity of the ECs at the time of implant affects anastomosis[41]. As such, it would be of great value to live-track ECFC signaling throughout the duration of vessel formation within a tissue construct. With this information we could optimize the timing of graft placement in relation to the cell signaling. For example, it would be expected that a prevascularized tissue construct would be most successful if the EC are exhibiting the highest AKT signaling, since AKT signaling is correlated with both vessel formation and survival[160], [161]. Overall, this work highlights the benefits of collaborative research. The combination of these two technologies is expected to provide additional insight on vascularization mechanisms engineer tissue constructs for regenerative medicine applications.

CHAPTER 4. RAPID VASCULARIZATION OF DENSE TISSUE CONSTRUCTS ACHIEVED BY MAINTAINING CELL-MATRIX TENSIONAL FORCES OF CELL-DENSE TISSUE CULTURES

4.1 Overview

The ability to rapidly vascularize a dense tissue construct *in vitro* is valuable for engineering a dermal substitute. The success of graft integration with the patient relies on the vascularization of the graft. It has been shown that prevascularization of a tissue construct results in rapid anastomosis of the vessels in the graft with the host's vessels. However, it has also been shown that vascularization is impeded within tissue constructs that contain a denser extracellular matrix (ECM). Here, we controlled the design parameters identified in Chapter 2 to engineer the rapid vascularization of dense tissue constructs (>10 mg/mL collagen concentration). Within this work we encapsulated a high density of ECFCs (25×10^6 cell/mL) within densified oligomer collagen matrices (12 mg/mL, 20 mg/mL, and 40 mg/mL). Additionally, we incorporated a 3D-printed Tissue Tensioner culture device that maintained horizontal cell-matrix tensional forces throughout the duration of the 3-day and 7-day cultures. Within these studies, we observed rapid vascularization of dense tissue constructs by three days, demonstrating our ability to successfully scale-up the rapid vascularization results observed in Chapter 2. Additionally, we measured tissue thicknesses and found that as collagen fibril density was increased, there was an increased resistance to vertical cell-mediated contraction. Both of these results are significant as it relates to the engineering of a dermal substitute. The rapid vascularization of the tissue construct will reduce the production time to get to the patient, resulting in reduced scarring and contracture. Furthermore, the resistance to cell-mediated contraction demonstrated here is important for preventing scarring and contracture if the engineered tissue was grafted into a wound.

4.2 Introduction

A major challenge for tissue engineers is the rapid vascularization of tissue constructs *in vitro*. Vascularization is necessary for the survival of engineered tissues that

will be implanted *in vivo*. Tissue constructs that are vascularized before implantation (aka prevascularized) have demonstrated rapid anastomosis, or connection, to the host's blood vessels, allowing effective nutrient transport to the tissue-resident cells. Without prevascularization, a grafted tissue construct relies on vascular ingrowth from the vessels in the wound bed via angiogenesis, which moves slowly (~5μm/hr)[5]. For skin grafts, vascularized autografts have demonstrated the ability to grow with the patient. This is significant for pediatric patients whose skin grows many times over as they grow into adults. Unfortunately, there are currently no skin substitutes on the market that can grow with them. What we need is an engineered skin replacement that is rapidly vascularized so that it would adapt with a growing child.

When designing a tissue construct to be applied as a skin graft, it is important to consider the conditions that the engineered tissue construct may be submitted to not only throughout the procedure but also during the recovery process. First and foremost, the tissue construct must be easy to handle by the physician. Physicians are faced with many different presentations of wounds, so they must be able to manipulate the skin substitute easily. Therefore, any hydrogel-based tissue constructs would be too soft and therefore too difficult to handle. Next, the approach must be able to withstand sutures, since skin substitutes are normally sutured into the open wound area. Current soft-tissue engineering strategies employ tissue constructs that cannot retain sutures. Lastly, during the recovery process, the skin substitute will be sutured into a wound, which brings two problems: mechanical agitation and enzymatic degradation. For the former problem, wounds near jointed areas will experience more mechanical agitation. Therefore, the proposed engineered tissue must be mechanically stable to withstand these mechanical perturbations. For the latter problem, the wound environment contains proteases that will degrade the ECM to prepare the wound for new ECM synthesis. As such, skin substitutes containing substrates to these proteases (i.e., type I collagen) are subject to enzymatic degradation. Again, approaches that have implemented less-dense ECMs (< 3mg/mL collagen content) have demonstrated excessive degradation that renders the tissue construct unrecognizable. The ideal base biomaterial for a skin substitute should resist enzymatic degradation. What we need is an approach for vascularizing dense, mechanically stable tissue constructs.

However, vascularizing dense tissue constructs is not trivial due to the dynamic, yet finicky, nature of ECs.

One approach for prevascularizing denser tissue constructs involves the seeding of ECs onto the external portion of the scaffolds. Early approaches for prevascularizing tissue constructs were performed using top-down approaches (AKA prefabricated scaffolds), which include collagen sponges[47], [48], [162], electrospun scaffolds[163], [164], and decellularized tissues[45], [165]. Here, scaffolds were first created (fabricated or decellularized) then subsequently "seeded" with cells by adding culture medium containing ECs. Due to the dense nature of preformed scaffolds, the majority of the ECs remain on the periphery of the tissue construct. Since the ECs are aggregated at the outer surface of the tissue construct, this approach is no different from sprouting angiogenesis assays where ECs are seeded on top of hydrogels[166]. These approaches employ simulated angiogenesis, where the endothelial cell sheets must sprout into the tissue to vascularize it. However, due to the dense nature of these substitutes, seeded cells aggregate on the surface and slowly grow into the scaffold[45], [47], [48], [162], [165], requiring 2-4 weeks of *in vitro* culture time. Supp et al. demonstrated an *in vitro* penetration depth of ~100μm after 15 days of culture[47]. This distance is relatively short when considering the range of dermal thicknesses (0.6mm to 3mm). What we need, is a bottom-up approach that enables encapsulation of ECs throughout a dense, mechanically stable scaffold so the ECs may employ vasculogenic mechanisms to rapidly and extensively vascularize the tissue constructs.

Recently, the field has been transitioning the approach for vascularizing tissue constructs from a top-down to a bottom-up approach, incorporating solubilized matrix molecules such as fibrin (10 mg/mL) and collagen (3-6 mg/mL)[43], [49], [166]–[168] at higher-than-previously published concentrations. In these models, the ECs are mixed with soluble ECM, allowing the ECs to be distributed throughout the ECM before polymerizing into the final tissue construct. Here, the ECs were dispersed throughout the tissue construct rather than at just the periphery, and each dispersed cell could serve as a nucleation site for nascently formed vessels, resulting in thorough vascularization throughout the entirety of the tissue construct via vasculogenesis. While the ECM concentration of these studies is higher than traditional studies involving tissue construct vascularization, the employed

tissue constructs were still relatively less dense and therefore highly susceptible to degradation via the inflammatory cytokines found in the wound environment. Much of these problems can be attributed to the limitations of commercially available type I collagen (i.e., mechanically weak, pronounced cell-mediated contraction, slow and inconsistent polymerization times)[169]. Additionally, the collagen content in native skin is estimated to be around 40 mg/mL, so 6 mg/mL of collagen is still too low[170]. There is a need for a collagen-based, bottom-up approach that can achieve physiologic densities of collagen, increased mechanical properties, and resistance to degradation all while still facilitating vessel formation.

Currently, no work exists, to our knowledge, that demonstrates the ability to vascularize dense tissue constructs (>10 mg/mL collagen concentration) via cell encapsulation within an ECM. A reason for this gap is likely due to the well-known fact that denser tissue constructs impede vessel formation[52], [55], [58]. While encapsulating ECs in higher concentrations of collagen (~3mg/mL) has resulted in vessels with larger lumen, it has been found that increasing the ECM concentration too much inhibited vessel formation. This observation was due to spatial hindrance between endothelial cells—the cells are unable to sense and anastomose with one another[55], [56]. However, our lab has recently reported that increasing the EC density of a tissue construct while maintaining cell-matrix tensional forces may be an effective way to rapidly vascularize a tissue construct[141].

We have previously identified critical design parameters for rapidly vascularizing less dense (collagen concentration = 1.4 mg/mL) tissue constructs *in vitro*: i.) maintained cell-matrix tensional forces, ii.) increased EC seeding density, and iii.) presence of adipose stromal cells (ASC). Controlling these parameters resulted in rapid formation of ECFC vessels within the oligomer tissue constructs. However, the multitissue interface model incorporated a 5μL tissue sphere (diameter < 3 mm), which would have minimal therapeutic impact if it were applied as a wound therapy. To scale up the size and mechanical properties of our tissue constructs, our lab has shown that oligomer densification can be used to create large, mechanically stable tissue constructs without the presence of exogenous crosslinkers[28], [29]. Here, they demonstrated that this approach facilitates uniform distribution of cells, specifically ASC and chondrocytes[28], [29], and

does not affect cell viability. Unlike other tissue densification processes, our approach allows uniform cell encapsulation, which will be vital for whole-tissue vascularization. Furthermore, this densification technique has been shown to create tissue constructs that resist enzymatic degradation[28]. In the present work, we employed this densification approach in conjunction with insight gained from Chapter 2 to uniformly distribute a high density of ECFCs & ASCs while maintaining cell-matrix tensional forces (using a 3D-printed Tissue Tensioner culture chamber) to rapidly vascularize dense tissue constructs *in vitro*. Overall, this work demonstrated for the first time that physiologically dense tissue constructs can be rapidly vascularized *in vitro*.

4.3 Materials and Methods

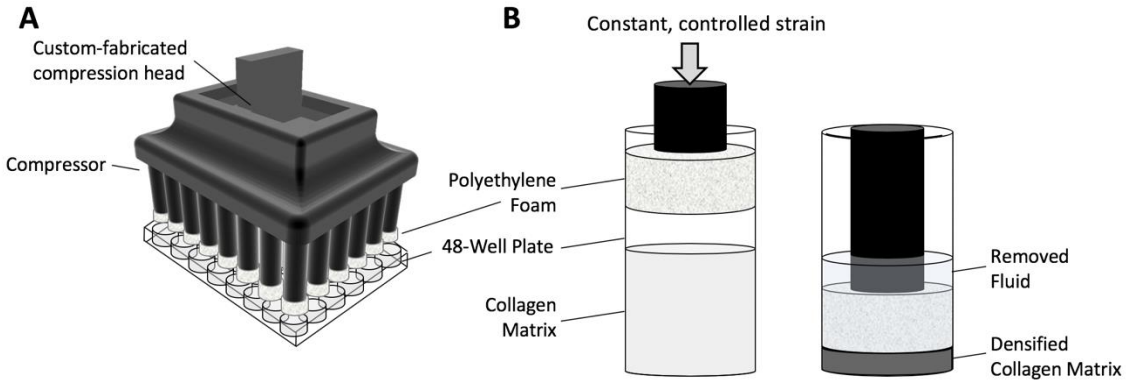

Figure 4.1 Schematic of medium-throughput confined compression device and tissue densification mechanism (A) Medium-throughput compression device, including 48-well plate and 3D printed compressor head. Adaptor-top facilitates integration with a mechanical testing instrument, enabling user definition of strain and strain rate. (B) Custom-fabricated polyethylene foam platens (10 mm diameter, 0.25" thick) facilitate even and controlled fluid flow out of tissue construct during compression, resulting in a densified collagen-fibril microstructure.

4.3.1 Fabrication of Compression Device for Medium-Throughput Compression

The medium-throughput compression device consisted of a custom-fabricated Compression Head with polyethylene platens and a standard 48-well culture plate. (Figure 4.1). The compression head was designed in SolidWorks (Dassault Systémes SolidWorks Corporation, Waltham, MA) and 3D printed using a 3D Printer (FORTUS 400mc, Stratasys). All 3D printed parts were cleaned as instructed according to manufacturer

specifications prior to use. Fabrication of the polyethylene foams started with a 0.25" thick sheet of ultra-high molecular weight polyethylene (PE) foam containing 50-micron pores (BB2062-50BL, Scientific Commodities Inc.). From these sheets, cylindrical PE foams (10 mm diameter) were cut out. Holes (5/16") were drilled out of the center of these PE foams, and allowed press-fit placement of the PE foams onto the 3D printed compressor device. The compression head was exposed to H_2O_2 gas plasma for 30 minutes. Afterwards, the PE foams were rinsed with sterile PBS to remove any residual H_2O_2.

4.3.2 Preparation of Type I Collagen Oligomers

Type I collagen oligomers were acid-solubilized from the dermis of market weight pigs and lyophilized for storage as described in a previous study[39]. The oligomer formulation was standardized based upon molecular composition as well as polymerization capacity according to ASTM International standard F3089-14[85]. Here, polymerization capacity is defined by matrix shear storage modulus (G', Pa) as a function of oligomer concentration of the polymerization reaction. All collagen solutions were diluted with 0.01 N HCl to achieve desired concentrations and neutralized with 10× PBS and 0.1 N NaOH to achieve pH 7.4[86]. Neutralized solutions were kept on ice prior to inducing polymerization by warming to 37°C.

4.3.3 Cell Culture

Human ECFC were isolated from umbilical cord blood and cultured as described in a previous study[87]. Low-passage human adipose stromal cells (ASC) were obtained from Zen-Bio (Research Triangle Park, NC). Both ECFC and ASC were propagated in complete endothelial cell growth medium (EGM-2, Lonza, Walkersville, MD) supplemented with 10% fetal bovine serum (HyClone, ThermoFisher Scientific, Waltham, MA). Cells were grown and maintained in a humidified environment of 5% CO_2 in air at 37°C. ECFC and ASC were used in experiments at passages between 8 and 13.

4.3.4 Preparation of Dermal Constructs

To create cellularized dermal constructs, ECFC and ASCs were added at specified densities to neutralized oligomer solutions (4.0 mg/mL). Cell-oligomer suspensions were pipetted into 48 well plates at specific volumes (342 µL, 570 µL, and 1140 µL) and

polymerized for 30 minutes at 37°C. Tissue constructs were densified to a final thickness of 1.2mm at a strain rate of 1.5mm/min using a universal mechanical testing machine (TestResources). Final oligomer concentrations (fibril densities) for the constructs were 12 mg/mL, 20 mg/mL, and 40 mg/mL, with final cellular densities of 25×10^6 ECFC/mL and 6.125×10^6 ASC/mL.

Immediately after compression, tissues were clamped into a custom-fabricated Tissue Tensioner and placed into petri dishes (Figure 4.2). The Tissue Tensioner was designed in SolidWorks (Dassault Systémes SolidWorks Corporation, Waltham, MA; Supplemental Figure 6 & 7) and created using a 3D Printer (FORTUS 400mc, Stratasys). The Tissue Tensioner consisted of two parts that clamp together onto the tissue construct in order to prevent to maintain tissue geometry and cell-matrix tensional forces. Additionally, the Tissue Tensioner design included channels that allowed medium access to the top and bottom of the tissue constructs. 25 mL of EGM-2 supplemented with 10% FBS and 1% penicillin streptomycin were added into the petri dishes. Medium changes were performed daily. Densified tissue constructs were grown for 3 and 7 days. All experimental groups were tested in triplicate (n=3). Acellular tissue constructs were densified to the same final oligomer concentrations (12 mg/mL, 20 mg/mL, and 40 mg/mL) and thicknesses were measured at day 0 (n=3).

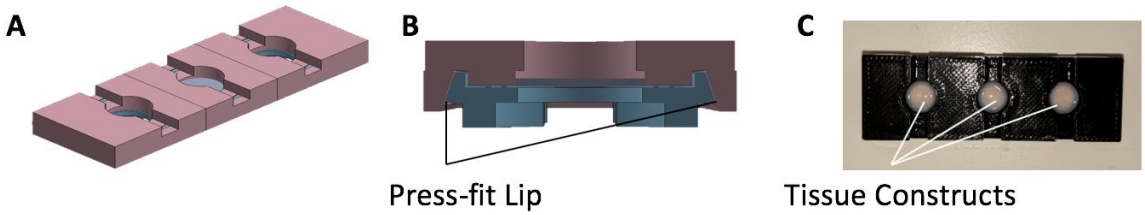

Figure 4.2 Schematic of custom-fabricated Tissue Tensioner for maintaining tissue geometry and cell-matrix tensional forces. To maintain cell-matrix tensional forces, the device clamped onto the outer edge of the tissue construct in place, preventing cell-mediated tissue construct contraction. (A) One complete device, with a collagen tissue in the middle chamber. (B) A front-facing view (C) Top-view showing a Tissue Tensioner with three 12 mg/mL tissue constructs.

4.3.5 Immunostaining of Tissue Constructs

After 3 days and 7 days of culture, tissue constructs were fixed in 4% formalin and then placed in a 30% sucrose solution. Afterwards, bisected tissue constructs were embedded in optimal cutting temperature (OCT, Fisher Scientific) solution and 60 µm sections were prepared using a Thermo Cryotome FE (Fisher Scientific, Kalamazoo, MI). Afterwards, the tissue slices were rinsed with 1× phosphate buffered saline (PBS), permeabilized with 1% Triton X-100, and blocked with 1% bovine serum albumin. The primary antibody, mouse anti-vimentin (V6389-200UL, Sigma; 1:200), was added and kept overnight at 4°C. Constructs were then rinsed with 1× PBS and incubated with the secondary antibody, AlexaFluor™488 goat anti-mouse (A-11001, Life Technologies, Carlsbad, CA; 1:200) overnight at 4°C. Next, tissue slices were rinsed with 1× PBS and counterstained with 4',6-diamidino-2-phenylindole (DAPI) to visualize cell nuclei. Once nuclear stains were confirmed under a fluorescent scope, tissue slices were rinsed before setting with antifade mounting medium (Vectashield™; H-1200, Vector Labs, Burlingame, CA).

4.3.6 3D Confocal Microscopy Image Acquisition

For 3D qualitative analysis, tissue constructs were imaged using a Zeiss LSM 880 confocal system adapted to an inverted microscope (LSM 880, Zeiss). Image stacks were collected from one spot within each of the three independent tissue constructs per experimental group. Z-distance between each slice was 2.5 µm. The complete imaging volume was (853.333µm × 853.333·Yµm × 50µm), where Y is the number of tile scans that were performed. If the thickness of the tissue construct was greater than the imaging window, multiple image tiles were taken to capture the full thickness of the tissue construct. ZenBlue software was used to create z-projections of each image stack.

4.3.7 Tissue Construct Thickness Measurement

To measure the thickness of a given tissue construct, we imported the tile-scanned z-stacks into ImageJ. Once opened, the global scale was set for the ImageJ session using parameters from the image (1.2 pixels/µm). Using the line tool, a measurement was made across the tissue to measure its thickness at three locations: near the top, near the middle,

and near the bottom. These three measurements were then averaged. The same measurements were made for each tissue construct within each group (n=3) at each time point (day 0, day 3, and day 7). To normalize the data, each group's measured tissue thickness was divided by the thickness of that respective group at day 0.

4.3.8 3D Vessel Morphology Analysis

To analyze the morphology of ECFC vessel networks, previously captured confocal image stacks were cropped down to the specified volume: (213.333μm × 426.666μm × 50 μm). There were three images analyzed for each experimental group (n = 3). Images were analyzed using a previously reported method[38]. Briefly, images were imported into Imaris (Bitplane) and the Filament Tracer software was used to generate filamentous microstructures that approximate the vessel network. With this software, various vessel morphological parameters could be analyzed: vessel volume percentage, total vessel length, vessel diameters, vessel lengths, and vessel volumes. Here, vessel segments that were less than 20μm in length were not included in the analysis.

4.3.9 Cryogenic Scanning Electron Microscopy

To visualize the remodeled collagen fibrils, tissue constructs were imaged using an FEI NOVA nanoSEM 200 (FEI, Hillsboro, OR). Samples were flash-frozen by submersion into critical point liquid nitrogen. Afterwards, samples were transferred to a CD1000 cold-stage attachment (Oxford Instruments North America, Inc., Concord, MA), and sublimated under vacuum for 10 minutes. Samples were then subsequently sputter coated with platinum and ready for imaging. Images were taken at 3000× and 5000×.

4.3.10 Statistical Analysis

Statistical analyses were performed using statistical analysis software (Minitab, State College, PA. Unless otherwise stated, comparisons were made using one-way analysis of variance (ANOVA) with a Tukey post hoc test. A critical global p value of 0.05 was used.

4.4 Results and Discussion

4.4.1 Culturing Tissue Constructs within the Advanced Tissue Construct Culture Device Prevents Cell-Mediated Tissue Construct Contraction in the Horizontal Direction

Tissue constructs were immediately placed into an advanced tissue culture chamber after confined compression. These advanced tissue culture chambers provided two functions: i.) to prevent cell-mediated tissue construct contraction and ii.) to maximize cellular access to nutrients. In regard to the former, the culture chamber consists of two parts that come together in a press-fit manner that lock in place. The chamber pinches down around the tissue construct to hold it in place. As such, contraction in the horizontal direction is prevented and thus cell-matrix tensional forces are maintained. Regarding the access to nutrients, channels were designed to allow cell culture medium to flow freely across the top and bottom of the tissue constructs. Preliminary studies were performed that demonstrated enhanced nutrient delivery in the advanced tissue culture chambers as compared to tissue constructs cultured within the well plate alone (data not shown).

4.4.2 Tissue Construct Contraction Depends on ECM Density and Time

Tissue constructs were set to be compressed to a thickness of 1.2 mm. Measurements of each tissue construct's thickness were taken at 0, 3 and 7 days after the tissues were fixed (Figure 4.3 and Figure 4.4). Initial measurements of tissue constructs right after compression (day 0) showed tissue thicknesses of 1794 ± 100.3 μm, 1836 ± 124.4μm, 1680 ± 123.4 μm for 12 mg/mL, 20 mg/mL, and 40 mg/mL, respectively. After three days of culture, the tissue thicknesses were measured at 755.8 ± 101.8 μm, 1105 ± 177.0 μm, and 1630 ± 381.4 μm for the 12 mg/mL, 20 mg/mL, and 40 mg/mL tissue constructs, respectively. This data demonstrates that the amount of vertical compression of the tissue construct decreases as the initial ECM density increases. Measurements of tissue thickness after seven days of culture further highlighted this point: 491.9 ± 25.78 μm, 901.8 ± 208.6 μm, 1556.9 ± 61.87 μm for the 12 mg/mL, 20 mg/mL, and 40 mg/mL tissue constructs, respectively. The tissue constructs that were initially compressed to higher initial collagen concentrations experienced the least amount of contraction. Each group was statistically different from each other at days 3 and 7. The increased resistance to contraction is partly due to increased compressive modulus as collagen oligomer

concentration is increased[28], [171]. Compressive modulus represents a material's ability to resist compressive deformation; therefore, increasing this parameter would increase the resistance to collagen compaction.

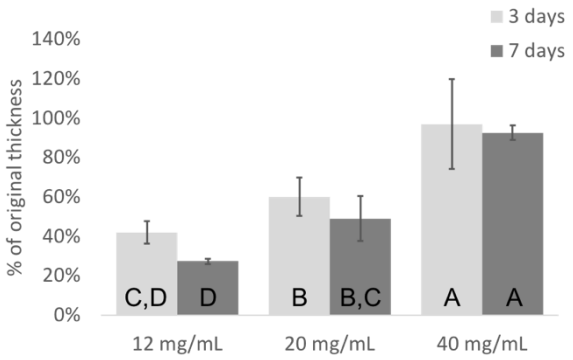

Figure 4.3 Bar graph showing the thickness of the various groups of tissue constructs. As collagen fibril density was increased, there was increased resistance to matrix deformation. Although not statistically significant, there was increased matrix deformation as time was increased. Compared statistically using Tukey's test. Different letters indicate statistically different groups ($p < 0.05$). n=3

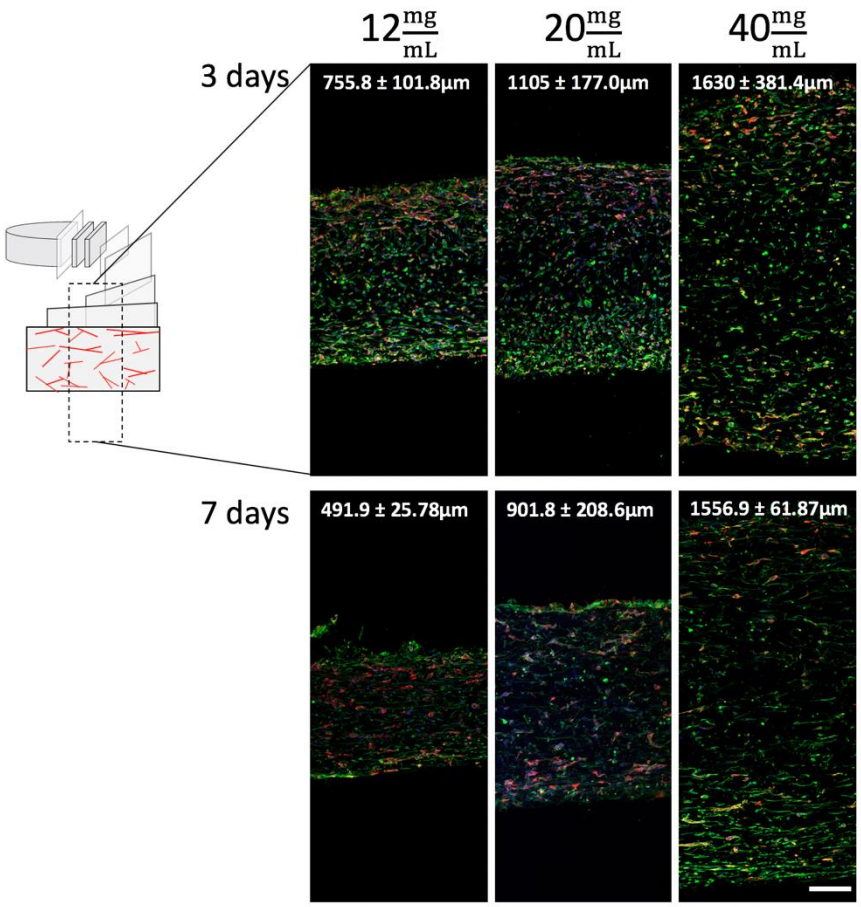

Figure 4.4 Increasing collagen fibril density of tissue constructs increased the tissue constructs resistance to deformation. Projections of confocal image stacks (50 µm thick) illustrating vessel network formation within the densified tissue constructs after 3 and 7 days of culture. ECFCs and ASCs were encapsulated in oligomer tissue constructs and densified to reach final densities of 25×10^6 ECFC/mL and 6.25×10^6 ASC/mL. ECFC were transfected with TdTomato (red fluorescence). All cell populations were stained with anti-vimentin (green fluorescence) and DAPI (blue fluorescence). White numbers at the top of each image represent the average thickness for that specific group. Scale bar = 200 µm.

4.4.3 Dense Oligomer Tissue Constructs were Rapidly Vascularized Using Increased Cell Concentrations While Maintaining Cell-Matrix Tensional Forces

The ability to achieve rapid *in vitro* vascularization within dense tissue constructs (type I collagen concentration > 10 mg/mL) within a week is a feat that has not been previously achieved. Here, we present confocal images demonstrating vascularization of collagen tissues with densities ranging from 12 mg/mL to 40 mg/mL. After 3 and 7 days, tissue constructs were stained and analyzed via confocal microscopy (Figure 4.5A). In terms of overall tissue vascularization, there was a decrease in vessel volume percentage

as the tissue construct collagen fibril density was increased (Figure 4.5B). Specifically, the vessel volume percentages were 5.38 ± 2.82%, 3.05 ± 0.80%, and 1.25 ± 0.53%, for the 12 mg/mL, 20 mg/mL, and 40 mg/mL tissue constructs, respectively at 3 days. At 7 days, the vessel volume percentages were calculated at 2.91 ± 0.35%, 2.40 ± 1.50%, and 1.43 ± 0.53%, for the 12 mg/mL, 20 mg/mL, and 40 mg/mL tissue constructs, respectively. Within our vascularized, dense tissue constructs, we observed a decrease in vessel formation as the ECM concentration was increased, which corroborates previous findings by other groups[55], [56]. An additional trend (not statistically significant) observed in our tissue constructs was a decrease in vessel volume percentage from 3 to 7 days for the 12 mg/mL and 20 mg/mL groups. One explanation for this drop in vessel volume percentage is vessel regression, which has been observed by Cross et al.[55]. The vessel formation process is very dynamic, and once ECs form vessels, they require stimuli in order to persist. If these signals are not achieved or maintained, the ECs will regress, as their stimuli indicates that vessels are no longer needed in that location[172].

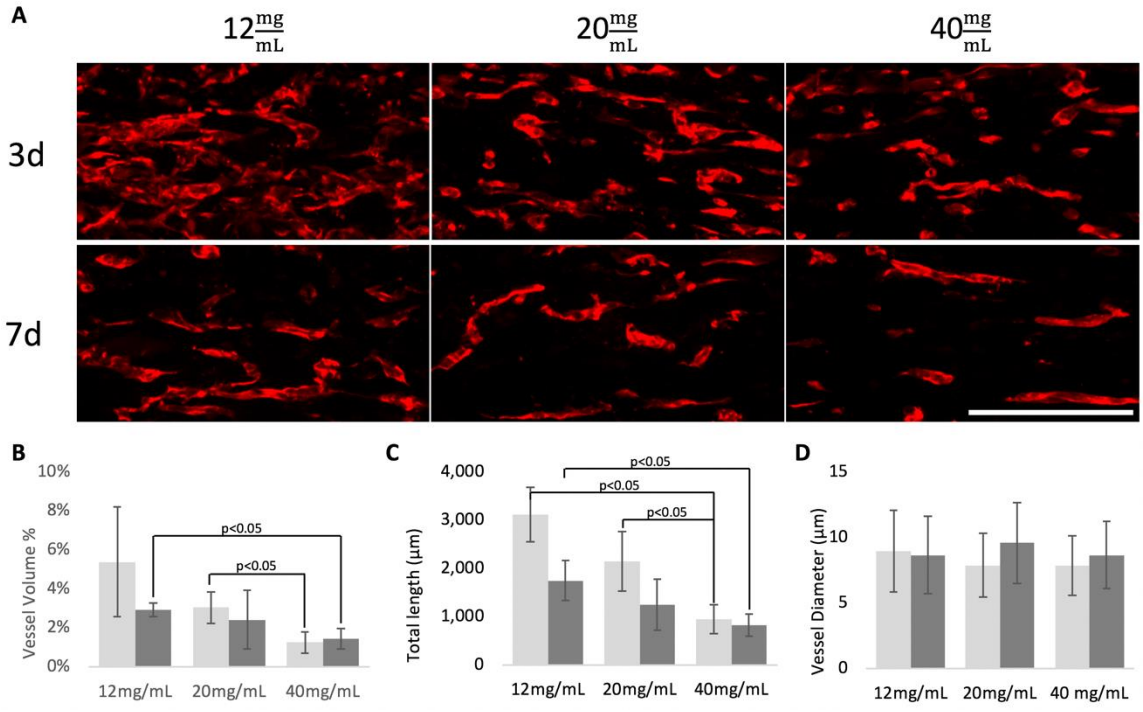

Figure 4.5 ECFC vessel formation was achieved within all tissues. As collagen fibril density was increased, there was decreased (B) vessel volume percentage and (C) total vessel length at 3 and 7 days. (D) Vessel diameters were not statistically different from one another. (A) Projections of confocal image stacks (50 μm thick) illustrating vessel network formation within the densified tissue constructs after 3 and 7 days of culture. Scale bar = 200 μm (B) Plot comparing the average vessel diameters of each group at 3 and 7 days. (C) Plot comparing the vessel volume percentage of each group at 3 and 7 days. (D) Plot comparing the total length of the vessel structures at 3 and 7 days. Scale bar = 200 μm. Comparisons made using two sample T-tests.

Regarding the total length of the vessels in each tissue construct (Figure 4.5C), there appeared to be a decrease in total length as collagen fibril density was increased. Specifically, the total vessel lengths were 3119 ± 564.2 μm, 2144 ± 621.1 μm, and 944.7 ± 301.8 μm, for the 12 mg/mL, 20 mg/mL, and 40 mg/mL tissue constructs, respectively at 3 days. At 7 days, a similar trend was observed. Here, the total vessel lengths were measured at 1749.32 ± 416.6 μm, 1253 ± 528.8 μm, and 830.0 ± 225.7 μm, for the 12 mg/mL, 20 mg/mL, and 40 mg/mL tissue constructs, respectively. When comparing each tissue group at 3 and 7 days, there was a noticeable trend of decreasing total vessel length.

Distributions of vessel morphological parameters are presented in Figure 4.6, Figure 4.7, and Figure 4.8. Although vessel diameters were not statistically different from one another (Figure 4.5D), there appeared to be noticeable trends in the distribution of vessel diameters (Figure 4.6). After three days of culture (Figure 4.6, A), all tissue groups seemed to have vessels with similarly distributed diameters. Overall, each group showed the highest fraction of vessels with diameters 4-8μm. Taking a closer look, it appeared that a slightly greater fraction of vessels in the 40 mg/mL tissue constructs existed at smaller diameters (4-8μm). The 12 and 20 mg/mL groups seemed to have vessels with diameters of at least 16μm, while the largest diameter vessel for the 40 mg/mL group was in the range of 12-16 μm. Furthermore, the 12 mg/mL group was the only group containing vessel diameters in the 20-24 μm range. At 7 days, the vessel diameter distribution changed. Here, the 12 mg/mL group had the highest fraction of vessels in the 4-12μm range, while the 40 mg/mL had the highest fraction in the 4-8 μm range. Alternately, the 20 mg/mL group demonstrated the highest fraction of vessels in the 8-12μm range. Similar to observations made at 3 days, the 40 mg/mL group did not contain vessels with diameters greater than 16μm at 7 days. For the 12 mg/mL group, the largest vessel diameter was in the 16-20μm

range. Surprisingly, the 20 mg/mL had the largest diameter vessel falling in the range of 20-24 µm.

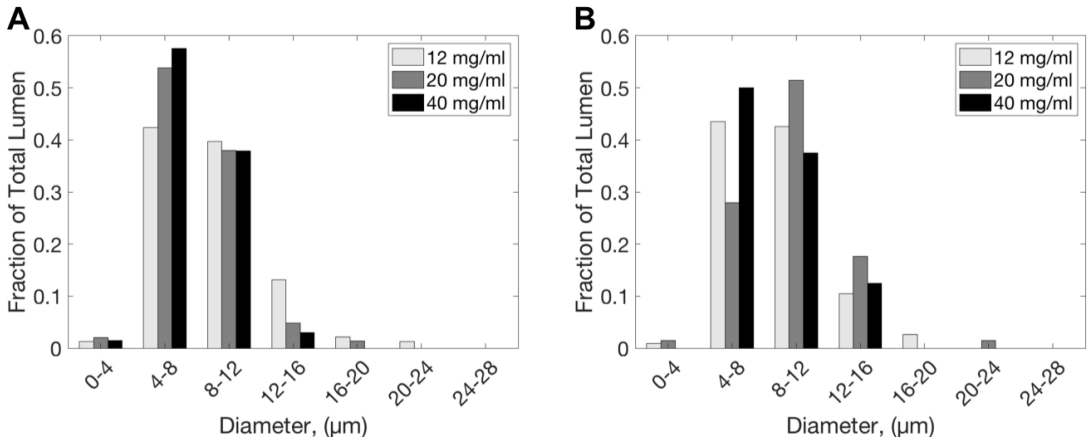

Figure 4.6 At 3 days (A), the ECFC within the least dense matrices had the most vessel segments at the largest diameters (16-24µm). At 7 days (B), the largest diameter vessel segments were in the 20 mg/mL group, with the second largest being in the 12 mg/mL group. Comparison of ECFC vessel diameter fractional distributions at (A) 3 days and (B) 7 days at the specified collagen fibril densities (12, 20, and 40 mg/mL).

Figure 4.7 shows the distribution of vessel segment lengths at 3 and 7 days. The number of occurrences for each length of vessel segment can be seen in Figure 4.7, A-B. At 3 days (Figure 4.7, A), the 12 mg/mL group appeared to have the most counts in each category overall, followed by the 20 mg/mL and then the 40 mg/mL groups. Overall, the 12 and 20 mg/mL groups contained more counts of vessel segments that exceeded 100µm in length. When looking at the distribution by fraction of total lumen per group (Figure 4.7,C), the relative fraction seemed similar between all three groups. Figure 4.7, B shows the total number of occurrences for each length of vessel segment after 7 days of culture. Like the 3 day analysis, the 12 mg/mL group contained a higher frequency of each vessel segment length, with the exception of vessels that exceed 90µm in length. At the longest group (100+µm), the number of longer vessel segments (100+µm) was the same between each group. These results are further highlighted when looking at the fraction of total lumen (Figure 4.7,D). While the distribution was similar for the lower length groups (20-70 µm), there appeared to be a larger fraction of longer vessels in the denser tissue constructs groups (20 and 40 mg/mL).

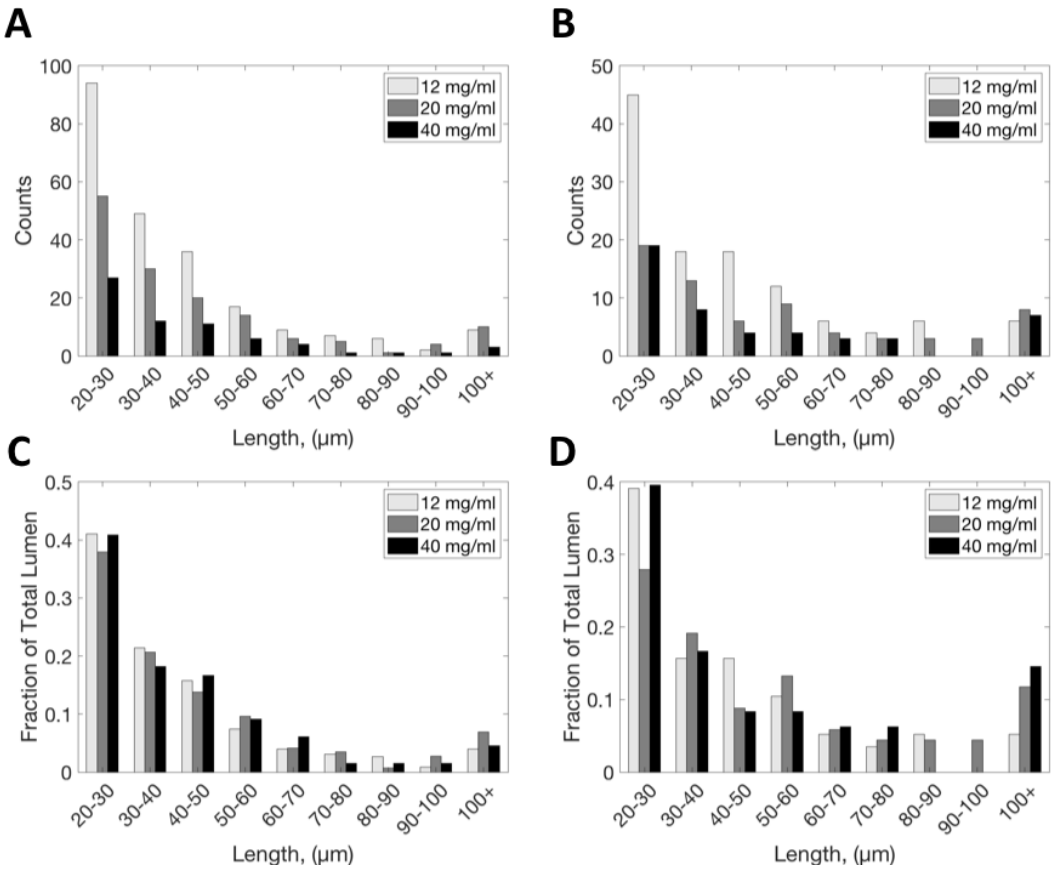

Figure 4.7 At 3 days(A, C), there were more longer vessel segments (>100μm) in the 12 and 20 mg/mL groups. At 7 days (B,D), all groups contained a similar number of long vessel segments (>100μm), with the denser group containing a larger fraction of long vessel segments. Comparison of ECFC vessel segment length distributions at 3 days (A,C) and 7 days (B,D) at the prepared initial collagen fibril densities (12, 20, and 40 mg/mL). (A-B) Plots showing the distribution of each vessel segment length. (C,D) Plots showing the fractional distribution of vessel segment length.

Figure 4.8 shows the distribution of vessel segment volumes at 3 and 7 days. The number of vessels that fall under each volume group can be seen in Figure 4.8, A-B. At 3 days (Figure 4.8A), there was an overall higher count of the 12 mg/mL group than the other groups. However, when looking at the fractional distribution of occurrences, all groups appeared to be the same with an exception at the largest volume (4000+μm^3). At this volume, the 12 and 20 mg/mL groups had a higher fractional occurrence. After 7 days of culture, the 12 mg/mL group showed more occurrences at each volume of the lower volumes (400-2400μm^3) but appeared similar number of times in the range of 2400-3200μm^3. Interestingly, at the highest volume group (4000+μm^3), there were slightly more

occurrences in the 40 mg/mL group and more than double the number of occurrences in the 20 mg/mL group. When looking at the fractional counts after 7 days of culture (Figure 4.8,D), the majority of the vessel segments in the 12 mg/mL group were of smaller volume (400-1200 µm3). Interestingly, there was a large fraction of large-volume vessels (4000+µm3) in the 20 mg/mL group. By comparison, the 40 mg/mL group appeared only about half as many times and the 12 mg/mL group appeared less than a quarter number of times that of the 20 mg/mL group.

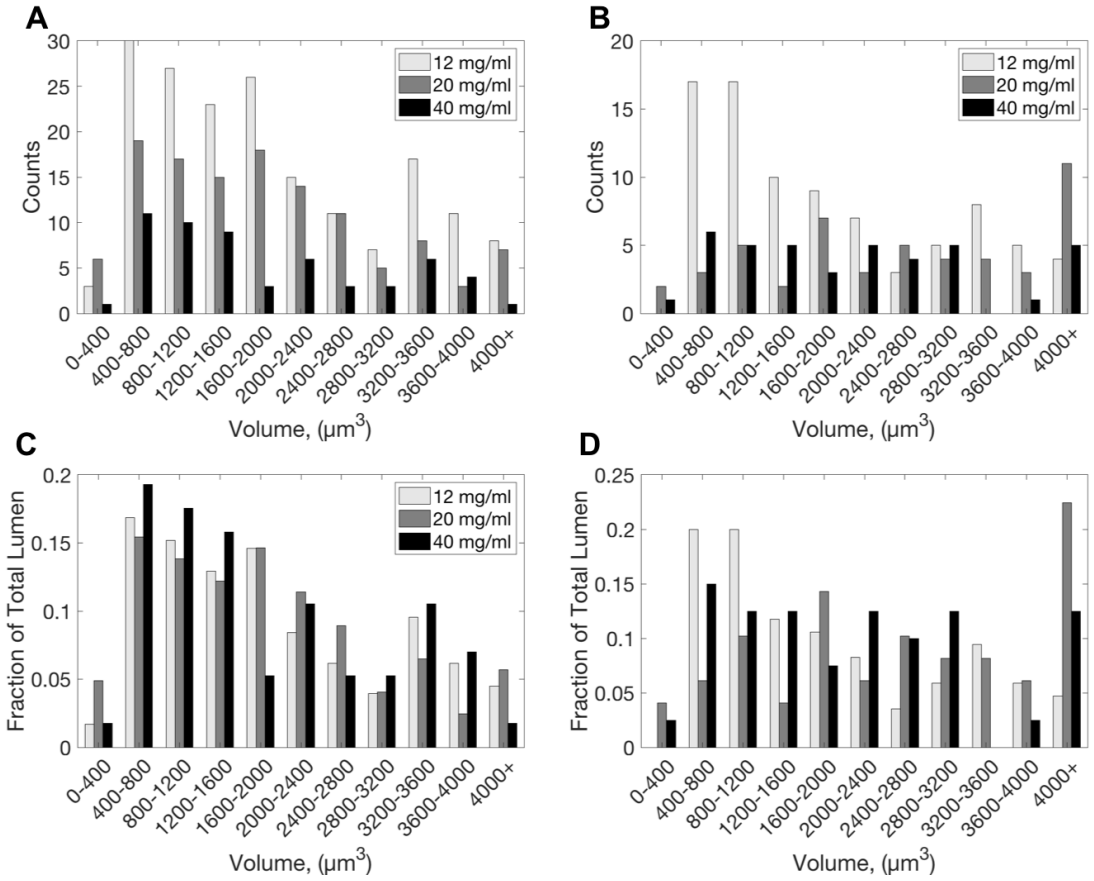

Figure 4.8 At 3 days, there are more large volume segments (>4000µm^3) in the 12 and 20 mg/mL groups. At 7 days, the 20 mg/mL group contains the greatest number of long vessel segments (>4000µm^3). Comparison of ECFC vessel segment volume distributions at 3 days (A,C) and 7 days (B,D) at the prepared initial collagen fibril densities (12, 20, and 40 mg/mL). (A-B) Plots showing the distribution of each vessel segment volume. (C,D) Plots showing the fractional distribution of vessel segment volume.

4.4.4 Vessel Structures are Formed More Rapidly in Less Dense Matrices

Overall, the 12 mg/mL group appeared to develop vessels the quickest, as demonstrated by the distributions at 3 days (Figure 4.6A, Figure 4.7A, Figure 4.8A). Specifically, at 3 days, the 12 mg/mL group contained a larger fraction of vessels at the largest volumes and diameters. This observation was reasonable, since larger diameter vessels correspond with larger vessel volumes. One likely explanation for the rapid vessel formation within the 12 mg/mL tissue construct was that this group represented the least dense ECM. Since each tissue contained the same starting ECFC density, these ECFCs had less ECM material between one another, making it easier to sense and connect with one another. This is supported by the idea that ECM degradation is the limiting factor for vessel invasion[173]. As such, the ECs could degrade and sprout through the 12 mg/mL tissue construct more easily. In contrast, denser ECMs imposed a steric hindrance, preventing the cells from sensing one another and forming vessels[55]. An additional explanation for the rapid vascularization within the 12 mg/mL group can be observed in Figure 4.3. Specifically, the 12 mg/mL experienced the most cell-mediated contraction in the vertical direction. As such, this compaction of the collagen matrix would have increased apparent ECFC density by bringing the ECFCs closer to one another, making it easier for them to anastomose with one another. Additionally, cell-matrix tensional forces were maintained in the horizontal direction, which explains why vessels were oriented along the horizontal plane[100]. It has been previously reported in our lab that increasing the ECFCs to very high densities while maintaining cell-matrix tensional forces increased the vessel volume percentage[141]. It is likely that the increased vascularization rate and volume observed in the 12 mg/mL was due to a combination of the cell-matrix and cell-cell interactions within this system.

While the 12 mg/mL developed quickly by 3 days, both the 20 mg/mL and 40 mg/mL groups contained vessel segments with higher fractions of the vessel population having larger volumes and lengths at 7 days (Figure 4.7B, Figure 4.8B). One explanation for this is that these denser tissue constructs contained more ECM material, which hindered the ability of the EC vessels to sprout and branch[55]–[57]. This has been observed by Sieminski et al., where their ECFCs demonstrated less branched and interconnectedness of vessels when the collagen ECM was too stiff. In the present model, ECFCs were unable to

degrade the matrix, which resulted in less branching. As such, the vessel segments were larger in both length and volume. An additional explanation for the increased vessel diameter within the 20 mg/mL and 40 mg/mL at 7 days is that these denser tissue constructs experienced the least amount of vertical tissue contraction. Since the ECs in these did not deform the ECM as much, they continued to grow without pulling in the surrounding ECM. As shown in Chapter 2, matrix contraction results in smaller vessel segments. However, it is important to consider the delicate balancing act involved within tissue vascularization at these densities. Although the 40 mg/mL group resisted collagen deformation the most, the 20 mg/mL contained the largest vessel segments in terms of diameter and volume. As mentioned previously, this is likely due to limiting factors of vessel formation associated with local matrix degradation.

4.4.5 SEM Images Reveal Similar Collagen Fibril Density Between Groups

Scanning electron microscope (SEM) images were taken to visualize the collagen fibril microstructure of the ECFC vascularized tissue constructs after 7 days of culture (Figure 4.9). Within the collagen, voids were observed, which were likely created by an ECFC or ASC, depending on the size of the void. The higher magnification images (Figure 4.9, bottom) focused on what appears to be vessels within the collagen. Despite the collagen fibril densities being initially set to 12 mg/mL, 20 mg/mL, or 40 mg/mL, all of the groups appear to contain similar densities of collagen fibrils. In fact, the 12 mg/mL group appears to have the smallest pores while the 20 mg/mL and 40 mg/mL groups appear to have similar, slightly larger pore sizes. One explanation for this can be found when looking at the tissue contraction data (Figure 4.3). Here, the 12 mg/mL group demonstrated the most vertical contraction. Estimating the collagen concentration based on thickness of the tissue construct at 7 days resulted in 26.1 mg/mL, 23.2 mg/mL, and 29.4 mg/mL, for 12 mg/mL, 20 mg/mL and 40 mg/mL, respectively. Interestingly, the ECFC and ASC have contracted each tissue construct to very similar final collagen fibril densities. These results would follow previous findings by Sieminski et al., where they described endothelial cells achieving a force-balance between cell traction and apparent ECM stiffness[52]. ECMs were contracted to similar final ECM densities, which have been previously correlated to mechanical properties[52], [91], [174]. However, the extent of cell-mediated remodeling

was not measured, so this claim would need to be further validated by taking measurements of the mechanical properties after matrix remodeling. Furthermore, these measurements would need to be made on the local ECM mechanical properties and could be achieved using atomic force microscopy (AFM)[175].

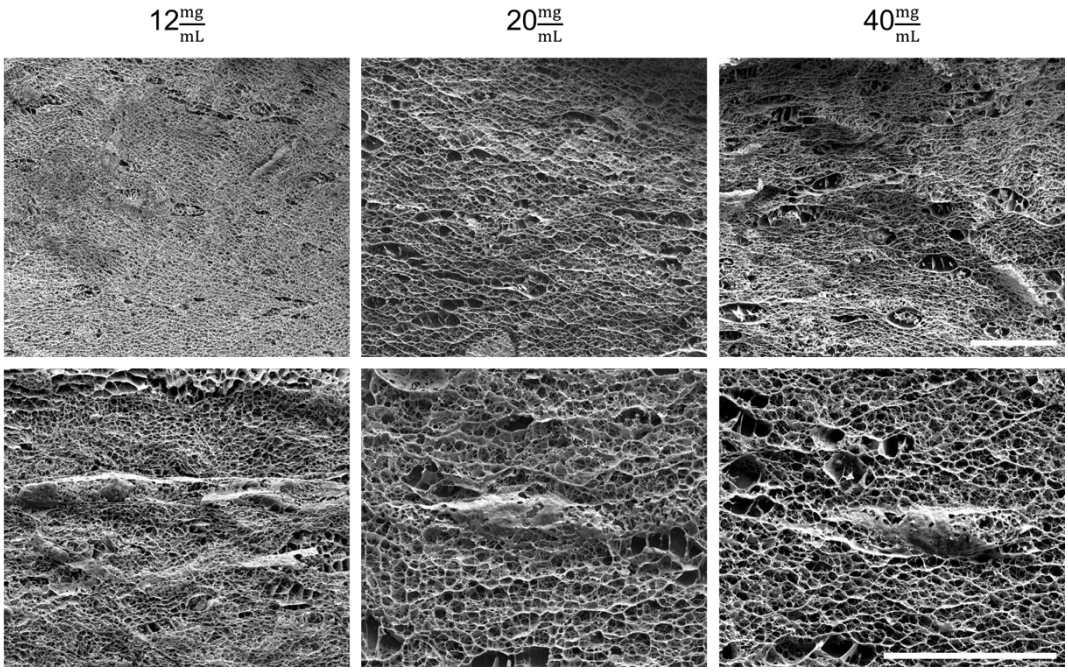

Figure 4.9 Qualitatively, ECFCs contracted the oligomer matrices to similar final densities. Scanning electron microscope (SEM) images of the ECFC vascularized tissue constructs after 7 days of culture taken at (TOP) 1500× magnification and (BOTTOM) 3000× magnification. Cryo-SEM was performed to visualize the dense collagen fibrils. All groups contain a dense arrangement of collagen fibrils. Void spaces in the collagen represent vascular tunnels carved out by ECFCs. Scale bar = 50 μm.

4.5 Conclusion

The major contribution of this work was demonstrating the ability to rapidly vascularize dense tissue constructs *in vitro*. We implemented oligomer densification, which enabled the encapsulation of ECFCs throughout the tissue constructs so they could form vessels via vasculogenesis. To overcome matrix-inhibition of vessel formation that is observed at high ECM densities, ECFCs were encapsulated at extremely high densities. Additionally, the Tissue Tensioner maintained cell-matrix tensional forces under these high cell densities and while maximizing the cell's access to nutrients. Vessel formation

was observed in all tissue densities, with increased vascularization in the less dense tissue constructs. Additionally, we postulate that the encapsulated cells contracted the matrices to similar final densities due to their desire of specific cell-matrix tensional force. Collectively, these findings highlight the importance of endothelial cell-matrix interactions and the associated mechanotransductive signaling pathway. Further optimization of design parameters related to densified matrices, specifically fibril density and microarchitecture as well as ECFC density, will provide additional insight to vascularizing dense tissue constructs.

CHAPTER 5. DENSIFIED OLIGOMER TISSUE CONSTRUCTS RESIST WOUND CONTRACTION AND FACILITATE INTEGRATION WHEN GRAFTED ONTO RAT EXCISIONAL WOUNDS

5.1 Overview

We have described the *in vitro* engineering of rapidly vascularized, dense tissue constructs to be applied as a treatment for pediatric skin defects. While the data collected *in vitro* demonstrated the therapeutic potential of the engineered tissue, it could not capture its performance if it were to be grafted into a wound *in vivo*. As such, it was necessary to develop an animal model for testing tissue-engineered treatments for skin defects. Specifically, we developed a rat excisional wound model and applied different acellular, oligomer-based tissue constructs (4 mg/mL, 20 mg/mL, and 40 mg/mL) into the full-thickness defect. Unlike the 20 mg/mL and 40 mg/mL groups, the 4 mg/mL tissue construct was not densified. Additional groups we employed were autografts (positive control), no treatment (negative control), and Helicote (collagen sponge, commercial comparison). We employed acellular tissue constructs to define the host's wound healing response to the biomaterial. The specific outcomes we defined were tissue contraction, recellularization, tissue integration, and vascularization; we found that these outcomes were reduced with increasing oligomer collagen fibril density. However, all oligomer tissue constructs were infiltrated by the host's cells, highlighting the natural cell adhesions sites present in the oligomer. In contrast, the Helicote contains particulated collagen that is cross-linked, which masked cell adhesion sites. Furthermore, cryogenic SEM revealed that the collagen microstructure of the densified oligomer tissue constructs appeared structurally similar to native rat skin, while the Helicote appeared different from the other groups. Overall, the results of this work demonstrated that the densified oligomer collagen is readily cellularized and vascularized by the host's cells. These results validate that the material is a suitable base-biomaterial for dermal regeneration, since it resisted wound contraction and did not degrade, but rather integrated with the host. Furthermore, defining the wound response to acellular oligomer-based tissue constructs will help discern the contribution of

vascularization to wound healing in future studies that implement vascularized oligomer-based tissue constructs.

5.2 Introduction

A major clinical problem for children are large, full-thickness skin defects. Here, this open wound must be covered immediately to prevent infection and, even worse, death[176]. The gold standard of treatment for full thickness defects is an autograft; however, when patients experience large, full-thickness skin defects that cover greater than 2% of their total body surface area, there is limited availability and donor site morbidity[3]. In this case, skin substitutes do provide immediate wound coverage; however, current skin substitutes on the market do not grow with pediatric patients, leading to lifelong suffering[177], [178].

Graft characteristics are important determinants for ideal wound healing outcomes (i.e., reduced scarring and contracture). One important determinant for preventing wound contraction is the graft's mechanical stability. Dermal substitutes on the market are preferred over epidermal and dermo-epidermal substitutes because they offer greater mechanical stability that results in reduced wound contraction[18]. Other determining characteristics are the graft's ECM density and microarchitecture, which cells have shown to directly interact with and respond to[179]. The ideal dermal substitute would provide the host's infiltrating cells with cues for skin regeneration rather than scar tissue formation[180]. When surveying currently available dermal substitutes, there are two major categories: decellularized tissues and collagen sponges[23]. Decellularized tissues provide an intact ECM that cells recognize and grow into. However, the process for decellularizing allogeneic and xenogeneic tissues requires a careful balance: excessive processing denatures the extracellular matrix proteins, preventing cellular recognition, while inadequate processing results in residual cell remnants that cause immune rejection[20], [181]. Furthermore, the process for tissue decellularization aims to retain the microarchitecture of native ECM, which is quite dense. As such, the dense ECM has been shown to hinder cell invasion, resulting in delayed recellularization and vascularization[182]. Delayed healing responses are not ideal, as they have been shown to facilitate scarring and contracture outcomes[183]. The other acellular dermal substitutes

are collagen sponges (i.e., Integra), which are created through processing tissue particulate along with other additives (i.e., glycosaminoglycans (GAGs)). The scaffold is then exogenously crosslinked to enhance its mechanical stability and degradation profile and reduce immunogenicity[184]–[186]. However, exogenous crosslinking has been shown to mask cell binding sites, be cytotoxic, and result in calcification[30], [187]–[189]. Just like decellularized matrices, the crosslinked collagen sponges exhibit slow recellularization and revascularization times[5], [190]. Overall, the delayed revascularization observed with current dermal substitutes represents a major problem underlying scarring, contracture, and inability to grow with the patient.

Vascularization of the dermal substitute is a notable event during wound healing, because it confirms successful graft integration, facilitates the ability of the graft to grow with the patient, and is required before an epidermal component may be added on top[19], [20], [191], [192]. When applying treating a full thickness wound, a mechanically stable dermal substitute is first placed in the wound. Most of these are acellular, and therefore do not contain blood vessels. As such, the skin substitute must be vascularized by the patient's body before an epidermal graft, which provides barrier function, can be placed on top. If the epidermal graft is placed before the dermal substitute is adequately vascularized, then it will not have access to nutrients and will necrose[4]. Furthermore, graft vascularization provides nutrients not only to the overlying epidermis, but also to the other infiltrating cells key for skin regeneration (i.e., fibroblasts, fibrocytes, and inflammatory cells). Graft vascularization is a key event that controls the overall procedure timing and the associated outcomes. All currently available skin substitutes are avascular[182]; therefore their revascularization relies on angiogenesis-related sprouting from the host's wound bed. Pre-clinical research in animals has shown that host-mediated vascularization of avascular grafts depends on physical characteristics of the graft[13]. Specifically, graft revascularization by the host is impeded if the skin substitute employs an ECM that is either dense (decellularized skin) or highly crosslinked (i.e., Integra)[182]. Overall, the current procedure for applying skin substitutes is lengthy, requiring multiple steps, and results in poor take rates (<50%), scarring and contracture, and growth limitations[6]–[9]. The ideal acellular engineered skin substitute should contain ECM components associated with rapid

vascularization to facilitate rapid restoration of normal skin functions (i.e., barrier function, thermoregulation, ability to grow)[10], [11].

Our previous work has implemented type I collagen oligomers and demonstrated its ability to facilitate rapid vascularization *in vitro*. Unlike monomeric collagens (telo- and atelo-collagen variants), oligomer collagen contains a naturally occurring intermolecular crosslink that facilitates branching of the collagen matrix[25]. These higher-level interconnections present within oligomer collagen matrices serve as the basis for its superiority over commercially available collagens regarding mechanical integrity, polymerization rates, and reproducibility. However, previous work has implemented oligomers at subphysiologic densities (<<40 mg/mL collagen content), which does not contain adequate mechanical properties to prevent wound contraction *in vivo*.

To overcome the limitations of less-dense ECMs, our lab has previously generated dense, mechanically stable tissue constructs using a confined compression technique[28], [29]. This densification technique offered a microenvironment where cells have remained viable and have responded to local matrix mechanophysical cues by displaying altered morphology, cytomechanics, phenotype, and tissue morphogenesis. In the present work, we report the use of these densified oligomer tissue constructs for the treatment of full thickness defects within a rat model. Within our model, we created bi-lateral, full-thickness excisional wounds (including the panniculus carnosus) on the dorsum of Sprague-Dawley rats. In the present work, the rat full-thickness excisional wound model (in lieu of a Fusenig's chamber) was used to define the role of collagen fibril density on wound contraction as well as various wound healing events such as inflammation, recellularization, and revascularization. Engineering the relevant design parameters associated with densified oligomer tissue constructs may further the development of skin substitutes for a variety of wound types by controlling the rate and extent of associated wound healing events.

5.3 Materials and Methods

5.3.1 Fabrication of Compression Device for High-Throughput Compression

The medium-throughput compression device consisted of a custom-fabricated Compression Head with polyethylene platens and a standard 24-well culture plate. (Figure 5.1). The compression head was designed in SolidWorks (Dassault Systémes SolidWorks Corporation, Waltham, MA) and 3D printed using a 3D Printer (FORTUS 400mc, Stratasys). All 3D printed parts were cleaned as instructed according to manufacturer specifications prior to use. Fabrication of the polyethylene foams started with a 0.25" thick sheet of ultra-high molecular weight polyethylene (PE) foam containing 50 micron pores (BB2062-50BL, Scientific Commodities Inc.). From these sheets, cylindrical PE foams (15 mm diameter) were cut out. Holes (5/16") were drilled out of the center of these PE foams, which allowed press-fit placement of the PE foams onto the 3D printed compressor device. The compression head was exposed to H_2O_2 gas plasma for 30 minutes. Afterwards, the PE foams were rinsed with sterile PBS to remove any residual H_2O_2.

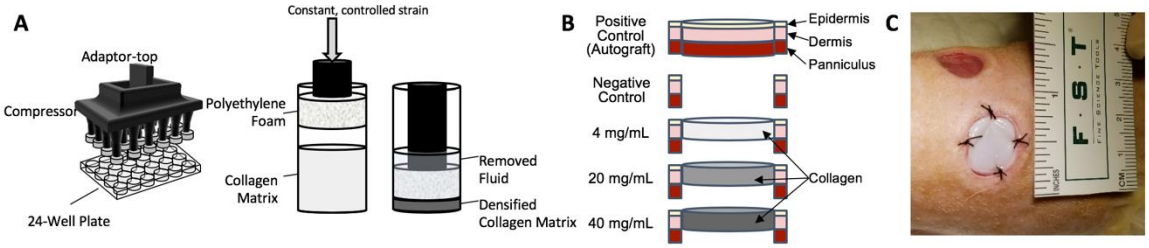

Figure 5.1 (A) Schematic of the high throughput compression device. The compressor was attached to a Test Resources mechanical testing device. Collagen matrices were polymerized in the wells of the 24 well plate. Using controlled strain, tissue constructs were compressed, and fluid was removed in a controlled manner through the porous polyethylene foam. To create tissue constructs with varying densities, wells were filled with different initial volumes of collagen. (B) Schematic showing the various groups tested throughout the study. Full thickness wounds (including removal of the panniculus carnosus) were created using a biopsy punch. Wound space was filled with the specified treatment groups. (C) Overhead photograph of showing a 40 mg/mL collagen tissue construct sutured into the wound

5.3.2 Preparation of Type I Collagen Oligomers

Type I collagen oligomers were acid-solubilized from the dermis of market weight pigs and lyophilized for storage as described in a previous study[39]. The oligomer

formulation was standardized based upon molecular composition as well as polymerization capacity according to ASTM International standard F3089-14[85]. Here, polymerization capacity is defined by matrix shear storage modulus (G', Pa) as a function of oligomer concentration of the polymerization reaction. All collagen solutions were diluted with 0.01 N HCl to achieve desired concentrations and neutralized with 10× PBS and 0.1 N NaOH to achieve pH 7.4[86]. Neutralized solutions were kept on ice prior to inducing polymerization by warming to 37°C.

5.3.3 Fabrication of Medium-Throughput Compression Device for Dermal Tissue Manufacturing

Tissue manufacturing was performed using a medium-throughput compression device integrated with a universal mechanical testing instrument (Testresources, Shakopee, MN). The compression device consisted of a custom-fabricated compression head with polyethylene (PE) foam platens and a standard 24-well culture plate (Figure 5.1). The compression head was designed in SolidWorks (Dassault Systémes SolidWorks Corporation, Waltham, MA) and fabricated from ABS-M30 using a 3D Printer (FORTUS 400mc, Stratasys). All 3D printed parts were cleaned as instructed according to manufacturer specifications prior to use. Circular platens (10 mm diameter; 0.25" thickness) were cut from ultra-high molecular weight PE foam with 50 μm pores (BB2062-50BL,Scientific Commodities Inc.). Circular indentations (5/16" diameter) were made in the center of the platens, allowing press-fit placement onto the ends of the compression head. The assembled compression head was gas plasma sterilized and the PE foam platens were rinsed in sterile PBS prior to tissue manufacturing.

5.3.4 Preparation of Dermal Substitutes with Varied Fibril Densities

Dermal substitutes (1.2 mm thickness) were prepared at specified oligomer concentrations, with oligomer concentration correlating with fibril density of the self-assembled construct[28], [29]. For 4 mg/mL, 20 mg/mL, and 40 mg/mL constructs, neutralized oligomer solutions (4.0 mg/mL) were pipetted into a 24 well-plate at volumes of 230 μL, 1150 μL, and 2300 μL, respectively, and polymerized for 30 minutes at 37°C. The 4 mg/mL material (230 μL volume, 1.2 mm height) was applied with no further processing. The multi-throughput compression device was used to compress wells

containing 1150 µL and 2300 µL volumes at a strain rate of 1.5 mm/min strain rate to a final thickness of 1.2 mm, yielding 20 mg/mL and 40 mg/mL constructs, respectively. All constructs were stored in sterile PBS prior to use.

5.3.5 Cryogenic Scanning Electron Microscopy

Ultrastructure and microstructure analysis of oligomer dermal substitutes and Helicote was performed using an FEI NOVA nanoSEM 200 (FEI, Hillsboro, OR). Samples were flash-frozen by submersion into critical point liquid nitrogen. Afterwards, samples were transferred to a CD1000 cold-stage attachment (Oxford Instruments North America, Inc., Concord, MA), and sublimated under vacuum for 10 minutes. Samples were subsequently sputter coated with platinum and imaged.

5.3.6 Creation of Full-Thickness Skin Wounds and Application of Dermal Substitutes

All animal studies were conducted according to protocols approved by the Purdue University Institutional Animal Care and Use Committee. Male Sprague-Dawley rats, (9 to 11 weeks of age; Charles River Laboratories, Wilmington, MA), were anesthetized using isoflurane gas. A sterile punch (15 mm diameter) was used to create a total of two full-thickness skin wounds, including the panniculus carnosus, bilaterally positioned on each side of the sagittal plane of the rat dorsum. Wounds were randomly assigned to experimental treatment and control groups (n=10), with experimental treatment groups consisting of either Helicote or oligomer constructs prepared at 4.0 mg/mL, 20 mg/mL, or 40 mg/mL. For a subset of animals, the excised full-thickness skin was applied to the opposite wound, serving as an autograft (positive control). No-fill wounds served as negative controls. Samples with sufficient suture retention strength, specifically the autograft, 20 mg/mL oligomer and 40 mg/mL oligomer, were sutured into place with non-absorbable 5-0 silk sutures (Perma-Hand Silk, Ethicon, Somerville, NJ). All wounds were covered with Xeroform™ (Covidien, Dublin, Ireland), a non-adherent pad (McKesson, San Francisco, CA), and Tegaderm (3M, St. Paul, MN). For additional support, the rats were wrapped with self-adherent cohesive bandages (Vetwrap) and zonas tape. Dressing changes were performed at 7 days. Photographs were taken with a ruler in the field of view at 0, 7, and 14 days. At 7 and 14 day study endpoints, animals were euthanized and wound

areas and associated implants were excised *in toto* and processed for histopathological analysis. Wound areas were quantified using a Matlab script and normalized to original wound areas. Autografts that did not successfully take, as determined by tissue necrosis, were not included for analysis. Additionally, tissue constructs that desiccated were also not included.

5.3.7 Histopathological Analysis

After euthanizing animals, grafts were excised and fixed in 4% paraformaldehyde for at least 24 hours, then transferred to 30% sucrose at 4°C. The samples were either i.) bisected and placed in optimal cutting temperature (OCT) medium overnight at -80°C for cryosection preparation or ii.) embedded in paraffin. Cryosections (30μm thickness) were prepared on a Thermo Cryotome FE (Fisher Scientific, Kalamazoo, MI). Paraffin sections were stained with hematoxylin and eosin (H&E) and Masson's Trichrome for histopathological analysis. Cryosections were rehydrated, permeabilized with 1% Triton X-100, blocked with 1% bovine serum albumin, and stained with the primary antibody, Goat anti-CD31(AF3628SP, R&D Systems). Slides were imaged on an upright microscope (Eclipse E200, Nikon, Melville, NY) using a Leica DFC480 camera (Leica, Buffalo Groove, IL).

5.3.8 Statistical Analysis

Statistical analyses were performed using statistical analysis software (SAS, Cary, NC). Unless otherwise stated, comparisons were made using one-way analysis of variance (ANOVA) with a Tukey posthoc test. A critical global p-value of 0.05 was used.

5.4 Results and Discussion

5.4.1 Plastic Compression Formed Graded Microstructure in Oligomer Dermal Substitutes Similar to Rat Dermis

Previously, plastic compression, where both strain levels and strain rates were specified, has been applied to self-assembled oligomer constructs as a means to expand the achievable range of fibril densities and control the resulting microstructure[28], [29]. Here, this work was extended with the development and application of a medium-throughput

compression device for manufacturing up to twenty-four dermal substitutes at once. All oligomer dermal substitutes were prepared at a final thickness of 1.2 mm, which falls within the known range for rat skin[193]. Cryo-SEM imaging was used to visualize and compare the ultra- and micro-structure of the dermal substitutes with that of normal rat skin.

Plastically compressed oligomer constructs prepared at 20 mg/mL and 40 mg/mL showed a graded collagen-fibril architecture similar to that observed in the dermal layer of rat skin (Figure 5.2). Local fibril bundling and alignment parallel to the surface was observed in upper regions, progressing to more randomly organized, lower fibril densities near the bottom. On the other hand, 4 mg/mL oligomer and Helicote displayed more homogenous (uniform) microstructures with distinguishing features. More specifically, 4 mg/mL oligomer appeared as a continuous network of collagen fibrils, which were approximately 100 nm in diameter. By contrast, Helicote appeared as an amorphous collagen sponge material defined by loose aggregation of non-dissociated tissue particulate and their associated native fibrillar collagen (Supplemental Figure 8). Collectively, results show that interfacing self-assembling (fibril forming) collagens with advanced tissue fabrication techniques supports customization of fibril density and approximation of native dermal architecture features, which may prove useful in the design of next-generation regenerative skin substitutes.

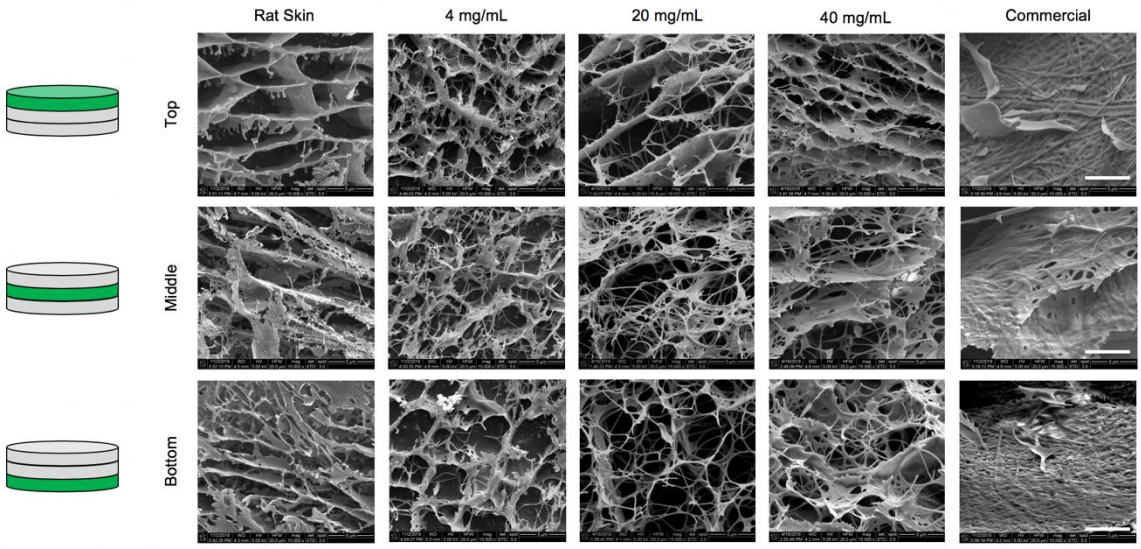

Figure 5.2 Plastic compression of oligomer supports creation of dermal substitutes with graded microstructures similar to native rat skin. Cryo-SEM images along the thickness of native rat skin, oligomer dermal substitutes prepared at 4 mg/mL, 20 mg/mL, and 40 mg/mL, and Helicote. Scale bar = 5μm

One important finding from the SEM images was the similarity of appearance between the native rat skin and the compressed collagen constructs. Many studies have shown that cells are able to sense the biophysical properties of the ECM. Specifically, cells sense not only the mechanical rigidity, but also the ECM microstructure and respond with changes in phenotype[38], [54], [100], [194]. As such, the ability to engineer tissue constructs with a similar microstructure to native skin is important for guiding the behavior of migrating cells to a regenerative response rather than one which will prolong inflammation or nonhealing[195], [196]. Although these plastically compressed tissue constructs were dense, they contained large enough pores to facilitate cellular infiltration. Moreover, their composition of purified type I collagen provides motifs that facilitates cellular interaction and remodeling of the matrix as needed. Oligomer collagens are self-assembling collagen molecules and are different from collagen sponges (i.e., Integra, Helicote), which consist of cross-linked tissue particulate. The cross-linking has been shown to mask critical cell-binding sites, which have resulted in poor host responses[197], [198]. Additionally, their structure consists of aggregated tissue particulate, which does not mimic native tissue architecture (Supplemental Figure 8).

5.4.2 Densified Oligomer Tissue Constructs Appeared Skin-like 14 Days Post-Operation

Representative images of each treatment group can be seen in Figure 5.3A. At 7 days, no discoloration was seen in the plastically compressed collagen tissue constructs, while the 4 mg/mL tissue constructs have darkened. In comparison, the positive control appeared moist and hydrated, while the negative control wound had scabbed over. At 14 days, the plastically compressed collagen tissue constructs as well as the positive control seemed to match the surrounding native rat skin. The gross images presented in Figure 5.3A show the persistence of the densified collagen tissue constructs (20 and 40 mg/mL) at 14 days post-operation. The 4 mg/mL group appeared desiccated or degraded and was no longer visible. Underneath the 4 mg/mL tissue construct, the wound appeared similar to the negative control (data not shown). Both of these groups contracted significantly, leaving behind elongated scars that were aligned along the sagittal plane of the rat's back. No samples of the Helicote group were able to maintain integrity within the wound at 14 days. In addition to resisting wound contraction, the densified collagen matrices resisted proteolytic degradation as demonstrated by their persistence at 14 days

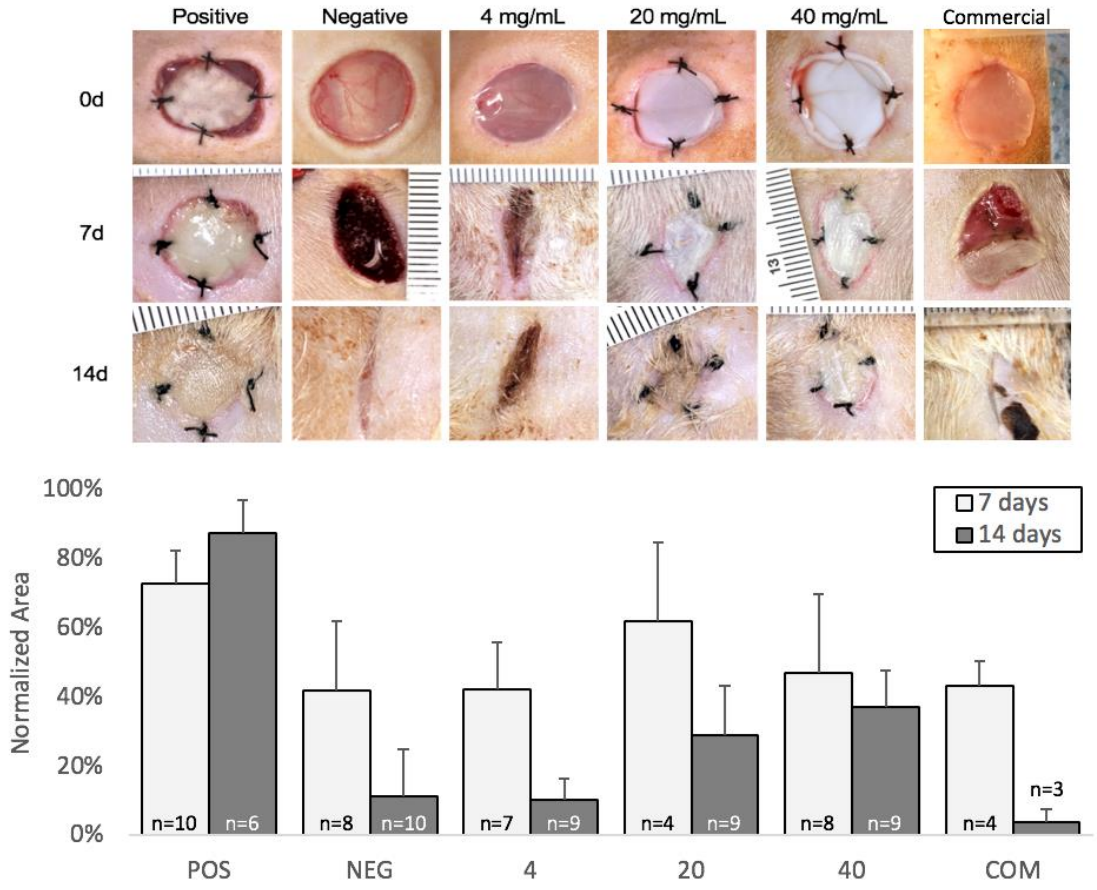

Figure 5.3 The 20 mg/mL and 40 mg/mL groups resisted wound contraction at 14 days. (A) Representative gross images of wounds taken at 0, 7, and 14 days. At 7 days, the 4 mg/mL group has contracted significantly more than the 20 mg/mL and 40 mg/mL groups. This trend continues at 14 days; the 4 mg/mL group nears complete closure while the 20 mg/mL and 40 mg/mL groups continue to resist complete contraction. (B) Bar graph showing measured wound sizes for each group at 7 days and 14 days. The wound sizes are represented by an area normalized to the starting wound size.

5.4.3 Densified Collagen Tissue Constructs Resisted Tissue Contraction and Proteolytic Degradation

One of the major criteria when choosing a biomaterial was employ a mechanically stable material to reduce tissue contraction without implementing a Fusenig's chamber. In the present work, images were taken at the time of operation and after each terminal time point (7 days or 14 days). Each treatment group was normalized to the initial wound size for the respective wound. At 7 days, the positive control contracted to 72.82% ± 9.49%, which was not statistically different to its size at 14 days (87.58%± 9.48%). The increased

area from 7 to 14 days for the positive control was likely due to the exclusion criteria we enforced on the samples. Specifically, we did not include autografts that did not take by 14 days, some of which had smaller wound areas. Interestingly, the size of the positive control at 7 days was also not statistically different from the 20 mg/mL tissues at 7 days (62.02% ± 22.60%) but was statistically different from all other groups. When comparing the normalized wound areas at 14 days, there appears to be a trend of increased resistance to contraction as collagen fibril density was increased (10.18% vs. 28.89% vs. 37.24% for 4 mg/mL, 20 mg/mL, and 40 mg/mL, respectively). Furthermore, the 20 mg/mL and 40 mg/mL tissue constructs were statistically different from the all other groups at 14 days. Two-sample t-tests were performed to compare each treatment at 7 days and 14 days. Here, the autograft, no treatment, 4 mg/mL, and Helicote demonstrated statistically different measurements, while the densified oligomers (20 mg/mL and 40 mg/mL) were not statistically different. This demonstrated that the 20 mg/mL and 40 mg/mL tissue constructs resisted contraction between 7 and 14 days greater than the other groups. Their ability to resist contraction was likely due to the increased compressive modulus observed when collagen fibril density is increased[28], [171].

Generally speaking, the rodent animal model offers a quick, relatively cost-effective method for testing wound therapies; however, additional modifications to these animal models have been performed to help with wound contraction. The primary mode of wound closure within rodents is through contraction via a subdermal muscle, the *panniculus carnosus*. To prevent wound contraction, other groups did not remove this muscle in their full-thickness defects and/or a Fusenig's chamber was implemented[43], [48], [49], [199]. This chamber is a ring made from rigid material (i.e., polypropylene, steel) that is sutured into the tissue surrounding the wound. While this chamber has enabled application of less-dense tissue matrices in wound healing in rodents, the results are not within a model that accurately represents the clinical problem. In the present work, we did not implement a Fusenig's chamber and demonstrated that the densified oligomer collagens could resist wound contraction in lieu of a Fusenig's chamber.

5.4.4 Oligomer Collagen Groups were Integrated into the Surrounding Native Tissue

Masson's Trichrome staining was performed on the tissue explant to qualitatively examine collagen tissue constructs (Figure 5.4). Here, collagen appeared blue, while cell nuclei appeared purple and cytoplasm appeared pink. At 7 days, the collagen in the autografts stained a deep blue hue due to the high collagen fibril density found in native tissues (~40 mg/mL collagen content). On the other hand, the negative control presented very light staining within the wound region. As for the oligomer tissue constructs, an increase in collagen density was evident by the increasingly deeper blue color. As for the Helicote, it stained a deep blue similar to that of the autograft; however, its overall appearance was patchy and discontinuous. When looking at the color of the autograft at 14 days, it appeared lighter blue in color when compared to native skin. This was likely due to degradation via invading inflammatory cells. All of the other treatment groups appeared darker than their 7 day counterpart. Within the oligomer tissues, the difference between each group was more drastic at 14 days than at 7 days.

The boundary of the treatment and the native skin can be seen in the 40× images by the sudden change in color (Figure 5.4; yellow dotted lines). When looking at the boundary of the grafted tissues at 7 days, the autograft did not appear to have integrated to the native tissue as indicated by the white gap. All other groups appear to have integrated with the tissue with the exception of the Helicote, which contains some gaps as well. For the oligomer tissue groups, there appeared to be smooth integration with the surrounding native skin. At 14 days, all of the grafted tissues appear to have integrated to a higher degree than at 7 days. The autograft no longer has the gap present; instead, there appeared to be a highly cellularized tissue interface. Going from the negative control to the 40 mg/mL tissue construct, there appeared to be increasing integration as the oligomer collagen density increased. At lower collagen concentrations, the borders were clearly distinguishable by the sudden change in color. As collagen concentration was increased, the interfaces smoothly blended into one another and became increasingly difficult to identify. As for the Helicote, the boundary was similar to the negative controls, since the majority of the substitute had fallen out of the wound.

5.4.5 Timing and Extent of Inflammatory Response Depended on Collagen Fibril Density

For the autograft, minimal cellular infiltration was observed at 7 days (Figure 5.4). However, at 14 days, there appeared to be a band of inflammatory infiltrate migrating to the surface of the tissue. The negative control contained a dense infiltration of cells at 7 days, continuing until 14 days. Similarly, the 4 mg/mL group contained a dense infiltration of cells at both 7 and 14 days. When looking at the 20 and 40 mg/mL group, we observed a collagen fibril density-dependent infiltration into the tissue grafts. At 7 days, the 20 mg/mL group contained cellular infiltrate up to the surface of the tissue, leaving only a very thin band of acellular collagen. In contrast, the denser, 40 mg/mL collagen tissue group had a much thicker acellular band. Conversely, at 14 days, the 20 mg/mL group appeared to have less cell infiltration near the surface, while the 40 mg/mL group had the densest collection of inflammatory infiltrate at the surface. Lastly, the commercial collagen (Helicote) appeared loose and patchy with very few cells migrating through this group at 7 days. At 14 days, most of the Helicote had fallen out of the wound, but remnants could be seen as demonstrated by the characteristic porous pattern of the material. The remaining wound appeared contracted and resembled the 4 mg/mL and negative control groups.

The inflammatory response is the second major part of wound healing and has been identified as a major determinant for scar tissue formation[200]. The inflammation seen in our model was inevitable due to the wounding to the rat dermis and subsequent release of cytokines and damage-associated molecular patterns (DAMPs). Inflammation is crucial for clearing the wound area for repair; however, its persistence can result in pathologies such as chronic non-healing wounds. The patterns of inflammatory infiltrate observed in the oligomer collagen follow a collagen density-dependent trend. Increasing collagen fibril density slowed down the infiltrating cells by increasing the material that they must degrade and migrate through. As such, the 40 mg/mL group became visibly infiltrated to the surface at 14 days, while that same level of invasion was nearly achieved in the 20 mg/mL group at 7 days, and much sooner in the 4 mg/mL group. By the time that the inflammatory cells within the 40 mg/mL group have invaded to its surface (14 days), the 20 mg/mL group already appeared to contain less inflammatory cells near the surface, indicating that the inflammation was resolving. Further study using longer time points is needed to determine

the long-term outcomes of early and late inflammatory responses. Quick turnover of the inflammatory phase is ideal, since chronic inflammation is pathologic and has been shown to result in scar tissue formation[201].

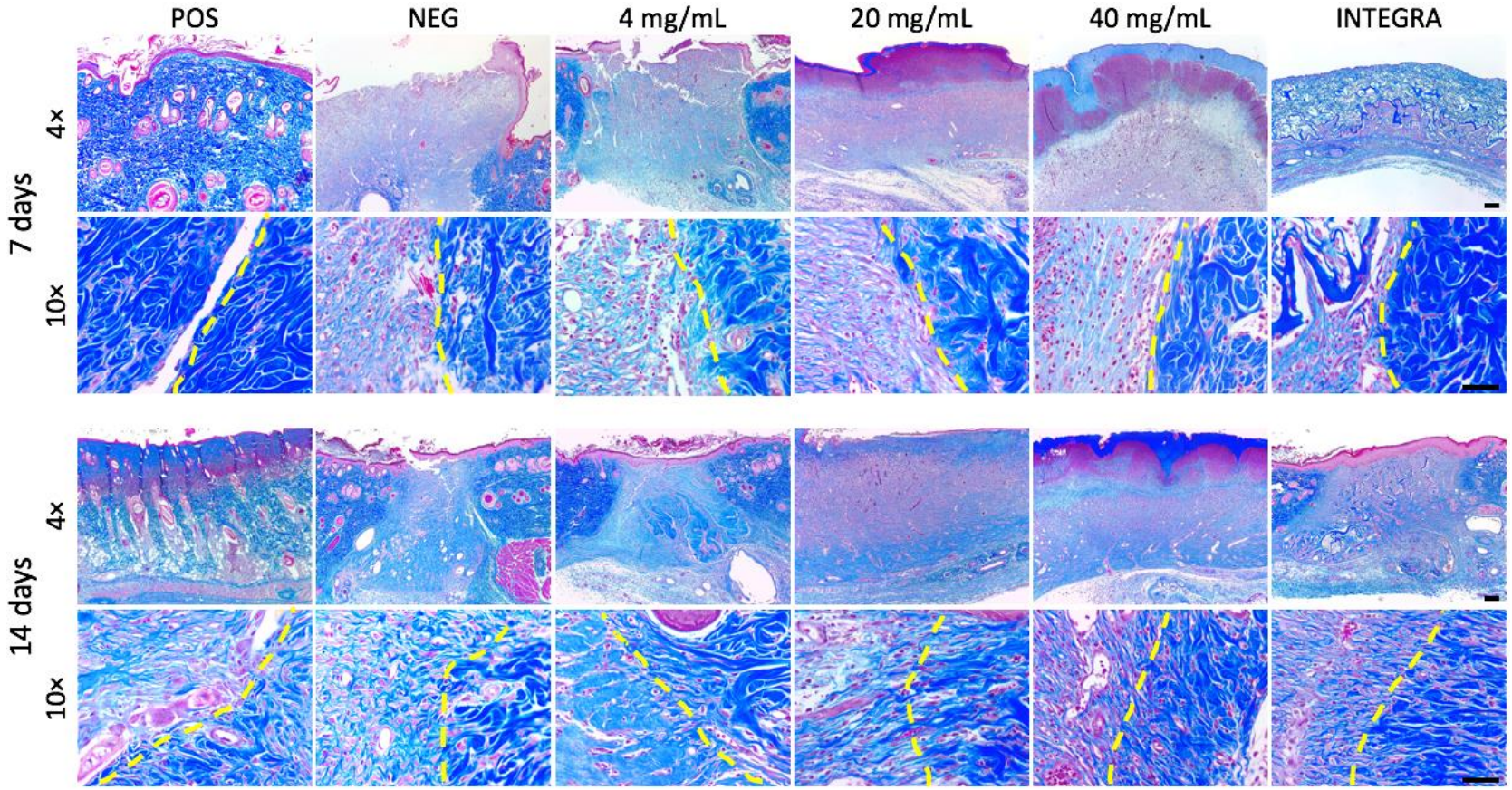

Figure 5.4 Within the oligomer collagen groups, the rate of cell infiltration appeared to decrease with increasing collagen fibril concentration. Over the duration of the 14 days, all oligomer tissues persisted in the wound and were infiltrated by the host's cells. Representative histological images (Masson's Trichrome) of each treatment group at 7 and 14 days showing the center of the treatment (4× images) and the boundary (40× images, yellow dashed line). Regarding the boundary images, on the right was the native rat dermis. Scale bar: 200μm.

5.4.6 Cellular Populations were Impacted by Scaffold Composition and Density

Higher magnification (100x) images helped delineate the individual cells within each group (Figure 5.5). The positive control autograft had sparse infiltrate at 7 days, likely due to the inherently high collagen density. At 14 days, there was an inflammatory population present and evidence of some coagulative necrosis, though new vessels have appeared to have restarted perfusion. The negative control sample showed a large cellular infiltrate including many small rounded cells, likely lymphocytes, multi-lobulated granulocytes, and fibroblastic cells. At 14 days, more vessels and surrounding matrix were apparent while the immune response had begun to regress. The 4 mg/mL sample was similar, with an early mixed infiltrate. The 20 mg/mL sample had a stratified appearance with a dense neutrophilic population near the surface and lower areas with lymphocytes, monocytes, and fibroblasts. However, inflammation resolved rapidly, and vessels were quite apparent at 14 days. The dense collagen in the 40 mg/mL sample limited cellular infiltration more than the 20 mg/mL, but less than the autograft. More neutrophils and other granulocytes were apparent in the dense collagen near the surface. Cells continued to penetrate at 14 days, with the 40 mg/mL sample appearing more like the 20 mg/mL at the previous 7 day time point. The Helicote had a distinctive porous appearance. There was minimal cellular ingrowth at 7 days, though blood and a mixed inflammatory population were seen including many eosinophils. At 14 days, new matrix had appeared around the Helicote along with more fibroblasts and inflammatory cells. Foreign body giant cells were seen in some areas. In summary, higher collagen densities as in the 40 mg/mL sample and positive control were again associated with longer periods of inflammation. The 20 mg/mL sample underwent resolution rapidly in contrast. The commercial product had a distinctive foreign body response in contrast to the oligomer samples, which displayed a similar response to positive control wounds.

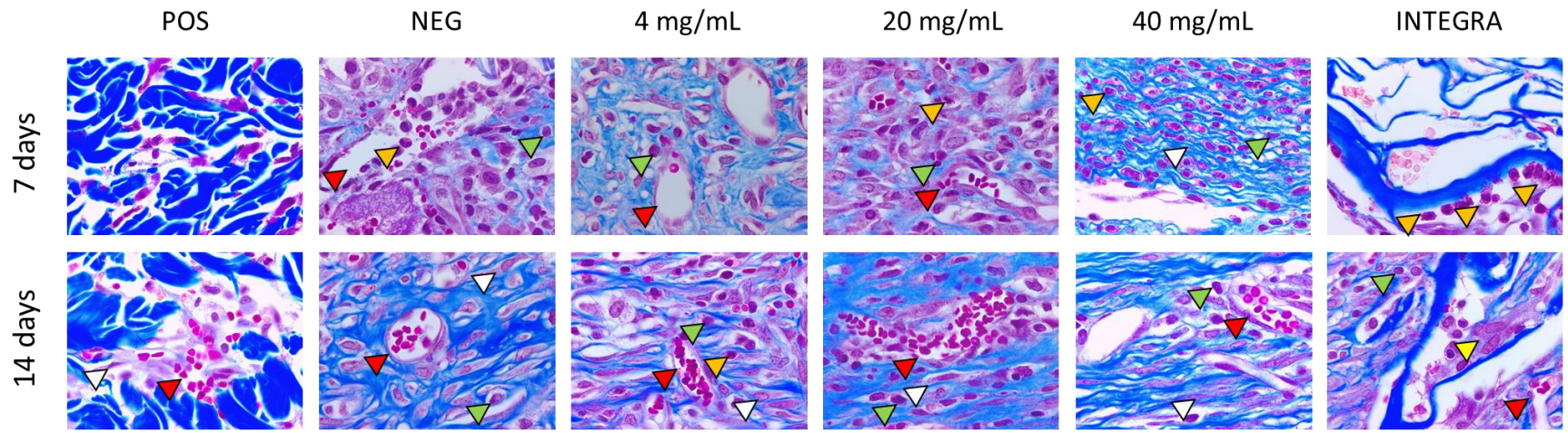

Figure 5.5 High magnification images of cellular infiltration (Masson's trichrome, 100x) showed a progression of inflammation and revascularization in all samples. Notably, high collagen density in the positive control and 40 mg/mL samples had decreased infiltrate, though more neutrophils were present. Other experimental groups showed lymphocytes, fibroblasts, and new vessels forming. The commercial comparison shows granulocytes lining the material, along with beginnings of a foreign body giant cell response. Green: lymphocytes, red: vessels, orange: granulocytes, yellow: giant cell, white: fibroblast.

5.4.8 Timing and Extent of Tissue Vascularization Depends on Collagen Fibril Density

Tissue vascularization followed a similar pattern to the cellular infiltrate: extent and depth of vascularization depended on collagen fibril density. The vascularization of each tissue group was visualized via confocal microscopy (Figure 5.6). Here, the vascularization observations seen in the histology images was further corroborated with high-definition, high signal-to-noise images.

At 7 days, the autografts appeared to have positive CD-31 staining around the follicles, which are known to be vascularized[202]. The negative control and 4 mg/mL groups contained vascularization all the way up to the surface of the wounded area. Within the 20 mg/mL and 40 mg/mL groups, vascularization could be seen near the edge of the tissue construct, with deeper penetration observed in the 20 mg/mL tissue constructs. Regarding their morphology, the vessels in the 20 mg/mL and 40 mg/mL tissue constructs looked less developed than those found in the 4 mg/mL tissue construct as determined by their lighter staining. From 7 days to 14 days, the vascularization in the negative control and 4 mg/mL tissue group appeared to have reduced. As for the 20 mg/mL and 40 mg/mL groups, there appeared to be increased depth of invasion from 7 days, with the 20 mg/mL experiencing deeper vascular invasion. As mentioned previously, graft characteristics affects graft revascularization. Here, the denser tissue (40 mg/mL) demonstrated delayed revascularization related to ECM-density related inhibition. Regarding morphology at 14 days, the vessels appeared larger in all of the oligomer collagen groups.

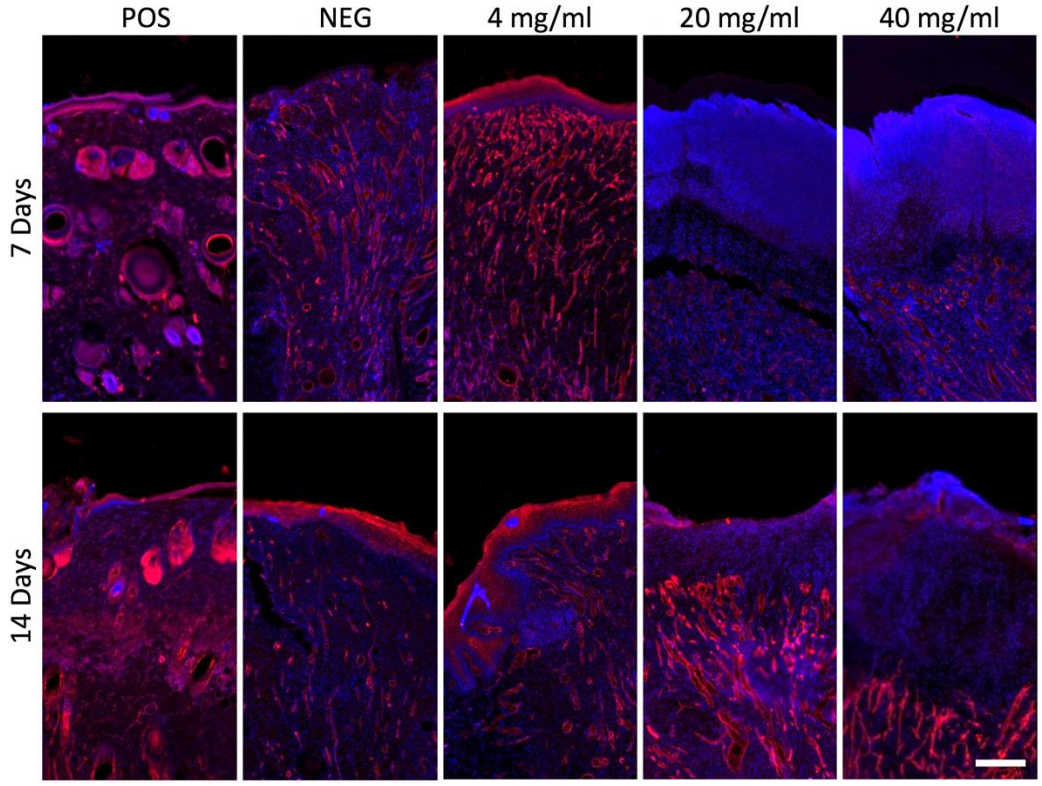

Figure 5.6 As collagen concentration increases, there was decreased invasion of vessels. Vessels appeared to subside within the 4 mg/mL at 14 days, while the 20 and 40 mg/mL group contained persisting vessels. Confocal microscope images of each treatment group at 7 and 14 days. To visualize blood vessels, excised tissues were stained with a CD31 primary antibody (red) and DAPI (blue). At 7 days, the 4 mg/mL group appears highly vascularized up to the surface of the tissue construct. Alternately, there is less vascularization seen in the 20 and 40 mg/mL tissue constructs. At 14 days, a decrease in vascularization is observed in the 4 mg/mL group, while extensive vascularization is observed in 20 and 40 mg/mL. The extent of the observed vascularization appears to be collagen fibril density dependent. The 20 mg/mL group appears to have more microvessels near the surface, while the 40 mg/mL has microvessels near the tissue boundary. Scale bar = 200μm

When engineering a tissue construct as a skin substitute, it was important to consider the interactions that the biomaterial would have with the invading endothelial cells. Research has reported that, within a normal wound, angiogenic ingrowth was due to endothelial cells sensing and responding to the fibrin/fibronectin-rich wound clot. They further reported that, once collagen accumulated to produce a scar, blood vessels began to diminish — implying that type I collagen signaled an end to the vascularization phase[203]. However, in the present work, dense collagen tissue constructs were extensively

vascularized via angiogenic invasion. This was further corroborated by many vasculogenesis models that have successfully employed type I collagen to induce vessel formation[38], [52], [92]. Overall, the extensive vascularization observed in the densified oligomer tissue constructs provided evidence that the grafted tissues were integrating with the host.

As mentioned earlier, the observed vascularization patterns correlated with inflammation, which was partly due to these two processes being dependent on one another. When tissue injury to the skin occurs, VEGF is released[204], causing the nearest capillaries to vasodilate. In this instance, leukocytes are recruited to the vasodilated capillaries and begin extravasating through the vessel wall into the tissue space to reach the site of injury. Additionally, VEGF has been shown to increase endothelial cell interaction with circulating inflammatory cells. Specifically, VEGF has been found to increase leukocyte extravasation by affecting expression of leukocyte-endothelial cell adhesion molecules[195]. The leukocytes then seek and remove any bacteria or debris, clearing the area for new tissue growth. Additionally, vessels are important not only for the delivery of material to the wound site, but also for the removal of the waste products via lymphatic capillaries[195]. Lymphatic capillaries transport fluid, extravasated leukocytes, and antigen presenting cells from the wound area to the lymph system. Without lymphatic vessels to clear the fluid buildup, edema could occur, which has been demonstrated in Integra dermal regeneration template[205], [206]. Overall, the blood and lymphatic capillaries work together to regulate the inflammatory process.

Cellular infiltration, whether it be inflammatory, mesenchymal, or vascular, is crucial for effective tissue regeneration. The complex interplay between clearing debris (i.e., foreign objects, dead cells) and laying down new matrix in the wound site must be considered. In the present work, the rate of cellular infiltration into the tissue construct decreased with increasing collagen fibril density. Cells sense and respond not only to ECM density and microarchitecture, but also to ECM gradients[38], [207], [208]. SEM images revealed a graded microstructure in the densified collagen tissue constructs. The effect of the graded microstructure was observed with the variable rates of cellular infiltration in the 20 and 40 mg/mL tissue constructs. Additionally, this was observed in the varying thicknesses of the acellular region observed within the densified oligomers. Additionally,

the SEM revealed that all oligomer collagen matrices were porous enough to facilitate cellular infiltration, while the Helicote appeared sheet-like as it consisted of aggregates of tissue particulate. Cell infiltration into the Helicote appeared minimal and was consistent with previous reports of limited host response when collagen sponges are used [197], [198].

Collagen sponges represent a large portion of the market of dermal substitutes, however they undergo processing that limits the host's response. These sponges consist of tissue particulate that is exogenously crosslinked to enhance its mechanical properties and control degradation and inflammation. In the present study, the Helicote was not able to resist wound contraction 14 days post-operation, while both of the densified oligomers could resist wound contraction 14 days post-operation. Regarding cellular infiltration, there was much less infiltration in the Helicote than in the oligomer collagen matrices. This is likely due to the limited cellular adhesion observed in collagen sponges[209]. On the other hand, oligomer collagen retains natural cell-binding domains, enabling recognition by infiltrating cells. When looking at the population of infiltrating cells, the Helicote contained giant cells, which were not seen in other groups. One giant cell is the fusion of macrophages that are generated when a large foreign body has been detected. Additionally, minimal vascularization was observed in the Helicote, while all oligomer collagens demonstrated vascularization by the host. Overall, the oligomer collagen elicited a more-desirable wound healing response than Helicote.

It was found that oligomer collagen fibril density determined wound healing outcomes (i.e., wound contraction, inflammatory response, and vascularization). It was shown that increasing the collagen fibril density increased the graft's resistance to wound contraction; specifically, both of the densified oligomer tissue constructs successfully resisted wound contraction 14 days post-operation. Regarding inflammation, increasing the collagen fibril density not only decreased the rate of inflammatory infiltration, but also prolonged the inflammation phase. The 4 mg/mL tissue construct had the least amount of cell infiltrate at 7 days, while the 20 mg/mL and 40 mg/mL tissue constructs contained dense bands of inflammatory infiltrate. At 14 days, most of the inflammation has resolved in the 4 mg/mL tissue construct, which was paired with complete epithelialization. In the 20 mg/mL tissue construct, the inflammation appeared to have started resolving, while the 40 mg/mL tissue construct still contained a dense band of inflammatory cells. The

vascularization pattern of the oligomer tissue constructs was similar to the inflammatory pattern. Regarding early wound healing outcomes, the ideal oligomer tissue construct was the 20 mg/mL tissue construct. This tissue construct not only demonstrated adequate mechanical properties by resisting wound contraction, but also it demonstrated rapid turnover of the inflammatory phase, which is important for reducing scarring and contraction outcomes[183]. Future studies should be performed to analyze collagen fibril densities near 20 mg/mL to further optimize wound healing outcomes.

Further study of cell populations within the tissue explants should provide mechanistic insight for continuing to develop the densified collagen oligomer material. For example, examining the leukocyte population would provide valuable insight on the wound healing process; specifically, determining the relative amounts of M1 and M2 macrophages[210], [211]. M1 macrophages release pro-inflammatory cytokines and play a major role with removing microbes and debris, while M2 macrophages play a major role in rebuilding the wounded region. Regarding mesenchymal cells, it would be of great interest to define the phenotype of the invading fibroblasts. Ideally, minimal myofibroblast invasion is desired, as myofibroblasts are known to be a major contributor of wound contraction[212], [213]. In regard to the invading vessels, it would be helpful to observe the ratio between blood and lymphatic capillaries. This would provide additional information into the inflammatory timeline as lymphatic capillaries play a large role in removing the proinflammatory cells as well as the excess fluid to prevent edema. Overall, understanding the interplay of these cell invasion events will help inform future biomaterial designs for wound healing applications[214], [215].

5.5 Conclusion

Altogether, the developed animal model was used to define the role of collagen fibril density in excisional wound healing. A major finding was that the densified oligomer collagen resisted wound contraction and proteolytic degradation. Additionally, the graded microstructure between the 20 mg/mL and 40 mg/mL groups affected the rate of cellular infiltration into the tissue construct. The denser tissue constructs had delayed inflammatory infiltration and vascularization. Another significant finding was the thorough infiltration of the host's vasculature, which indicates that the graft successfully integrated with the

host. Collectively, these findings highlight the importance of densified oligomer tissue microstructure. The present work laid the foundation for future studies involving vascularized, dense tissue constructs by defining the rat's response to acellular dense tissue constructs.

CHAPTER 6. CONCLUSIONS

The work presented in this thesis demonstrated the development of a novel culture system and adapted a previously developed advanced tissue culture fabrication technique for studying *in vitro* tissue construct vascularization using oligomer collagen and endothelial colony forming cells (ECFCs); specifically, the multitissue interface culture model and densified oligomers. However, these advanced tissue fabrication techniques could be achieved solely due to the inherent mechanical stability of the oligomeric collagen. Oligomer collagen is an exceptional matrix for vasculogenesis, as well as all other tissue engineering applications, due to its intermolecular crosslink. The oligomer provides impressive mechanical support without excessive extracellular matrix (ECM) material, providing a relatively open microenvironment that allows cells to migrate through as well as interact with the ECM. The oligomer has been used previously to modulate early and late vessel forming events via cell-matrix interactions. In the present work, new tissue models were developed to address areas for clinical translation, such as rapid and extensive vascularization. The multitissue interface culture model was used to identify key parameters for rapid *in vitro* tissue vascularization: ECFC density, mechanical integrity (maintenance of cell-matrix tensional forces), and the presence of adipose stromal cells (ASCs). These key parameters were adapted to rapidly vascularize dense tissues (>10 mg/mL collagen content) *in vitro*, a feat that was not yet accomplished. Lastly, a rodent model was developed to evaluate the efficacy of acellular engineered tissues in full-thickness skin defects. Within this model, we employed densified oligomers, which demonstrated the ability to resist degradation and tissue contraction as well as facilitate rapid recellularization and vascularization. The next step for this project would be to graft the densified vascularized tissue constructs into this developed excisional rodent model and evaluate the role of vascularization on tissue construct integration, wound contraction, and scarring.

6.1 Future work

The vascularized dense tissues from Chapter 4 should be grafted into the animal model developed in Chapter 5 with slight modifications to test the efficacy of rapidly vascularized, dense tissue constructs' ability to anastamose to the host's circulation and affect wound healing outcomes (scarring/contracture). Since human ECFCs will be used, an immunocompromised rat variant should be used to prevent immune rejection of the xenogenic component of the grafted tissue construct. Alternatively, a procedure for harvesting rat ECFCs could be developed, but that would require additional testing and validation before implementing. Rather than using sutures to hold the densified oligomers in place, neutralized oligomer collagen could be used as a surgical glue, offering two advantages. First, the use of collagen rather than suture material will reduce the inflammatory response induced by the suture material. Secondly, the grafted tissue construct will be anchored on all sides, helping prevent cell-mediated tissue contraction of the highly cellularized dense tissue construct. As demonstrated in Chapter 4, we expect rapid vascularization of the dense tissue constructs. As such, it would be appropriate to graft the cellularized tissue constructs immediately after densification to quickly provide the encapsulated cells dynamic, *in vivo* stimuli to prevent ECFC regression. As for matrix density selection, it would be ideal to test the same three matrix densities as was used in Chapter 4 (12, 20, and 40 mg/mL). These three ECM densities provide different cell-matrix interaction stimuli, resulting in the ECFCs forming vessels at different rates. We expect the anastomosis rate to increase with decreasing collagen fibril density, since lower collagen fibril densities facilitate i.) increased rates of host cell infiltration as well as ii.) increased vessel formation within the tissue construct. Additionally, the extent of tissue contraction is expected to increase with decreasing collagen fibril density. The ECFC densities may also have to be modified when moving into the animal. In Chapter 4, tissue construct vessel volume percentage decreased from 3 days to 7 days likely due to regression. Any regression, or apoptosis, of cells in the tissue construct will elicit additional inflammatory response, which is not desired. The current densities will be used, since the dynamic environment of the wound could provide pro-survival stimuli for the ECs to prevent the regression that was observed *in vitro*. Although the capillary density estimated within skin is ~90-140 capillaries/mm^2, this represents the capillary density within normal

patients[216], [217]. It is likely that the wounded areas will require a higher-than-normal capillary density due to the metabolic needs of wounde tissue. Preliminary testing will need to be performed to evaluate optimal vessel densities of grafted tissue constructs. Overall, further investigation into vascularized oligomer tissue constructs will provide insight on critical design parameters related to regeneration of functional skin replacements for children suffering from large skin defects.

APPENDIX

Supplemental Figures

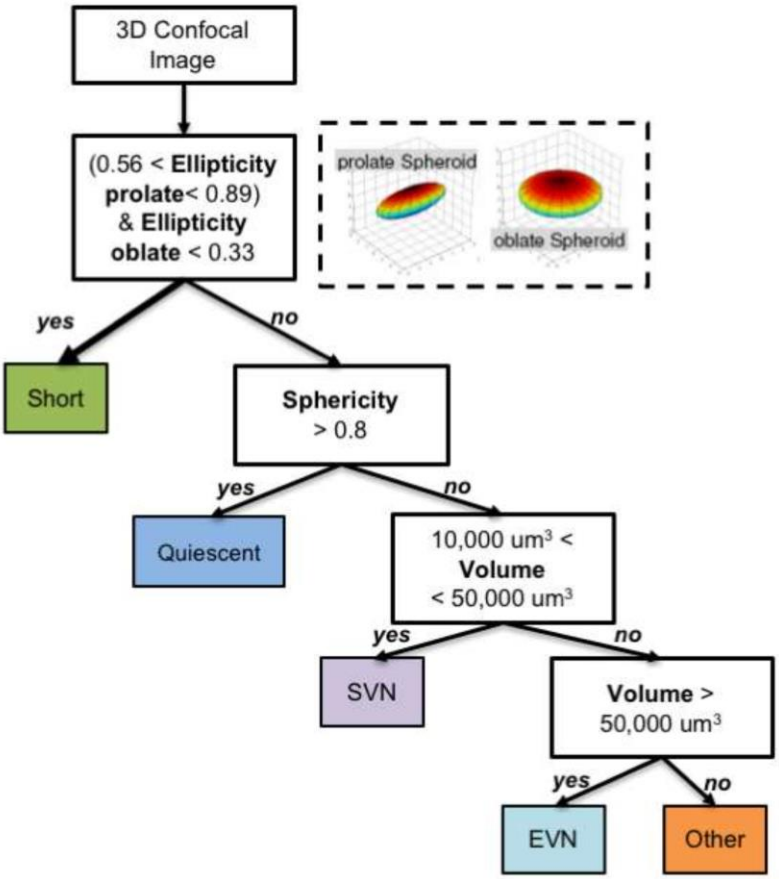

Supplemental Figure 1 Decision tree used to quantify vessel network morphology. Each surface object is categorized as either a quiescent cell, short vessel, small vessel network (SVN), extensive vessel network (EVN), or other. Any objects that could not be classified by the decision tree were categorized as "other".

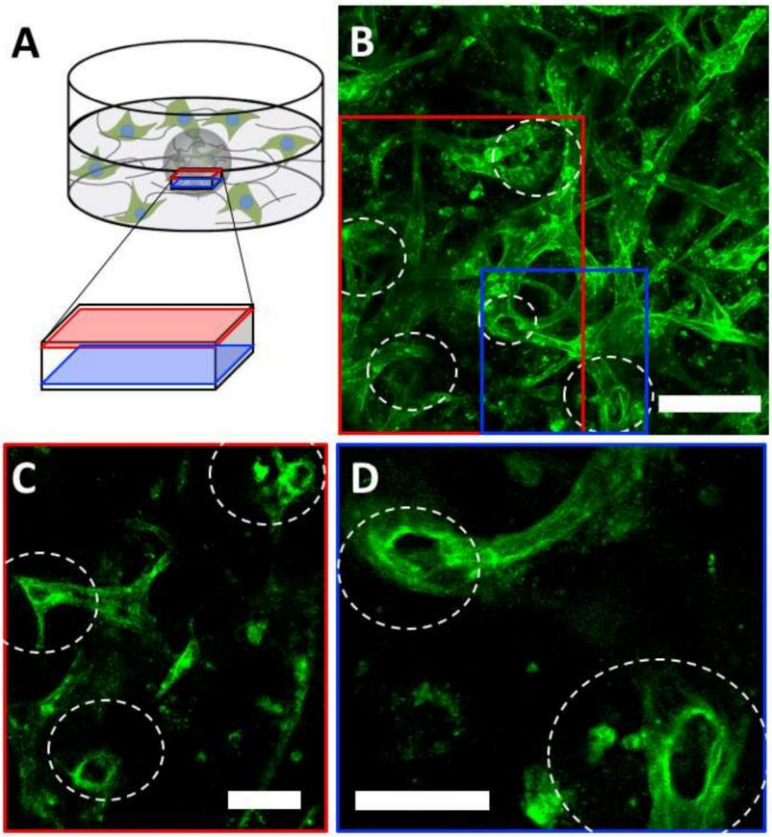

Supplemental Figure 2 Lumenized vessel networks formed within ECFC-encapsulated spheres of the multitissue culture format. (A) Schematic of the Z-stack imaging volume within the ECFC- oligomer sphere. (B) Projection of confocal image stacks (100 μm thick) illustrating vessel network formation within the tissue sphere for multitissue interface constructs after 3 days of culture. ECFC-encapsulated oligomer spheres (200 Pa, 5 × 106 ECFC/mL, 5μL) were embedded in oligomer matrices (200 Pa, 0.2 × 106 ASC/mL, 250 μL). Tissue constructs were stained with phalloidin (green fluorescence) for visualization of ECFC cytoskeleton. Red and blue boxes represent regions of interest with lumenized vessels (white dotted circles). (C,D) High- magnification, image slices within (C) upper and (D) lower regions of imaged volume showing lumenized vessels (white dotted circles). (B) Scale bar = 150 μm. (C, D) Scale bar = 80μm.

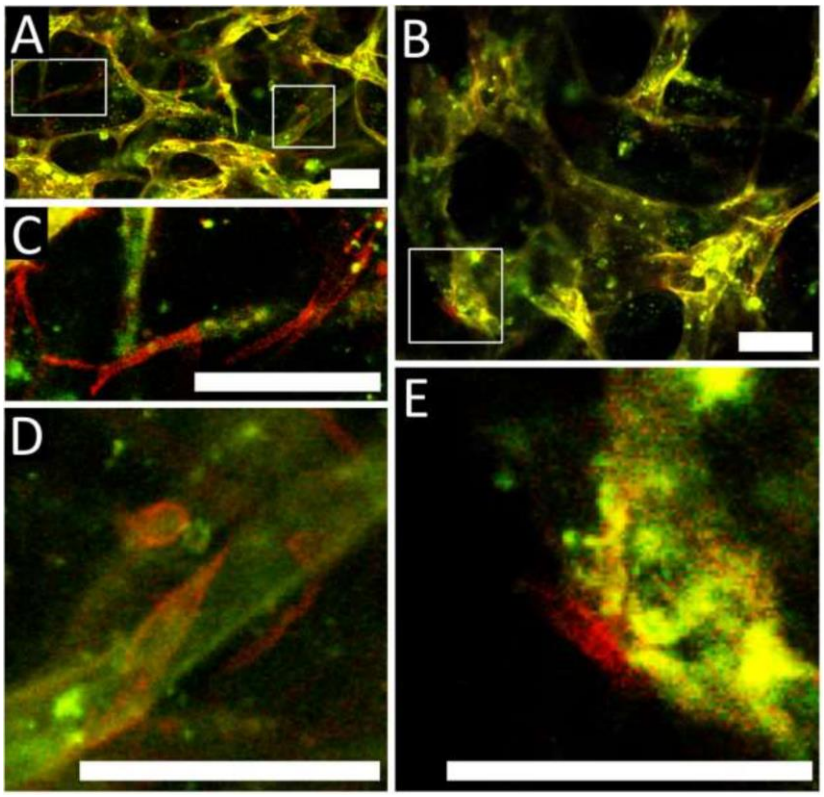

Supplemental Figure 3 Confocal images taken within the tissue sphere, illustrating ECFC-ASC interactions after 3 days of culture. (A, B) Regions of interest within confocal images. ECFC-encapsulated oligomer spheres (200 Pa, 5×106 ECFC/mL, 5μL) were embedded in oligomer matrices (200 Pa, 0.5×106 ASC/mL, 250 μL). Tissue constructs were stained with UEA1 lectin (green fluorescence) and phalloidin (red fluorescence) for visualization of ECFC vessel networks and F- actin of all cells, respectively. When the green and red fluorescence was overlaid, ECFC appeared yellow (red + green fluorescence) while ASC will only be stained by the phalloidin, appearing red. (C-E) High-magnification, image slices showing pericyte-like role of ASC on ECFC vessels. All scale bars = 80 μm.

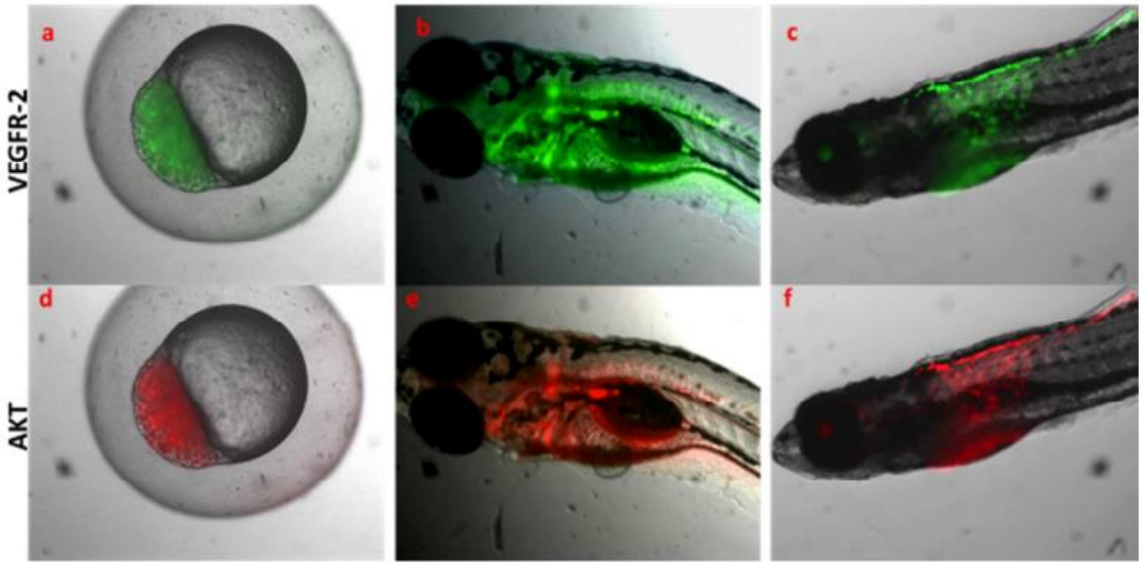

Supplemental Figure 4 Distribution of ASOR (bottom, red) and VSOR (top, green) 10 minutes after the sensor was microinjected into zebrafish at different stages of development. (A, D) 3-hour post fertilization (3hpf) embryo; (B, E) five days post fertilization (5dpf); and (C, F) seven days post fertilization (7dpf).

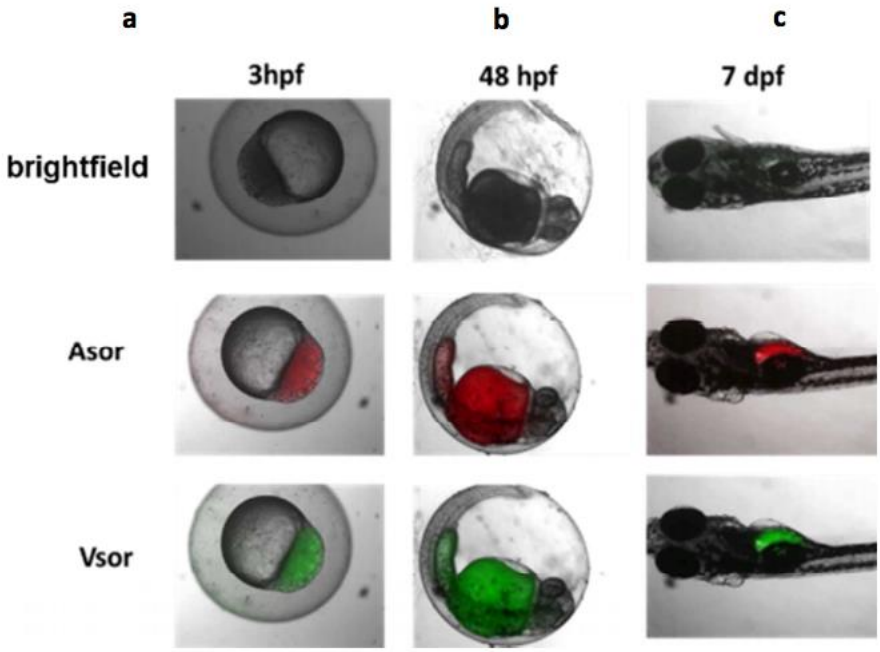

Supplemental Figure 5 Biocompatible evaluation in developing zebrafish after biosensor uptake. Biosensor was microinjected into (A) 3hpf embryo and returned into culture (Egg water, 27°C). Embryo was then imaged at (B) 48 hpf and (C) 7 dpf. All returned embryos (n=5) successfully developed into larvae and no changes in phenotype were observed compared to control.

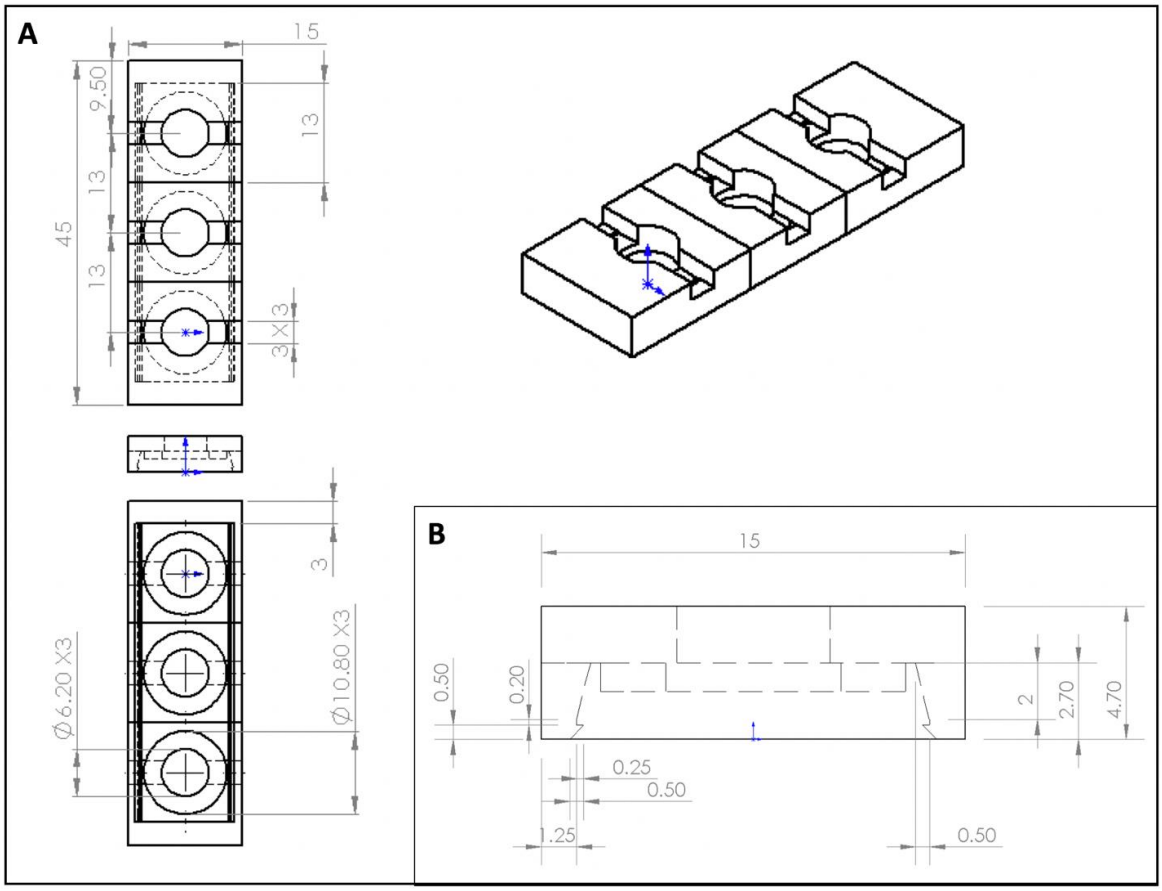

Supplemental Figure 6 SolidWorks drawing of the top part of the Tissue Tensioner. Units are in mm. (B) Zoomed-in view to show the dimensions of the press-fit locking mechanism.

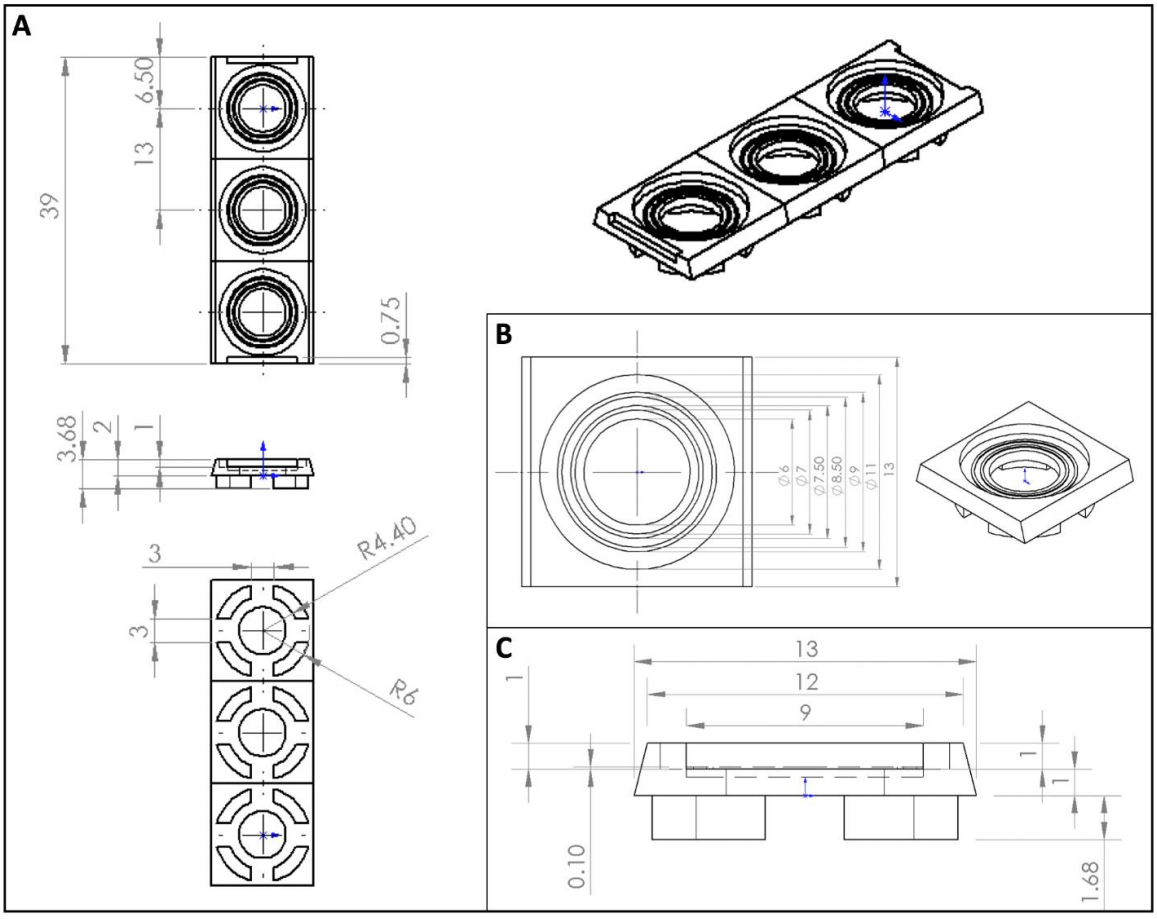

Supplemental Figure 7 SolidWorks drawing of the bottom part of the Tissue Tensioner. Units are in mm. (B) Zoomed-in image of the well where the tissue constructs are placed. (C) Zoomed-in image showing the dimensions of the press-fit locking mechanism.

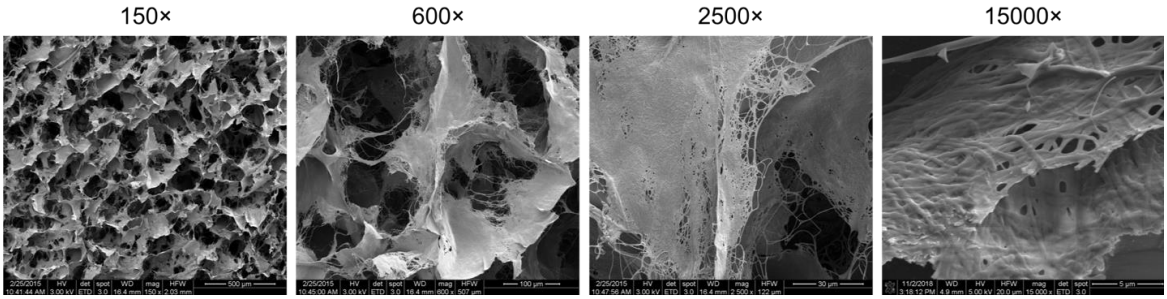

Supplemental Figure 8 Cryogenic SEM images of Helicote at 150×, 600×, 2500×, and 15000× magnification.

REFERENCES

[1] R. D. Mosteller, "Simplified calculation of body-surface area.," *N. Engl. J. Med.*, vol. 317, no. 17, p. 1098, 1987.

[2] P. Allen, J. Melero-Martin, and J. Bischoff, "Type I collagen, fibrin and PuraMatrix matrices provide permissive environments for human endothelial and mesenchymal progenitor cells to form neovascular networks," *J. Tissue Eng. Regen. Med.*, vol. 5, no. 4, pp. e74–e86, 2011.

[3] S. S. Scherer-pietramaggiori, G. Pietramaggiori, and P. Dennis, "Skin graft," *Plast. Surg. Vol. 1 Princ.*, pp. 318–338, 2013.

[4] D. P. Orgill, C. Butler, J. F. Regan, M. S. Barlow, I. V Yannas, and C. C. Compton, "Vascularized collagen-glycosaminoglycan matrix provides a dermal substrate and improves take of cultured epithelial autografts.," *Plast. Reconstr. Surg.*, vol. 102, no. 2, pp. 423–429, 1998.

[5] S. MacNeil, "Progress and opportunities for tissue-engineered skin.," *Nature*, vol. 445, no. 7130, pp. 874–80, 2007.

[6] R. C. Young and A. Burd, "Paediatric upper limb contracture release following burn injury," *Burns*, vol. 30, no. 7, pp. 723–728, 2004.

[7] J. D. Frame *et al.*, "Use of dermal regeneration template in contracture release procedures: a multicenter evaluation," *Plast. Reconstr. Surg.*, vol. 113, no. 5, pp. 1330–1338, 2004.

[8] B. S. Atiyeh and M. Costagliola, "Cultured epithelial autograft (CEA) in burn treatment: Three decades later," *Burns*, vol. 33, no. 4, pp. 405–413, 2007.

[9] J. S. Williamson *et al.*, "Cultured epithelial autograft: Five years of clinical experience with twenty-eight patients," *J. Trauma - Inj. Infect. Crit. Care*, vol. 39, no. 2, pp. 309–319, 1995.

[10] F. Canales *et al.*, "Microvascular tissue transfer in paediatric patients: analysis of 106 cases," *Br. J. Plast. Surg.*, vol. 44, no. 6, pp. 423–427, 1991.

[11] J. M. Serletti, J. V. A. Schingo, M. A. Deuber, A. J. Carras, H. R. Herrera, and V. F. Reale, "Free tissue transfer in pediatric patients.," *Ann. Plast. Surg.*, vol. 36, no. 6, pp. 561–568, 1996.

[12] J. B. Converse, John Marquis; Smahel and A. D. Donald L.; Harper, "Inosculation of vessels of skin graft and host bed: a fortuitous encounter," *Br. J. Plast. Surg.*, vol. 28, no. 1955, pp. 274–282, 1975.

[13] R. K. Chan *et al.*, "Autologous Graft Thickness Affects Scar Contraction and Quality in a Porcine Excisional Wound Model.," *Plast. Reconstr. surgery. Glob. open*, vol. 3, no. 7, p. e468, 2015.

[14] N. L. Rosin *et al.*, "Collagen structural alterations contribute to stiffening of tissue after split-thickness skin grafting," *Wound Repair Regen.*, vol. 24, no. 2, pp. 263–274, 2016.

[15] I. V. Yannas, "Tissue and Organ Regeneration in Adults," *Saudi Med J*, vol. 33, pp. 3–8, 2015.

[16] M. Varkey, J. Ding, and E. Tredget, "Advances in Skin Substitutes—Potential of Tissue Engineered Skin for Facilitating Anti-Fibrotic Healing," *J. Funct. Biomater.*, vol. 6, no. 3, pp. 547–563, 2015.

[17] R. V Shevchenko, S. L. James, and S. E. James, "A review of tissue-engineered skin bioconstructs available for skin reconstruction," *J. R. Soc. Interface*, vol. 7, no. 43, pp. 229–258, 2009.

[18] D. Q. A. Nguyen, T. S. Potokar, and P. Price, "An objective long-term evaluation of Integra (a dermal skin substitute) and split thickness skin grafts, in acute burns and reconstructive surgery," *Burns*, vol. 36, no. 1, pp. 23–28, 2010.

[19] C. Cuono, R. Langdon, and J. McGuire, "Use of Cultured Epidermal Autografts and Dermal Allografts As Skin Replacement After Burn Injury," *Lancet*, vol. 327, no. 8490, pp. 1123–1124, 1986.

[20] R. V Shevchenko, S. L. E. James, and S. L. E. James, "A review of tissue-engineered skin bioconstructs available for skin reconstruction.," *J. R. Soc. Interface*, vol. 7, no. 43, pp. 229–258, 2010.

[21] M. M. Melendez *et al.*, "Porcine wound healing in full-thickness skin defects using Integra??? with and without fibrin glue with keratinocytes," *Can. J. Plast. Surg.*, vol. 16, no. 3, pp. 147–152, 2008.

[22] F. Grinnell, "Fibroblasts, myofibroblasts, and wound contraction.," *J. Cell Biol.*, vol. 124, no. 4, pp. 401–404, 1994.

[23] H. Debels, M. Hamdi, K. Abberton, and W. Morrison, "Dermal matrices and bioengineered skin substitutes: a critical review of current options.," *Plast. Reconstr. surgery. Glob. open*, vol. 3, no. 1, p. e284, 2015.

[24] D. J. Prockop and K. I. Kivirikko, "Collagens: molecular biology, diseases, and potentials for therapy," *Annu. Rev. Biochem.*, vol. 64, no. 1, pp. 403–434, 1995.

[25] S. T. Kreger *et al.*, "Polymerization and matrix physical properties as important design considerations for soluble collagen formulations," *Biopolym. Orig. Res. Biomol.*, vol. 93, no. 8, pp. 690–707, 2010.

[26] L. C. Abraham, E. Zuena, B. Perez-Ramirez, and D. L. Kaplan, "Guide to collagen characterization for biomaterial studies," *J. Biomed. Mater. Res. Part B Appl. Biomater. An Off. J. Soc. Biomater. Japanese Soc. Biomater. Aust. Soc. Biomater. Korean Soc. Biomater.*, vol. 87, no. 1, pp. 264–285, 2008.

[27] A. M. Pizzo, K. Kokini, L. C. Vaughn, and B. Z. Waisner, "Extracellular matrix (ECM) microstructural composition regulates local cell-ECM biomechanics and fundamental fibroblast behavior : a multidimensional p erspective," vol. 2026, pp. 1909–1921, 2005.

[28] K. M. Blum *et al.*, "Acellular and cellular high-density, collagen-fibril constructs with suprafibrillar organization," *Biomater. Sci.*, vol. 4, no. 4, pp. 711–723, 2016.

[29] T. Novak, B. Seelbinder, C. M. Twitchell, C. C. Van Donkelaar, S. L. Voytik-harbin, and C. P. Neu, "Mechanisms and Microenvironment Investigation of Cellularized High Density Gradient Collagen Matrices via Densifi cation," vol. 1, pp. 2617–2628, 2016.

[30] L. A. Hapach, J. A. VanderBurgh, J. P. Miller, and C. A. Reinhart-King, "Manipulation of in vitro collagen matrix architecture for scaffolds of improved physiological relevance," *Phys. Biol.*, vol. 12, no. 6, p. 61002, 2015.

[31] A. Carpentier, "Biological factors affecting long-term results of yalvular hetero-grafts," *J. thorac. Cardiovasc. Surg.*, vol. 58, pp. 467–483, 1969.

[32] L. M. Delgado, Y. Bayon, A. Pandit, and D. I. Zeugolis, "To cross-link or not to cross-link? Cross-linking associated foreign body response of collagen-based devices," *Tissue Eng. Part B Rev.*, vol. 21, no. 3, pp. 298–313, 2015.

[33] Y. Chang, C.-C. Tsai, H.-C. Liang, and H.-W. Sung, "In vivo evaluation of cellular and acellular bovine pericardia fixed with a naturally occurring crosslinking agent (genipin)," *Biomaterials*, vol. 23, no. 12, pp. 2447–2457, 2002.

[34] E. A. Jaffe, R. L. Nachman, C. G. Becker, and C. R. Minick, "Culture of human endothelial cells derived from umbilical veins. Identification by morphologic and immunologic criteria," *J. Clin. Invest.*, vol. 52, no. 11, pp. 2745–2756, 1973.

[35] X. Xin *et al.*, "Hepatocyte growth factor enhances vascular endothelial growth factor-induced angiogenesis in vitro and in vivo," *Am. J. Pathol.*, vol. 158, no. 3, pp. 1111–1120, 2001.

[36] D. A. Ingram *et al.*, "Identification of a novel hierarchy of endothelial progenitor cells using human peripheral and umbilical cord blood," *Blood*, vol. 104, no. 9, pp. 2752–2760, 2004.

[37] A. L. Sieminski, R. P. Hebbel, and K. J. Gooch, "Improved microvascular network in vitro by human blood outgrowth endothelial cells relative to vessel-derived endothelial cells.," *Tissue Eng.*, vol. 11, no. 9–10, pp. 1332–1345, 2005.

[38] C. F. Whittington, M. C. Yoder, S. L. Voytik-Harbin, and S. L. Voytik-Harbin, "Collagen-Polymer Guidance of Vessel Network Formation and Stabilization by Endothelial Colony Forming Cells In Vitro.," *Macromol. Biosci.*, vol. 13, no. 9, pp. 1–15, Jul. 2013.

[39] J. L. Bailey, P. J. Critser, C. Whittington, J. L. Kuske, and M. C. Yoder, "Collagen oligomers modulate physical and biological properties of three-dimensional self-assembled matrices," vol. 95, no. 2, 2010.

[40] P. J. Critser, S. T. Kreger, S. L. Voytik-Harbin, and M. C. Yoder, "Collagen matrix physical properties modulate endothelial colony forming cell-derived vessels in vivo," *Microvasc. Res.*, vol. 80, no. 1, pp. 23–30, 2010.

[41] X. Chen *et al.*, "Prevascularization of a fibrin-based tissue construct accelerates the formation of functional anastomosis with host vasculature.," *Tissue Eng. Part A*, vol. 15, no. 6, pp. 1363–71, Jun. 2009.

[42] I. Montaño *et al.*, "Formation of human capillaries in vitro: the engineering of prevascularized matrices.," *Tissue Eng. Part A*, vol. 16, no. 1, pp. 269–282, 2010.

[43] A. S. Klar *et al.*, "Tissue-engineered dermo-epidermal skin grafts prevascularized with adipose-derived cells," *Biomaterials*, vol. 35, no. 19, pp. 5065–5078, 2014.

[44] E. F. Kung, F. Wang, and J. S. Schechner, "In vivo perfusion of human skin substitutes with microvessels formed by adult circulating endothelial progenitor cells," *Dermatologic Surg.*, vol. 34, no. 2, pp. 137–146, 2008.

[45] J. S. Schechner *et al.*, "Engraftment of a vascularized human skin equivalent.," *FASEB J.*, vol. 17, no. 15, pp. 2250–2256, 2003.

[46] B. R. Shepherd, D. R. Enis, F. Wang, Y. Suarez, J. S. Pober, and J. S. Schechner, "Vascularization and engraftment of a human skin substitute using circulating progenitor cell-derived endothelial cells.," *FASEB J.*, vol. 20, no. 10, pp. 1739–1741, 2006.

[47] D. M. Supp, K. Wilson-Landy, and S. T. Boyce, "Human dermal microvascular endothelial cells form vascular analogs in cultured skin substitutes after grafting to athymic mice.," *FASEB J.*, vol. 16, no. 8, pp. 797–804, 2002.

[48] P. L. Tremblay, V. Hudon, F. Berthod, L. Germain, F. A. Auger, and A. Auger, "Inosculation of Tissue-Engineered Capillaries with the Host's Vasculature in a Reconstructed Skin Transplanted on Mice," *Am. J. Transplant.*, vol. 5, no. 5, pp. 1002–1010, 2005.

[49] D. Marino *et al.*, "Bioengineering dermo-epidermal skin grafts with blood and lymphatic capillaries.," *Sci. Transl. Med.*, vol. 6, no. 221, p. 221ra14, 2014.

[50] A. S. Klar *et al.*, "Characterization of vasculogenic potential of human adipose-derived endothelial cells in a three-dimensional vascularized skin substitute," *Pediatr. Surg. Int.*, vol. 32, no. 1, pp. 17–27, 2016.

[51] J. S. Schechner *et al.*, "In vivo formation of complex microvessels lined by human endothelial cells in an immunodeficient mouse.," *Proc. Natl. Acad. Sci. U. S. A.*, vol. 97, no. 16, pp. 9191–6, 2000.

[52] A. L. Sieminski, R. P. Hebbel, and K. J. Gooch, "The relative magnitudes of endothelial force generation and matrix stiffness modulate capillary morphogenesis in vitro," *Exp. Cell Res.*, vol. 297, no. 2, pp. 574–584, 2004.

[53] G. E. Davis and C. W. Camarillo, "An α2β1 integrin-dependent pinocytic mechanism involving intracellular vacuole formation and coalescence regulates capillary lumen and tube formation in three-dimensional collagen matrix," *Exp. Cell Res.*, vol. 224, no. 1, pp. 39–51, 1996.

[54] S. J. Kim *et al.*, "Matrix rigidity regulates spatiotemporal dynamics of Cdc42 activity and vacuole formation kinetics of endothelial colony forming cells," *Biochem. Biophys. Res. Commun.*, vol. 443, no. 4, pp. 1280–1285, 2014.

[55] V. L. Cross *et al.*, "Dense type I collagen matrices that support cellular remodeling and microfabrication for studies of tumor angiogenesis and vasculogenesis in vitro," *Biomaterials*, vol. 31, no. 33, pp. 8596–8607, 2010.

[56] E. Kniazeva and A. J. Putnam, "Endothelial cell traction and ECM density influence both capillary morphogenesis and maintenance in 3-D," pp. 179–187, 2009.

[57] E. Kniazeva, S. Kachgal, A. J. Putnam, and D. Ph, "Effects of Extracellular Matrix Density and Mesenchymal Stem Cells on Neovascularization In Vivo," vol. 17, 2011.

[58] L. T. Edgar, C. J. Underwood, J. E. Guilkey, J. B. Hoying, and J. A. Weiss, "Extracellular Matrix Density Regulates the Rate of Neovessel Growth and Branching in Sprouting Angiogenesis," vol. 9, no. 1, pp. 1–10, 2014.

[59] A. G. Mikos *et al.*, "Engineering complex tissues," *Tissue Eng.*, vol. 12, no. 12, pp. 3307–3339, 2006.

[60] H. H. Lu and J. Jiang, "Interface Tissue Engineeringand the Formulation of Multiple-Tissue Systems," in *Tissue Engineering I*, Springer, 2005, pp. 91–111.

[61] J. E. Phillips, K. L. Burns, J. M. Le Doux, R. E. Guldberg, and A. J. García, "Engineering graded tissue interfaces," *Proc. Natl. Acad. Sci.*, vol. 105, no. 34, pp. 12170–12175, 2008.

[62] M. Lovett, K. Lee, A. Edwards, and D. L. Kaplan, "Vascularization strategies for tissue engineering," *Tissue Eng. Part B Rev.*, vol. 15, no. 3, pp. 353–370, 2009.

[63] T. Mammoto, A. Mammoto, and D. E. Ingber, "Mechanobiology and developmental control," *Annu. Rev. Cell Dev. Biol.*, vol. 29, pp. 27–61, 2013.

[64] W. Risau and I. Flamme, "Vasculogenesis," *Annu. Rev. Cell Dev. Biol.*, vol. 11, no. 1, pp. 73–91, 1995.

[65] S. Patel-Hett and P. A. D'Amore, "Signal transduction in vasculogenesis and developmental angiogenesis," *Int. J. Dev. Biol.*, vol. 55, no. 4–5, pp. 353–369, 2011.

[66] R. Montesano and L. Orci, "Tumor-promoting phorbol esters induce angiogenesis in vitro," *Cell*, vol. 42, no. 2, pp. 469–477, 1985.

[67] D. G. Chalupowicz, Z. A. Chowdhury, T. L. Bach, C. Barsigian, and J. Martinez, "Fibrin II induces endothelial cell capillary tube formation.," *J. Cell Biol.*, vol. 130, no. 1, pp. 207–215, 1995.

[68] R. Montesano, L. Orci, and P. Vassalli, "In vitro rapid organization of endothelial cells into capillary-like networks is promoted by collagen matrices.," *J. Cell Biol.*, vol. 97, no. 5, pp. 1648–1652, 1983.

[69] R. F. Nicosia and A. Ottinetti, "Growth of microvessels in serum-free matrix culture of rat aorta. A quantitative assay of angiogenesis in vitro.," *Lab. Invest.*, vol. 63, no. 1, pp. 115–122, 1990.

[70] J. B. Hoying and S. K. Williams, "Effects of basic fibroblast growth factor on human microvessel endothelial cell migration on collagen I correlates inversely with adhesion and is cell density dependent," *J. Cell. Physiol.*, vol. 168, no. 2, pp. 294–304, 1996.

[71] V. Nehls and D. Drenckhahn, "A microcarrier-based cocultivation system for the investigation of factors and cells involved in angiogenesis in three-dimensional fibrin matrices in vitro," *Histochem. Cell Biol.*, vol. 104, no. 6, pp. 459–466, 1995.

[72] T. Korff and H. G. Augustin, "Integration of endothelial cells in multicellular spheroids prevents apoptosis and induces differentiation," *J. Cell Biol.*, vol. 143, no. 5, pp. 1341–1352, 1998.

[73] M. S. Pepper, R. Montesano, J. Vassalli, and L. Orci, "Chondrocytes inhibit endothelial sprout formation in vitro: Evidence for involvement of a transforming growth factor-beta," *J. Cell. Physiol.*, vol. 146, no. 1, pp. 170–179, 1991.

[74] K. J. Bayless, R. Salazar, and G. E. Davis, "RGD-dependent vacuolation and lumen formation observed during endothelial cell morphogenesis in three-dimensional fibrin matrices involves the αvβ3 and α5β1 integrins," *Am. J. Pathol.*, vol. 156, no. 5, pp. 1673–1683, 2000.

[75] B. Vailhé, D. Vittet, and J.-J. Feige, "In vitro models of vasculogenesis and angiogenesis," *Lab. Investig.*, vol. 81, no. 4, p. 439, 2001.

[76] J. A. Madri, B. M. Pratt, and A. M. Tucker, "Phenotypic modulation of endothelial cells by transforming growth factor-beta depends upon the composition and organization of the extracellular matrix.," *J. Cell Biol.*, vol. 106, no. 4, pp. 1375–1384, 1988.

[77] W. B. Saunders *et al.*, "Coregulation of vascular tube stabilization by endothelial cell TIMP-2 and pericyte TIMP-3," *J. Cell Biol.*, vol. 175, no. 1, pp. 179–191, 2006.

[78] G. E. Davis, K. J. Bayless, and A. Mavila, "Molecular basis of endothelial cell morphogenesis in three-dimensional extracellular matrices," *Anat. Rec. An Off. Publ. Am. Assoc. Anat.*, vol. 268, no. 3, pp. 252–275, 2002.

[79] L. T. Edgar, J. B. Hoying, and J. A. Weiss, "In silico investigation of angiogenesis with growth and stress generation coupled to local extracellular matrix density," *Ann. Biomed. Eng.*, vol. 43, no. 7, pp. 1531–1542, 2015.

[80] L. Krishnan *et al.*, "Effect of mechanical boundary conditions on orientation of angiogenic microvessels," *Cardiovasc. Res.*, vol. 78, no. 2, pp. 324–332, 2008.

[81] R. K. Jain, P. Au, J. Tam, D. G. Duda, and D. Fukumura, "Engineering vascularized tissue," *Nat. Biotechnol.*, vol. 23, no. 7, p. 821, 2005.

[82] C. Whittington and E. Brandner, "Oligomers Modulate Interfibril Branching and Mass Transport Properties of Collagen Matrices.," *Microsc Mi*, pp. 1–11, 2013.

[83] S. L. Voytik-Harbin and B. Han, "Collagen–Cell Interactions and Modeling in Microenvironments," *CRC Handb. Imaging Biol. Mech. Taylor Fr. Gr.*, pp. 261–273, 2015.

[84] X. Chen, R. S. Patel, J. A. Weibel, and S. V Garimella, "Coalescence-induced jumping of multiple condensate droplets on hierarchical superhydrophobic surfaces," *Sci. Rep.*, vol. 6, p. 18649, 2016.

[85] A. Standard, "F3089: Characterization and standardization of polymerizable collagen-based products and associated collagen− cell interactions." ASTM International: West Conshohocken, PA, 2014.

[86] B. A. Roeder, K. Kokini, J. E. Sturgis, J. P. Robinson, and S. L. Voytik-Harbin, "Tensile mechanical properties of three-dimensional type I collagen extracellular matrices with varied microstructure," *J. Biomech. Eng.*, vol. 124, no. 2, pp. 214–222, 2002.

[87] D. A. Ingram *et al.*, "Identification of a novel hierarchy of endothelial progenitor cells using human peripheral and umbilical cord blood," *Blood*, vol. 104, no. 9, pp. 2752–2760, 2004.

[88] S. L. Voytik-Harbin, B. Rajwa, and J. P. Robinson, "Three-dimensional imaging of extracellular matrix and extracellular matrix-cell interactions," *Methods Cell Biol.*, vol. 63, pp. 583–597, 2001.

[89] A. N. Stratman *et al.*, "Endothelial cell lumen and vascular guidance tunnel formation requires MT1-MMP–dependent proteolysis in 3-dimensional collagen matrices," *Blood*, vol. 114, no. 2, pp. 237–247, 2009.

[90] P. Allen, J. Melero-Martin, J. Bischoff, J. Melero-Martin, and J. Bischoff, "Type I collagen, fibrin and PuraMatrix matrices provide permissive environments for human endothelial and mesenchymal progenitor cells to form neovascular networks," *J. Tissue Eng. Regen. Med.*, vol. 5, no. 4, pp. e74–e86, 2011.

[91] R. R. Rao, A. W. Peterson, J. Ceccarelli, A. J. Putnam, and J. P. Stegemann, "Matrix composition regulates three-dimensional network formation by endothelial cells and mesenchymal stem cells in collagen/fibrin materials," *Angiogenesis*, vol. 15, no. 2, pp. 253–264, 2012.

[92] W. Koh, A. N. Stratman, A. Sacharidou, and G. E. Davis, "In vitro three dimensional collagen matrix models of endothelial lumen formation during vasculogenesis and angiogenesis," *Methods Enzymol.*, vol. 443, no. 08, pp. 83–101, 2008.

[93] J. A. Whisler, M. B. Chen, and R. D. Kamm, "Control of perfusable microvascular network morphology using a multiculture microfluidic system," *Tissue Eng. Part C Methods*, vol. 20, no. 7, pp. 543–552, 2012.

[94] R. B. Vernon and E. H. Sage, "Contraction of fibrillar type I collagen by endothelial cells: a study in vitro," *J. Cell. Biochem.*, vol. 60, no. 2, pp. 185–197, 1996.

[95] H. Mohammadi, P. D. Arora, C. A. Simmons, P. A. Janmey, and C. A. McCulloch, "Inelastic behaviour of collagen networks in cell–matrix interactions and mechanosensation," *J. R. Soc. Interface*, vol. 12, no. 102, p. 20141074, 2015.

[96] Y. K. Park, T.-Y. Tu, S. H. Lim, I. J. M. Clement, S. Y. Yang, and R. D. Kamm, "In vitro microvessel growth and remodeling within a three-dimensional microfluidic environment," *Cell. Mol. Bioeng.*, vol. 7, no. 1, pp. 15–25, 2014.

[97] J. P. Morgan *et al.*, "Formation of microvascular networks in vitro," *Nat. Protoc.*, vol. 8, no. 9, p. 1820, 2013.

[98] J. M. Sorrell, M. A. Baber, and A. I. Caplan, "Construction of a bilayered dermal equivalent containing human papillary and reticular dermal fibroblasts: use of fluorescent vital dyes," *Tissue Eng.*, vol. 2, no. 1, pp. 39–49, 1996.

[99] M. Heiss *et al.*, "Endothelial cell spheroids as a versatile tool to study angiogenesis in vitro," *FASEB J.*, vol. 29, no. 7, pp. 3076–3084, 2015.

[100] T. Korff and H. G. Augustin, "Tensional forces in fibrillar extracellular matrices control directional capillary sprouting," *J Cell Sci*, vol. 112, no. 19, pp. 3249–3258, 1999.

[101] D. E. Ingber, "Mechanical signaling and the cellular response to extracellular matrix in angiogenesis and cardiovascular physiology," *Circ. Res.*, vol. 91, no. 10, pp. 877–887, 2002.

[102] C. J. Drake, "Embryonic and adult vasculogenesis," *Birth Defects Res. Part C Embryo Today Rev.*, vol. 69, no. 1, pp. 73–82, 2003.

[103] C. J. Drake, A. LaRue, N. Ferrara, and C. D. Little, "VEGF regulates cell behavior during vasculogenesis," *Dev. Biol.*, vol. 224, no. 2, pp. 178–188, 2000.

[104] D. O. Traktuev *et al.*, "Robust functional vascular network formation in vivo by cooperation of adipose progenitor and endothelial cells," *Circ. Res.*, vol. 104, no. 12, pp. 1410–1420, 2009.

[105] P. Au, J. Tam, D. Fukumura, and R. K. Jain, "Bone marrow–derived mesenchymal stem cells facilitate engineering of long-lasting functional vasculature," *Blood*, vol. 111, no. 9, pp. 4551–4558, 2008.

[106] S. Rohringer *et al.*, "Mechanisms of vasculogenesis in 3D fibrin matrices mediated by the interaction of adipose-derived stem cells and endothelial cells," *Angiogenesis*, vol. 17, no. 4, pp. 921–933, 2014.

[107] S. Strassburg, H. Nienhueser, G. Björn Stark, G. Finkenzeller, and N. Torio-Padron, "Co-culture of adipose-derived stem cells and endothelial cells in fibrin induces angiogenesis and vasculogenesis in a chorioallantoic membrane model," *J. Tissue Eng. Regen. Med.*, vol. 10, no. 6, pp. 496–506, 2016.

[108] A. N. Stratman, M. J. Davis, and G. E. Davis, "VEGF and FGF prime vascular tube morphogenesis and sprouting directed by hematopoietic stem cell cytokines," *Blood*, p. blood-2010, 2011.

[109] K. Pill, S. Hofmann, H. Redl, and W. Holnthoner, "Vascularization mediated by mesenchymal stem cells from bone marrow and adipose tissue: a comparison.," *Cell Regen. (London, England)*, vol. 4, no. 1, p. 8, 2015.

[110] W. Holnthoner *et al.*, "Adipose-derived stem cells induce vascular tube formation of outgrowth endothelial cells in a fibrin matrix," *J. Tissue Eng. Regen. Med.*, vol. 9, no. 2, pp. 127–136, 2015.

[111] F. Verseijden, S. J. Posthumus-van Sluijs, P. Pavljasevic, S. O. P. Hofer, G. J. V. M. van Osch, and E. Farrell, "Adult human bone marrow–and adipose tissue–derived stromal cells support the formation of prevascular-like structures from endothelial cells in vitro," *Tissue Eng. Part A*, vol. 16, no. 1, pp. 101–114, 2009.

[112] M. Hellstrom, P. Lindahl, A. Abramsson, and C. Betsholtz, "Role of PDGF-B and PDGFR-beta in recruitment of vascular smooth muscle cells and pericytes during embryonic blood vessel formation in the mouse," *Development*, vol. 126, no. 14, pp. 3047–3055, 1999.

[113] A. N. Stratman, A. E. Schwindt, K. M. Malotte, and G. E. Davis, "Endothelial-derived PDGF-BB and HB-EGF coordinately regulate pericyte recruitment during vasculogenic tube assembly and stabilization," *Blood*, p. blood-2010, 2010.

[114] S. Gehmert *et al.*, "Angiogenesis: the role of PDGF-BB on adiopse-tissue derived stem cells (ASCs)," *Clin. Hemorheol. Microcirc.*, vol. 48, no. 1–3, pp. 5–13, 2011.

[115] E. S. Groban, A. Narayanan, and M. P. Jacobson, "Conformational changes in protein loops and helices induced by post-translational phosphorylation," *PLoS Comput. Biol.*, vol. 2, no. 4, p. e32, 2006.

[116] D. Domínguez *et al.*, "Phosphorylation regulates the subcellular location and activity of the snail transcriptional repressor," *Mol. Cell. Biol.*, vol. 23, no. 14, pp. 5078–5089, 2003.

[117] T. Hunter, "Protein kinases and phosphatases: the yin and yang of protein phosphorylation and signaling," *Cell*, vol. 80, no. 2, pp. 225–236, 1995.

[118] C. S. Abhinand, R. Raju, S. J. Soumya, P. S. Arya, and P. R. Sudhakaran, "VEGF-A/VEGFR2 signaling network in endothelial cells relevant to angiogenesis," *J. Cell Commun. Signal.*, vol. 10, no. 4, pp. 347–354, 2016.

[119] R. L. Kendall, R. Z. Rutledge, X. Mao, A. J. Tebben, R. W. Hungate, and K. A. Thomas, "Vascular endothelial growth factor receptor KDR tyrosine kinase activity is increased by autophosphorylation of two activation loop tyrosine residues," *J. Biol. Chem.*, vol. 274, no. 10, pp. 6453–6460, 1999.

[120] R. B. Oelrichs, H. H. Reid, O. Bernard, A. Ziemiecki, and A. F. Wilks, "NYK/FLK-1: a putative receptor protein tyrosine kinase isolated from E10 embryonic neuroepithelium is expressed in endothelial cells of the developing embryo.," *Oncogene*, vol. 8, no. 1, pp. 11–18, 1993.

[121] T. P. Quinn, K. G. Peters, C. De Vries, N. Ferrara, and L. T. Williams, "Fetal liver kinase 1 is a receptor for vascular endothelial growth factor and is selectively expressed in vascular endothelium," *Proc. Natl. Acad. Sci.*, vol. 90, no. 16, pp. 7533–7537, 1993.

[122] B. Millauer *et al.*, "High affinity VEGF binding and developmental expression suggest Flk-1 as a major regulator of vasculogenesis and angiogenesis," *Cell*, vol. 72, no. 6, pp. 835–846, 1993.

[123] "Shalabi et al_Nature 1995_Failure of blood-island formation and vasculogenesis in Flk-1-deficient mice.pdf." .

[124] H. Gerber *et al.*, "Vascular Endothelial Growth Factor Regulates Endothelial Cell Survival through the Phosphatidylinositol 3'-Kinase / Akt Signal," *J. Biol. Chem.*, vol. 273, no. 46, pp. 30336–30343, 1998.

[125] C. W. Lewis, R. G. Taylor, P. M. Kubara, K. Marshall, L. Meijer, and R. M. Golsteyn, "A western blot assay to measure cyclin dependent kinase activity in cells or in vitro without the use of radioisotopes," *FEBS Lett.*, vol. 587, no. 18, pp. 3089–3095, 2013.

[126] N. Dephoure, K. L. Gould, S. P. Gygi, and D. R. Kellogg, "Mapping and analysis of phosphorylation sites: a quick guide for cell biologists," *Mol. Biol. Cell*, vol. 24, no. 5, pp. 535–542, 2013.

[127] C. J. Hastie, H. J. McLauchlan, and P. Cohen, "Assay of protein kinases using radiolabeled ATP: a protocol," *Nat. Protoc.*, vol. 1, no. 2, p. 968, 2006.

[128] P. Argani *et al.*, "Primary renal neoplasms with the ASPL-TFE3 gene fusion of alveolar soft part sarcoma: a distinctive tumor entity previously included among renal cell carcinomas of children and adolescents," *Am. J. Pathol.*, vol. 159, no. 1, pp. 179–192, 2001.

[129] M. D. Shults, K. A. Janes, D. A. Lauffenburger, and B. Imperiali, "A multiplexed homogeneous fluorescence-based assay for protein kinase activity in cell lysates," *Nat. Methods*, vol. 2, no. 4, p. 277, 2005.

[130] R. S. Agnes, F. Jernigan, J. R. Shell, V. Sharma, and D. S. Lawrence, "Suborganelle sensing of mitochondrial cAMP-dependent protein kinase activity," *J. Am. Chem. Soc.*, vol. 132, no. 17, pp. 6075–6080, 2010.

[131] Q. Wang, E. I. Zimmerman, A. Toutchkine, T. D. Martin, L. M. Graves, and D. S. Lawrence, "Multicolor monitoring of dysregulated protein kinases in chronic myelogenous leukemia," *ACS Chem. Biol.*, vol. 5, no. 9, pp. 887–895, 2010.

[132] P.-A. Vidi, J. Chen, J. M. K. Irudayaraj, and V. J. Watts, "Adenosine A2A receptors assemble into higher-order oligomers at the plasma membrane," *FEBS Lett.*, vol. 582, no. 29, pp. 3985–3990, 2008.

[133] J. Chen and J. Irudayaraj, "Fluorescence lifetime cross correlation spectroscopy resolves EGFR and antagonist interaction in live cells," *Anal. Chem.*, vol. 82, no. 15, pp. 6415–6421, 2010.

[134] N. P. Damayanti, L. L. Parker, and J. M. K. Irudayaraj, "Fluorescence lifetime imaging of biosensor peptide phosphorylation in single live cells," *Angew. Chemie*, vol. 125, no. 14, pp. 4023–4026, 2013.

[135] J. Dai *et al.*, "Osteopontin induces angiogenesis through activation of PI3K/AKT and ERK1/2 in endothelial cells," *Oncogene*, vol. 28, no. 38, p. 3412, 2009.

[136] M. Simons, E. Gordon, and L. Claesson-Welsh, "Mechanisms and regulation of endothelial VEGF receptor signalling," *Nat. Rev. Mol. cell Biol.*, vol. 17, no. 10, p. 611, 2016.

[137] R. Moravčík, K. Stebelová, A. Boháč, and M. Zeman, "Inhibition of VEGF mediated post receptor signalling pathways by recently developed tyrosine kinase inhibitor in comparison with sunitinib," *Gen Physiol Biophys*, vol. 35, pp. 511–514, 2016.

[138] J. Zhao, Z.-R. Zhang, N. Zhao, B.-A. Ma, and Q.-Y. Fan, "RETRACTED ARTICLE: VEGF Silencing Inhibits Human Osteosarcoma Angiogenesis and Promotes Cell Apoptosis via PI3K/AKT Signaling Pathway," *Cell Biochem. Biophys.*, vol. 73, no. 2, pp. 519–525, 2015.

[139] N. Peng *et al.*, "Silencing of VEGF inhibits human osteosarcoma angiogenesis and promotes cell apoptosis via VEGF/PI3K/AKT signaling pathway," *Am. J. Transl. Res.*, vol. 8, no. 2, p. 1005, 2016.

[140] M. R. Abid *et al.*, "Vascular endothelial growth factor activates PI3K/Akt/forkhead signaling in endothelial cells," *Arterioscler. Thromb. Vasc. Biol.*, vol. 24, no. 2, pp. 294–300, 2004.

[141] K. P. Buno *et al.*, "In Vitro Multitissue Interface Model Supports Rapid Vasculogenesis and Mechanistic Study of Vascularization across Tissue Compartments," *ACS Appl. Mater. Interfaces*, vol. 8, no. 34, pp. 21848–21860, 2016.

[142] G. Zhao, R. B. Peery, and J. M. Yingling, "Characterization and development of a peptide substrate-based phosphate transfer assay for the human vascular endothelial growth factor receptor-2 tyrosine kinase," *Anal. Biochem.*, vol. 360, no. 2, pp. 196–206, 2007.

[143] A. PaulaáCraig, "A hybrid FLIM-elastic net platform for label free profiling of breast cancer," *Analyst*, vol. 138, no. 23, pp. 7127–7134, 2013.

[144] J. Chen, S. Nag, P.-A. Vidi, and J. Irudayaraj, "Single molecule in vivo analysis of toll-like receptor 9 and CpG DNA interaction," *PLoS One*, vol. 6, no. 4, p. e17991, 2011.

[145] J. Chen, A. Miller, A. L. Kirchmaier, and J. M. K. Irudayaraj, "Single molecule tools elucidate H2A. Z nucleosome composition," *J Cell Sci*, p. jcs-101592, 2012.

[146] J. Chen and J. Irudayaraj, "Quantitative investigation of compartmentalized dynamics of ErbB2 targeting gold nanorods in live cells by single molecule spectroscopy," *ACS Nano*, vol. 3, no. 12, pp. 4071–4079, 2009.

[147] M. Martini, M. C. De Santis, L. Braccini, F. Gulluni, and E. Hirsch, "PI3K/AKT signaling pathway and cancer: an updated review," *Ann. Med.*, vol. 46, no. 6, pp. 372–383, 2014.

[148] W. H. Tan, A. S. Popel, and F. Mac Gabhann, "Computational model of Gab1/2-dependent VEGFR2 pathway to Akt activation," *PLoS One*, vol. 8, no. 6, p. e67438, 2013.

[149] R. W. A. Mackenzie and B. T. Elliott, "Akt/PKB activation and insulin signaling: a novel insulin signaling pathway in the treatment of type 2 diabetes," *Diabetes, Metab. Syndr. Obes. targets Ther.*, vol. 7, p. 55, 2014.

[150] G. Song, G. Ouyang, and S. Bao, "The activation of Akt/PKB signaling pathway and cell survival," *J. Cell. Mol. Med.*, vol. 9, no. 1, pp. 59–71, 2005.

[151] S. Koch, S. Tugues, X. Li, L. Gualandi, and L. Claesson-Welsh, "Signal transduction by vascular endothelial growth factor receptors," *Biochem. J.*, vol. 437, no. 2, pp. 169–183, 2011.

[152] I. Shiojima, "Role of Akt Signaling in Vascular Homeostasis and Angiogenesis," *Circ. Res.*, vol. 90, no. 12, pp. 1243–1250, Jun. 2002.

[153] L. Napione *et al.*, "Unraveling the influence of endothelial cell density on VEGF-A signaling," *Guard.*, vol. 119, no. 23, p. GUARDIAN MASTERCLASSES, 2015.

[154] C. Wu and S. Dedhar, "Integrin-linked kinase (ILK) and its interactors: A new paradigm for the coupling of extracellular matrix to actin cytoskeleton and signaling complexes," *J. Cell Biol.*, vol. 155, no. 3, pp. 505–510, 2001.

[155] A. Papapetropoulos *et al.*, "Angiopoietin-1 inhibits endothelial cell apoptosis via the Akt/survivin pathway," *J. Biol. Chem.*, vol. 275, no. 13, pp. 9102–9105, 2000.

[156] N. W. Gale and G. D. Yancopoulos, "Growth factors acting via endothelial cell-specific receptor tyrosine kinases: VEGFs, angiopoietins, and ephrins in vascular development," *Genes Dev.*, vol. 13, no. 9, pp. 1055–1066, 1999.

[157] C. Suri *et al.*, "Increased vascularization in mice overexpressing angiopoietin-1," *Science (80-.).*, vol. 282, no. 5388, pp. 468–471, 1998.

[158] J. Holash *et al.*, "Vessel cooption, regression, and growth in tumors mediated by angiopoietins and VEGF," *Science (80-.).*, vol. 284, no. 5422, pp. 1994–1998, 1999.

[159] A. Mammoto *et al.*, "A mechanosensitive transcriptional mechanism that controls angiogenesis," *Nature*, vol. 457, no. 7233, p. 1103, 2009.

[160] I. Kim, J.-H. Kim, S.-O. Moon, H. J. Kwak, N.-G. Kim, and G. Y. Koh, "Angiopoietin-2 at high concentration can enhance endothelial cell survival through the phosphatidylinositol 3′-kinase/Akt signal transduction pathway," *Oncogene*, vol. 19, no. 39, p. 4549, 2000.

[161] H.-P. Gerber *et al.*, "Vascular endothelial growth factor regulates endothelial cell survival through the phosphatidylinositol 3′-kinase/Akt signal transduction pathway requirement for Flk-1/KDR activation," *J. Biol. Chem.*, vol. 273, no. 46, pp. 30336–30343, 1998.

[162] A. F. Black, F. Berthod, N. L'heureux, L. Germain, and F. a Auger, "In vitro reconstruction of a human capillary-like network in a tissue-engineered skin equivalent.," *FASEB J.*, vol. 12, no. 1, pp. 1331–1340, 1998.

[163] M. Li, M. J. Mondrinos, M. R. Gandhi, F. K. Ko, A. S. Weiss, and P. I. Lelkes, "Electrospun protein fibers as matrices for tissue engineering," *Biomaterials*, vol. 26, no. 30, pp. 5999–6008, 2005.

[164] V. S. Joshi, N. Y. Lei, C. M. Walthers, B. Wu, and J. C. Y. Dunn, "Macroporosity enhances vascularization of electrospun scaffolds," *J. Surg. Res.*, vol. 183, no. 1, pp. 18–26, 2013.

[165] Q. Zhang *et al.*, "Decellularized skin/adipose tissue flap matrix for engineering vascularized composite soft tissue flaps," *Acta Biomater.*, vol. 35, pp. 166–184, 2016.

[166] A. Diaz-Santana, M. Shan, and A. D. Stroock, "Endothelial cell dynamics during anastomosis in vitro," *Integr. Biol. (United Kingdom)*, vol. 7, no. 4, pp. 454–466, 2015.

[167] A. S. Klar, T. Biedermann, C. Simmen-Meuli, E. Reichmann, and M. Meuli, "Comparison of in vivo immune responses following transplantation of vascularized and non-vascularized human dermo-epidermal skin substitutes," *Pediatr. Surg. Int.*, 2016.

[168] M. G. McCoy, B. R. Seo, S. Choi, and C. Fischbach, "Collagen I hydrogel microstructure and composition conjointly regulate vascular network formation," *Acta Biomater.*, vol. 44, pp. 200–208, 2016.

[169] N. C. Hunt and L. M. Grover, "Cell encapsulation using biopolymer gels for regenerative medicine," *Biotechnol. Lett.*, vol. 32, no. 6, pp. 733–742, 2010.

[170] E. J. Miller and R. K. Rhodes, "[2] Preparation and characterization of the different types of collagen," in *Methods in enzymology*, vol. 82, Elsevier, 1982, pp. 33–64.

[171] J. L. Bailey, P. J. Critser, C. Whittington, J. L. Kuske, M. C. Yoder, and S. L. Voytik-Harbin, "Collagen oligomers modulate physical and biological properties of three-dimensional self-assembled matrices," *Biopolymers*, vol. 95, no. 2, pp. 77–93, 2011.

[172] B. Jiang and E. M. Brey, "Formation of stable vascular networks in engineered tissues," in *Regenerative Medicine and Tissue Engineering-Cells and Biomaterials*, InTech, 2011.

[173] G. E. Davis and D. R. Senger, "Endothelial extracellular matrix: Biosynthesis, remodeling, and functions during vascular morphogenesis and neovessel stabilization," *Circ. Res.*, vol. 97, no. 11, pp. 1093–1107, 2005.

[174] A. Shamloo and S. C. Heilshorn, "Matrix density mediates polarization and lumen formation of endothelial sprouts in VEGF gradients †," vol. 10, no. 22, 2010.

[175] E. M. Darling, R. E. Wilusz, M. P. Bolognesi, S. Zauscher, and F. Guilak, "Spatial mapping of the biomechanical properties of the pericellular matrix of articular cartilage measured in situ via atomic force microscopy," *Biophys. J.*, vol. 98, no. 12, pp. 2848–2856, 2010.

[176] R. L. Sheridan, "Sepsis in pediatric burn patients," *Pediatr. Crit. care Med.*, vol. 6, no. 3, pp. S112–S119, 2005.

[177] R. C. Young and A. Burd, "Paediatric upper limb contracture release following burn injury," *Burns*, vol. 30, no. 7, pp. 723–728, 2004.

[178] J. D. Frame *et al.*, "Use of dermal regeneration template in contracture release procedures: a multicenter evaluation," *Plast Reconstr Surg*, vol. 113, no. 5, pp. 1330–1338, 2004.

[179] I. V. Yannas, D. S. Tzeranis, B. A. Harley, and P. T. C. So, "Biologically active collagen-based scaffolds: Advances in processing and characterization," *Philos. Trans. R. Soc. A Math. Phys. Eng. Sci.*, vol. 368, no. 1917, pp. 2123–2139, 2010.

[180] L. Yildirimer, N. T. K. Thanh, and A. M. Seifalian, "Skin regeneration scaffolds: a multimodal bottom-up approach," *Trends Biotechnol.*, vol. 30, no. 12, pp. 638–648, 2012.

[181] D. M. Wise, "Histologic proof that acellular dermal matrices (ADM)—Enduragen, DermaMatrix, and DuraMatrix—are not repopulated or nonviable and that AlloDerm may be repopulated but degraded synchronously," *Aesthetic Surg. J.*, vol. 32, no. 3, pp. 355–358, 2012.

[182] S. Böttcher-Haberzeth, T. Biedermann, and E. Reichmann, "Tissue engineering of skin," *Burns*, vol. 36, no. 4, pp. 450–460, 2010.

[183] E. E. Tredget, B. Nedelec, P. G. Scott, and A. Ghahary, "Hypertrophic scars, keloids, and contractures: the cellular and molecular basis for therapy," *Surg. Clin. North Am.*, vol. 77, no. 3, pp. 701–730, 1997.

[184] H. C. Grillo and J. Gross, "Thermal reconstitution of collagen from solution and the response to its heterologous implantation," *J. Surg. Res.*, vol. 2, no. 1, pp. 69–82, 1962.

[185] D. G. Kline and G. J. Hayes, "The use of a resorbable wrapper for peripheral-nerve repair: experimental studies in chimpanzees," *J. Neurosurg.*, vol. 21, no. 9, pp. 737–750, 1964.

[186] D. Michaeli and M. McPherson, "Immunologic study of artificial skin used in the treatment of thermal injuries," *J. Burn Care Rehabil.*, vol. 11, no. 1, pp. 21–26, 1990.

[187] C. E. Schmidt and J. M. Baier, "Acellular vascular tissues: natural biomaterials for tissue repair and tissue engineering," *Biomaterials*, vol. 21, no. 22, pp. 2215–2231, 2000.

[188] F. J. Schoen and R. J. Levy, "Calcification of tissue heart valve substitutes: progress toward understanding and prevention," *Ann. Thorac. Surg.*, vol. 79, no. 3, pp. 1072–1080, 2005.

[189] K. Weadock, R. M. Olson, and F. H. Silver, "Evaluation of collagen crosslinking techniques," *Biomater. Med. Devices. Artif. Organs*, vol. 11, no. 4, pp. 293–318, 1983.

[190] H. Lagus, M. Sarlomo-Rikala, T. Böhling, and J. Vuola, "Prospective study on burns treated with Integra®, a cellulose sponge and split thickness skin graft: comparative clinical and histological study—randomized controlled trial," *Burns*, vol. 39, no. 8, pp. 1577–1587, 2013.

[191] S. Ehrmantraut *et al.*, "Perioperative steroid administration inhibits angiogenic host tissue response to porous polyethylene (Medpor) implants," *Eur Cell Mater*, vol. 19, no. 107, p. 16, 2010.

[192] T. Hussain, M. Schneider, B. Summer, and S. Strieth, "Pre-operative in vitro fibroblast coating of porous polyethylene compound grafts–Cell survival in vivo and effects on biocompatibility," *Biomed. Mater. Eng.*, vol. 27, no. 2–3, pp. 237–249, 2016.

[193] H. H. Takeuchi *et al.*, "Influence of skin thickness on the in vitro permeabilities of drugs through Sprague-Dawley rat or Yucatan micropig skin.," *Biol. Pharm. Bull.*, vol. 35, no. 2, pp. 192–202, 2011.

[194] M. D. Stevenson *et al.*, "A self-assembling peptide matrix used to control stiffness and binding site density supports the formation of microvascular networks in three dimensions.," *Acta Biomater.*, vol. 9, no. 8, pp. 7651–7661, Aug. 2013.

[195] M. Detmar *et al.*, "Increased microvascular density and enhanced leukocyte rolling and adhesion in the skin of VEGF transgenic mice.," *J. Invest. Dermatol.*, vol. 111, no. 1, pp. 1–6, Jul. 1998.

[196] H. Kämpfer, J. Pfeilschifter, and S. Frank, "Expressional regulation of angiopoietin-1 and-2 and the tie-1 and-2 receptor tyrosine kinases during cutaneous wound healing: a comparative study of normal and impaired repair," *Lab. Investig.*, vol. 81, no. 3, p. 361, 2001.

[197] F. S. Frueh *et al.*, "Adipose tissue-derived microvascular fragments improve vascularization, lymphangiogenesis, and integration of dermal skin substitutes," *J. Invest. Dermatol.*, vol. 137, no. 1, pp. 217–227, 2017.

[198] T. Später, F. S. Frueh, W. Metzger, M. D. Menger, and M. W. Laschke, "In vivo biocompatibility, vascularization, and incorporation of Integra® dermal regenerative template and flowable wound matrix," *J. Biomed. Mater. Res. - Part B Appl. Biomater.*, vol. 106, no. 1, pp. 52–60, 2018.

[199] C. Beaudoin Cloutier *et al.*, "*In Vivo* Evaluation and Imaging of a Bilayered Self-Assembled Skin Substitute Using a Decellularized Dermal Matrix Grafted on Mice," *Tissue Eng. Part A*, vol. 23, no. 7–8, pp. 313–322, 2017.

[200] A. Bayat, D. A. McGrouther, and M. W. J. Ferguson, "Skin scarring," *BMJ Br. Med. J.*, vol. 326, no. 7380, p. 88, 2003.

[201] R. Ogawa, "Keloid and hypertrophic scars are the result of chronic inflammation in the reticular dermis," *Int. J. Mol. Sci.*, vol. 18, no. 3, p. 606, 2017.

[202] M. Inaba and Y. Inaba, "Blood Vessel System in Hair Follicles," in *Androgenetic Alopecia*, Springer, 1996, pp. 39–44.

[203] M. G. Tonnesen, X. Feng, and R. A. F. Clark, "Angiogenesis in Wound Healing," *J. Investig. Dermatology Symp. Proc.*, vol. 5, no. 1, pp. 40–46, Dec. 2000.

[204] L. F. Brown *et al.*, "Expression of vascular permeability factor (vascular endothelial growth factor) by epidermal keratinocytes during wound healing.," *J. Exp. Med.*, vol. 176, no. 5, pp. 1375–1379, Nov. 1992.

[205] L. Bargues, S. Boyer, T. Leclerc, P. Duhamel, and E. Bey, "Incidence and microbiology of infectious complications with the use of artificial skin Integra in burns," in *Annales de chirurgie plastique et esthetique*, 2009, vol. 54, no. 6, pp. 533–539.

[206] P. Lohana, S. Hassan, and S. B. Watson, "Integra™ in burns reconstruction: our experience and report of an unusual immunological reaction," *Ann. Burns Fire Disasters*, vol. 27, no. 1, p. 17, 2014.

[207] E. Kniazeva and A. J. Putnam, "Endothelial cell traction and ECM density influence both capillary morphogenesis and maintenance in 3-D," *Am. J. Physiol. Physiol.*, vol. 297, no. 1, pp. C179–C187, 2009.

[208] M. Allioux-Guérin *et al.*, "Spatiotemporal analysis of cell response to a rigidity gradient: a quantitative study using multiple optical tweezers," *Biophys. J.*, vol. 96, no. 1, pp. 238–247, 2009.

[209] J. J. Grzesiak, M. D. Pierschbacher, T. I. Malaney, J. R. Glass, and M. F. Amodeo, "Enhancement of cell interactions with collagen / glycosaminoglycan matrices by RGD derivatization," vol. 18, no. 24, pp. 1625–1632, 1998.

[210] F. O. Martinez and S. Gordon, "The M1 and M2 paradigm of macrophage activation: time for reassessment," *F1000Prime Rep.*, vol. 6, 2014.

[211] M. H. M. Barros, F. Hauck, J. H. Dreyer, B. Kempkes, and G. Niedobitek, "Macrophage polarisation: an immunohistochemical approach for identifying M1 and M2 macrophages," *PLoS One*, vol. 8, no. 11, p. e80908, 2013.

[212] G. Gabbiani, "The myofibroblast in wound healing and fibrocontractive diseases," *J. Pathol. A J. Pathol. Soc. Gt. Britain Irel.*, vol. 200, no. 4, pp. 500–503, 2003.

[213] A. Desmoulière, C. Chaponnier, and G. Gabbiani, "Tissue repair, contraction, and the myofibroblast," *Wound repair Regen.*, vol. 13, no. 1, pp. 7–12, 2005.

[214] K. Maruyama, J. Asai, M. Ii, T. Thorne, D. W. Losordo, and P. A. D'Amore, "Decreased macrophage number and activation lead to reduced lymphatic vessel formation and contribute to impaired diabetic wound healing," *Am. J. Pathol.*, vol. 170, no. 4, pp. 1178–1191, 2007.

[215] K. L. Spiller *et al.*, "The role of macrophage phenotype in vascularization of tissue engineering scaffolds," *Biomaterials*, vol. 35, no. 15, pp. 4477–4488, 2014.

[216] E. A. Francischetti, E. Tibirica, E. G. da Silva, E. Rodrigues, B. M. Celoria, and V. G. de Abreu, "Skin capillary density and microvascular reactivity in obese subjects with and without metabolic syndrome," *Microvasc. Res.*, vol. 81, no. 3, pp. 325–330, 2011.

[217] A. Bonamy, H. Martin, G. Jörneskog, and M. Norman, "Lower skin capillary density, normal endothelial function and higher blood pressure in children born preterm," *J. Intern. Med.*, vol. 262, no. 6, pp. 635–642, 2007.